Summer 6-4-2014

Electrostatic Tractor Analysis for GEO Debris Remediation

Erik Alan Hogan
University of Colorado Boulder, erik.hogan@colorado.edu

Electrostatic Tractor Analysis for GEO Debris Remediation

by

Erik A. Hogan

B.S., University of Central Florida, 2009

A thesis submitted to the

Faculty of the Graduate School of the

University of Colorado in partial fulfillment

of the requirements for the degree of

Doctor of Philosophy

Department of Aerospace Engineering

2014

This thesis entitled:
Electrostatic Tractor Analysis for GEO Debris Remediation
written by Erik A. Hogan
has been approved for the Department of Aerospace Engineering

Prof. Hanspeter Schaub

Prof. Zoltan Sternovsky

Prof. Jeffrey Parker

Prof. David Meyer

Prof. Daniel Moorer

Date

The final copy of this thesis has been examined by the signatories, and we find that both the content and the form meet acceptable presentation standards of scholarly work in the above mentioned discipline.

Hogan, Erik A. (Ph.D., Aerospace Engineering)

Electrostatic Tractor Analysis for GEO Debris Remediation

Thesis directed by Prof. Hanspeter Schaub

The high value of operating in the geostationary ring, coupled with increasing numbers of orbital debris, highlights the need for GEO debris remediation techniques. One recent proposed technique for GEO debris mitigation is the electrostatic tractor. Here, a tug vehicle approaches a target debris object and emits a focused electron beam onto it. This results in a negative charge on the debris, and a positive charge on the tug vehicle. Due to the near proximity of the highly charged objects (20 meters or less) an attractive electrostatic force on the order of milliNewtons results. This electrostatic force is used in conjunction with low thrusting by the tug vehicle to tow the debris object into a disposal orbit 200-300 kilometers above the GEO belt.

During the tugging period, the charged relative motion between tug and deputy is stabilized through a feedback control law. This is accomplished using a novel relative motion description that isolates separation distance from the relative orientation. The equations of motion for the relative motion description are derived from the Clohessy-Wiltshire equations, assuming the debris object is in a nearly circular orbit. Lyapunov stability theory is used to derive an asymptotically stable control law for the tug thrusters during the towing period. The control law requires an estimate of the electrostatic force magnitude, and the impacts of improperly modeled charging on control response are determined. If the electrostatic force is under-predicted too severely, a collision may result. A bound on the control gains is determined to prevent such a collision.

Expected reorbiting performance levels achievable with the electrostatic tractor are computed. An open-loop analytical performance study is performed where variational equations are used to predict how much general orbital elements may be changed using the electrostatic tractor over one orbital period for a towed object at geosynchronous altitude. In contrast to earlier work, eccentric orbits and plane changes are also considered. Requirements on relative positioning of

the tug and debris for various orbit corrections are identified for the different orbit corrections. In some cases, the tug must maneuver around the debris at particular locations in the orbit, but the incurred performance losses during this repositioning are minimal. Co-planar reorbiting maneuvers with corrections of several kilometers per day are achievable, but large scale plane changes are not.

A first-order analytic current model is used to calculate the charging on tug debris during the charge transfer process. The model includes plasma currents, photoelectron current, secondary electron emission, and electron beam current. The effects of nominal changes (as a function of local time) in GEO space weather conditions on tractor performance are characterized. While the electron beam current can be modified to compensate for these changes, maintaining a fixed beam current achieves similar performance. The impacts of the relative sizes of tug and deputy are studied to determine thresholds where charge transfer is no longer possible, and the effects on tractor performance are considered. The simultaneous emission of an electron beam (onto the debris) and an ion beam (into space) is considered as a means for improving tractor performance. For smaller tug vehicles, this simultaneous emission allows for significant performance increases, enabling the tug to tow larger debris objects. The benefits are not as pronounced for larger tug vehicles. The debris object emits photoelectrons and secondary electrons that may be recaptured by the positively charged tug. NASCAP-2K is used to provide an estimate about the severity of this back flux. It is not found to hinder performance of the electrostatic tractor. Overall, the study supports the feasibility of the electrostatic tractor for GEO debris remediation, and helps to identify areas for further research.

Dedication

To my wife Diana, this work is dedicated to you for all you have done for me since we first met as lab partners many years ago. I certainly would not be where I am now if wasn't for all of your love and support over the years, and I look forward to our future together.

Also to my parents, thank you for shaping me into the man I am today. You started me on this path as child, and I owe you more than I could ever repay.

Acknowledgements

First and foremost I would like to thank my advisor and mentor, Dr. Hanspeter Schaub. It has truly been a pleasure working with you these past five years. I enjoyed our many long discussions on these various topics, and always appreciated the excitement that you were able to reintroduce when progress sometimes stalled. Thank you for providing me with the opportunity to teach (twice!), and for your ongoing guidance and support in this, and other, endeavors. I consider myself very lucky to have been apart of the AVS Lab, and I also appreciate all of the chances you provided for me to travel and present my work. Thank you to Dr. Zoltan Sternovsky for helping me to make sense of some of the charging dynamics, and for quickly responding to the questions I had. You helped me to identify some potential areas of research that directly contributed to the work detailed here. Thanks also goes to the other members of my committee: Dr. Jeffrey Parker, Dr. Daniel Moorer, and Dr. David Meyer. I very much appreciate your time and the input you have given me during this research.

To the other students in the AVS Lab, thank you for the many thought provoking discussions and suggestions over the years. I appreciate all the time you put in learning about my research, and all the good questions you asked. Thanks for the friendship, and for providing opportunities to take a break from research every now and then.

To my wife, Diana, this work would not have been possible without your love and support. Thank you for following me out to Colorado, teaching me to dance, and for putting up with the snow and cold these past five years! To my parents, thank you for all of the love and guidance that you have provided me. Ever since I can remember, you always encouraged my love for science and

pushed me to explore new things. I would not be where I am today if not for you. Thank you to my grandparents, who also encouraged me to succeed as a child and an adult. To my siblings, thanks for the many good times growing up. I am grateful for all the fond memories I have to look back on now. To the friends that have come and gone, thanks for all the fun and the opportunities to clear my head every now and then.

This research was funded in large part by the GAANN fellowship.

Contents

Chapter

Tables

Table

Figures

Figure

Chapter 1

Introduction

1.1 Motivation

The high value of operating in a geosynchronous orbit (GEO) dictates the need for close monitoring and mitigation of debris which pose a threat to future missions in this orbit regime. Indeed, a large-scale collision event or breakup of a body in GEO could render the region essentially unusable for hundreds, if not thousands of years, owing to its high altitude and negligible drag. Thus, it is of critical importance to prevent, as much as possible, any such event. The recent collision of the Cosmos 2251 and Iridium 33 (albeit in LEO) in 2009 provides an example of how serious such an event might be. As of May 13, 2011, the space surveillance network has catalogued over 2000 debris pieces associated with the collision.[19] A debris cloud of this magnitude introduced into the very narrow GEO environment could set off a chain-reaction of further collision or near-conjunction events, polluting the GEO belt for thousands of years. The latter issue, near-conjunction events, require the operating GEO satellites to use the scarce fuel to perform collision avoidance maneuvers, negating the usefulness of the GEO zone. Another collision event occurred in 1996 when a fragment from an Ariane 5 upper stage collided with the gravity boom on the French Cerise satellite.[4] While the event did not result in a large debris cloud like the Iridium-Cosmos collision, it did result in a loss of attitude stabilization for the Cerise satellite. The severed gravity boom was tracked as a new piece of debris.[55]

International guidelines for end-of-life operations call for removal of the satellite from geosynchronous orbit, often by raising it to a higher altitude. Due to the large amount of fuel required

for re-entry from GEO, it is not feasible to completely remove the satellites from orbit. An orbital increase of at least 300 km is often suggested, though higher altitudes are also proposed.[1,2] In addition to reorbiting, the Inter-Agency Space Debris Coordination Committee (IADC) recommends passivating spacecraft by depleting stored liquids and terminating power to moving parts such as momentum devices to prevent breakups.[2] In spite of these suggested guidelines operators often do not, or are technically unable to, comply. For example, in the period 1997-2003, 103 spacecraft reached end-of-operations. Only 34 were reorbited as suggested by the IADC; the remainder were either reorbited to a lower altitude than recommended or abandoned without any correction maneuver.[51] Non-compliance with end-of-mission suggested protocol increases collision risk. By the year 2000, 125 satellites had already been abandoned. What's more, over 350 objects were tracked drifting around GEO, with most crossing through the GEO belt twice a day.[52] In the years since, additional launches, further satellites reaching their end-of-operations, and newly detected objects have increased these numbers. As of January 1, 2013, over 1100 resident space objects (RSOs) in the GEO belt larger than 1 meter have been catalogued and tracked by U.S. Strategic Command.[5] Of these, only 358 are controlled. The remaining objects drift through the GEO region, uncontrolled, posing a collision risk to operational spacecraft. Depending on the longitude considered, 7-10 near miss events (<50 km) may occur each day; even with 80% end-of-life mitigation practices, the number of near-misses is forecast to double within 50 years.[6] These numbers only consider objects larger than 1 meter. There are many more objects of a smaller size that are untracked.

An operator may fail to abide by the suggested guidelines for a number of reasons, ranging from conscious decision to abandon after all fuel is spent to maximize operational use, to having a mechanical failure which prevents the final reorbiting phase. Thus, it is prudent to investigate strategies for active debris removal (ADR). Numerous ADR strategies have been proposed for varying orbital regimes. For spacecraft in the LEO environment, studies on the feasibility of using electrodynamic tethers indicate deorbiting may be possible within a time period of a few weeks or months.[35,48,49] At geosynchronous altitudes, however, deorbiting is not economically feasible due to the large ΔV requirements for reentry to occur, and the extremely small tether forces experienced

by the electrodynamic tether in geosynchronous regions. Furthermore, the electrodynamic tether concept is best suited for cases when it is built into a satellite before launch. This is due to the difficulty of physically attaching such a system to a potentially uncooperative debris object in orbit. Another proposed method for debris removal is the use of a ground-based high powered laser to impart a ΔV impulse onto an orbiting debris object through surface ablation, causing it to reenter.[75] Again, this method is only practical for objects in the LEO environment, but is likely to encounter numerous political challenges of aiming high-energy systems at LEO. It does, however, avoid the challenges associated with rendezvous and docking of a tumbling debris object. To apply the laser ablation strategy to objects in GEO, a laser equipped satellite must be flown.[107] Flying at a distance of around 15 meters from a debris object with a 5 kW laser, a GEO debris disposal maneuver is estimated to require around 5 days. The space-based laser is also considered for remote detumbling of a debris object, which would enable easier docking. Of course, a space-based destructive laser will fare no better than a ground-based one in the current political climate. Yet another proposal includes docking with targeted debris objects, grappling them with a robotic arm, and attaching a thruster to perform reorbiting maneuvers.[14,18] To implement such a method, the challenges of rendezvous and docking would, again, need to be considered. The recently proposed Ion-Beam-Shepherd method uses the ion-engine exhaust to push a debris object to a new orbit.[12,62] This concept would allow for non-contact reorbiting, but must address the issues of debris spin up within the ion exhaust, and the resulting lateral force deflection issues.

While current day GEO end-of-life disposal rates approach 80%, that still leaves a significant number of objects that reach end-of-life only to remain in the high-value GEO ring, in addition to the debris population that is already there.[54] Swiss Reinsurance Company Ltd, an insurance provider for satellite operations, notes the potential for space debris to destroy operational satellites with losses totaling into billions of dollars.[69] There are about eight times as many satellites insured in GEO as in LEO, with the total value of insured GEO assets exceeding 18 billion USD, compared with 1 billion USD in LEO. This highlights the value of satellite operations in the geosynchronous region, and illustrates the need to protect it from potentially catastrophic collision events. Cur-

rently, there is no generally accepted ideal method for active debris removal in GEO (or LEO), and it is prudent to investigate mitigation strategies to plan for the future.

1.2 Electrostatic Tractor Concept

1.2.1 Overview and Prospects

Recently, interest in the use of electrostatic forces for contactless tugging and remote attitude control of noncooperative objects has grown.[44,98,101,110] Originally proposed as a means for asteroid deflection,[80] the electrostatic tractor has also been suggested as a means for GEO debris remediation.[98] The concept relies on a combination of an attractive electrostatic force between two craft and low thrusting capability on one of the craft. The attractive force acts as a virtual tether between the two objects, and a low thrust maneuver is used to tow the noncooperative object into a new orbit.[44] Considering non-symmetrical spacecraft geometries, the charging also gives rise to torques on the craft.[61,109] Through careful manipulation of the charging histories, these torques can be applied in a manner sufficient to despin a noncooperative object remotely.[101] This latter ability greatly simplifies any orbital servicing mission where great efforts are required to first despin objects spinning at 1 degree per second or greater.[27,28] GEO debris can be tumbling up to 10's of degrees per second,[56] making any physical docking methods particularly challenging. In concept, the electrostatic tug is similar to the gravitational tractor, which is also proposed as a means for deflecting near earth asteroids.[70] Here, a massive spacecraft is used to generate a gravitational force on a celestial body which may be used to slowly modify its orbit over time.

Generally, a noncooperative object such as space debris or a defunct satellite requiring servicing will not possess the capability for self charge control. This dictates the need for a touchless method of remote charge transfer. To this end, a focused electron beam has been suggested as a means for achieving remote charge control for the electrostatic tugging application.[100] The tugging vehicle, equipped with an electron beam, approaches the target deputy object. By focusing the electron beam onto the deputy, a negative potential results from the bombardment of electrons. At

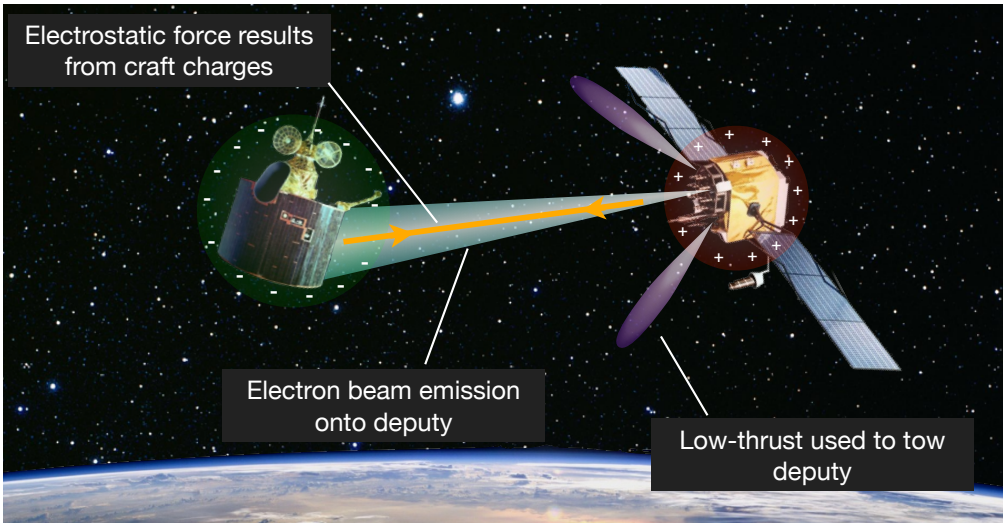

Figure 1.1: Illustration of the electrostatic tugging concept.

the same time, the tug is charged positively by the emission of the electron beam, as illustrated in Figure 1.1. This process generates the required attractive electrostatic force necessary for towing applications, or torques for despinning operations. It is worth noting that electron beams have been used as a method for self-charge control of spacecraft for decades.[64,85] However, they have not been used to do active charging of a neighboring space object.

The electrostatic tractor assumes tug and deputy potentials on the order of 10s of kV, and typical separation distances between the tug and debris object are below 20 meters.[44,98] Natural charging to these levels (10-20 kV, negative) in GEO was observed on the ATS-5 and ATS-6 satellites when the spacecraft were in eclipse, and satellites are designed to handle these charging events.[31,38,89] Current levels on the order of hundreds of microamps to a few milliamps are required to achieve charge transfer, depending on the plasma environment and sizes of the tug and deputy. On the SCATHA mission, a 13 mA electron beam was used to charge the spacecraft to 4 kV positive, so these levels of currents are flight validated. The electron beam energy levels needed for the electrostatic tractor are on the order of 10s of keV. Currently, electron gun systems up to energy levels of 100 keV are commercially available, and Kimball Physics is one such vendor. These systems are designed for the laboratory environment, however, and are not space rated at this time.

With the potential levels and separation distances considered, the resulting electrostatic forces are on the order of 1 mN. In order to actually tow the deputy object, a thruster system capable of generating forces of this magnitude is required. Because of the interest in flying small, lightweight satellite systems, high-efficiency, low-thrust propulsion methods have been investigated for decades. One such example is field emission electric propulsion (FEEP) thrusters, which can provide thrust levels ranging from μN to mN.[74] FEEP thrusters work by accelerating ions through a potential difference, giving rise to a small thrusting force on the spacecraft. Using charged particles for thrust in the electrostatic tractor application could complicate the charging dynamics. An alternate low-thrust system that does not require ion emission is cold gas microthrusters.[63] Here, minute amounts of neutral gas are emitted at supersonic speeds from small nozzles, with maximum thrust levels in the range of 0.1-10 mN.

The electrostatic tractor is an appealing method for near-future GEO debris remediation because much of the technical requirements are achievable with existing technology, some of which already has spaceflight legacy. The electrostatic tractor possesses several intriguing advantages when compared with other methods for reorbiting of non-cooperative objects:

(1) No contact is required with the deputy object, eliminating the need for docking with a possibly tumbling object.

(2) Towing is possible while the deputy object is rotating.

(3) Considering that torques result from three-dimensional charge distributions, objects can be detumbled while towed.[101]

(4) The charge transfer process is non-destructive, with minimal risk of introducing additional pieces of debris.

(5) Both cooperative and non-cooperative objects may be towed.

(6) Multiple debris objects can be reorbited (one at a time) with a single tug vehicle.

It is not difficult to envision a scenario where a formation of spacecraft needs to perform an orbital maneuver, either for station keeping or due to a change in mission requirements. In a formation flying application, there are two ways to accomplish such a maneuver. One way would be for all spacecraft in the formation to possess individual thrusting capabilities, with each performing their maneuver separately. A more intriguing scenario is one where only a single craft in the formation possesses thrusting capability, either unintentionally or by design. A combination of electrostatic forces and thrusting could be used to tow the passive spacecraft and perform the necessary orbital maneuvers. This concept could be expanded to extend mission life for an otherwise functional spacecraft that has lost its ability to perform station keeping on its own. Thus, the electrostatic tractor finds utility in non-debris related scenarios, as well.

Perhaps the most similar debris mitigation method to the electrostatic tractor concept is the Ion Beam Shepherd.[12,62] Here, an ion beam is directed onto a debris object, and the resulting momentum transfer is used to modify the debris orbit. This is also a touchless method of debris removal that requires flying at distances on the order of tens of meters. The Ion Beam Shepherd requires a pushing configuration, as opposed to the pulling configuration used for the electrostatic tractor. The pushing configuration has inherently unstable relative motion dynamics, which poses an additional challenge for the relative motion control.[96] If the debris objects are spinning, the ions in the ion beam can be deflected laterally, introducing off-axis forces which affect the orbit in an undesired way. Lastly, the Ion Beam Shepherd requires power levels of kW or more, orders of magnitude more than required for the electrostatic tractor.

1.2.2 Challenges

There are many challenges associated with the electrostatic tractor that need to be considered in order to move the concept forward. One major challenge is the need to autonomously fly only a few craft radii away from tumbling, bus-sized objects for a duration of several months. This must be done in the presence of charging, where an attractive force exists between tug and deputy. While there is an extensive body of research in the area of autonomous rendezvous and docking, in-flight

demonstrations of autonomous, close proximity rendezvous with a non-cooperative object have not been completed.[45,90,115] However, autonomous docking has been completed with cooperative target objects. One such example is the Orbital Express mission, where a servicing satellite (ASTRO) approached, docked with, and transferred fuel to another satellite (NEXTSat) intended to represent a spacecraft in need of servicing.[36] The relative motion sensing was accomplished using a laser-based system, where lasers were fired from ASTRO at retroreflectors on NEXTSat.[46] Images of the laser return were used to provide full 6-DOF relative position and orientation information. This method was successful because NEXTSat was purpose-designed with retroreflectors to provide these measurements. A non-cooperative object will not provide such information.

For a piece of debris, a geometric model will not always be available ahead of time. A sensor suite is required for identifying the deputy object geometry and providing relative position information on the fly for relative motion stabilization. One potential candidate sensor for this purpose is LIDAR, which provides three-dimensional topographical information about measured objects.[23] LIDAR is a technology with spaceflight heritage, and has been used to map the lunar surface,[106] to provide altimetry data on the Itokawa asteroid,,[3,76] and is considered a good candidate for autonomous rendezvous and docking operations.[50] LIDAR was also used by the space shuttle as a navigational aid for docking operations.[40] Obtaining a good geometric model would help with relative motion requirements, and also with estimating charging behavior.

The relative motion of tug and deputy is influenced, of course, by the electrostatic force acting between them. Thus, some knowledge of charging may be required. In charging experiments in space, Langmuir probes are used to provide measurements of spacecraft potential.[65] A tug vehicle equipped with such a device would be able to obtain measurements of its own potential. Also, because the tug is purpose designed for charging, pre-launch analysis of the tug charging dynamics would allow for good characterization of its charging behavior. A targeted debris object, however, would not benefit from such analysis. In practice, it would be a non-trivial effort to measure the deputy charging. Further, uncertainties in deputy material properties only complicate the matter further. While it is not clear at this stage how important knowledge of deputy charging, and the

resulting electrostatic force, is, it must be kept in mind moving forward.

The space environment around earth contains species of charged particles: negatively charged electrons and positively charged ions. In the presence of a highly charged spacecraft, these particle species rearrange in the resulting electric field.[11] For example, a negatively charged spacecraft will attract ions and repel electrons, resulting in a higher ion density and lower electron density in the near vicinity. The scale over which this rearrangement occurs is characterized by the Debye length, and this phenomenon results in a shielding of the electrostatic potential in space around the spacecraft. Correspondingly, the electrostatic force between neighboring charged objects is also reduced in the presence of a plasma. In lower earth orbit, the Debye lengths range from millimeters to centimeters, while GEO Debye lengths typically range from tens to hundreds of meters. For this reason the electrostatic tractor is not suitable for use in LEO debris remediation, and is only suitable for mitigation at higher orbits like GEO.

Modeling charging behavior for a typical satellite with a non-simple geometry and a variety of construction materials is not a simple task. The most accurate approach to such analysis is the use of numerical tools like the NASA/Air Force Spacecraft Charging Analysis Program (NASCAP-2K).[72] NASCAP-2K allows the user to define three-dimensional spacecraft geometries, as well as material properties, and models charging interactions between the plasma environment and spacecraft surfaces. The downside to using such a numerical tool is the computation time. A typical reorbiting time is on the order of several months; incorporating a spacecraft charging model into a simulation of the orbital dynamics over this time period is prohibitive if a program like NASCAP-2K is used, because thousands of charging simulations would be required. Simpler, analytic current-based charging models may be used instead, but this approach is only accurate for simple geometries like spheres and cylinders.[67] Of course, the tradeoff comes in computation time. Using a simple current balance model allows for a full orbital dynamics simulation that incorporates first-order realistic charging behavior.

1.3 Literature Review

1.3.1 Coulomb Formation Flying and Relative Motion Studies

Due to the nature of the electrostatic forces used for tugging, the electrostatic tractor concept may be considered a subset of the much larger field of Coulomb formation flying.[60,99] The use of electrostatic forces for spacecraft formation maintenance, called Coulomb formation flying, is a relatively new and intriguing area of research with a wealth of developments occurring in the last decade.[47,60,61,98,104] The use of electrostatic actuation in space is discussed as early as 1966 by Cover et. al. in Reference 29 as a means for inflating lightweight gossamer structures for space-based antenna systems. The Coulomb formation flying (CFF) concept revolves around active charge control of spacecraft to several kiloVolts; at separation distances of tens of meters, these charge levels result in milliNewtons of force. Through careful application of charging histories, the relative motion of spacecraft is affected for formation maintenance and reconfiguration.[83,91,113] A major benefit of CFF lies in its fuel and power efficiency. In the geosynchronous orbit regime, only 10s of Watts are required to achieve the required charge levels, with specific impulses of $10^{10} - 10^{13}$ seconds.[29,60,99] Furthermore, active charge control to the levels required for CFF has been demonstrated in flight. For example, on the SCATHA mission a spacecraft potential of 4 kV was achieved through emission of an electron beam at a current of 13 mA.[64,78] In addition to free flying formation maintenance, the use of spacecraft charging has been suggested as a means to inflate tethered Coulomb structures.[103,104] Here, spacecraft are connected by physical tethers and repulsive electrostatic forces are used to generate tension in the tethers and provide rigidity to the structure.

The electrostatic tractor uses a combination of electrostatic forces and thrusting to perform a deputy orbit modification. There is some prior work that considers similar types of hybrid control, making use of both thrusting and electrostatic forces simultaneously.[84,94] Here, thrusters are introduced to provide extra control authority for formation maintenance purposes, where the line-of-sight electrostatic forces are insufficient. Thrusting is used only to help maintain the desired

formation shape, and reorbiting maneuvers are not considered.

The seminal work regarding the electrostatic tugging concept considers an application to GEO debris mitigation.[98] Here, variational equations are used to predict possible semi-major axis changes for debris objects under the influence of electrostatic tugging. No consideration is given to relative motion dynamics or charge control. Rather, an open loop study is performed to assess the feasibility of raising a debris object on a circular geosynchronous orbit to a higher graveyard orbit. The results show that an object weighing several tons could be reorbited in a period of a few months. A follow on study considers the relative motion and derives a control law to stabilize the relative positions of tug and debris during the towing period using a spherical coordinate frame description, best suited for a leader-follower along track arrangement of tug and deputy.[44]

At its core, the electrostatic tug is a formation flying problem. In relative motion studies of spacecraft formations, the Hill frame coordinates are a commonly used relative motion description between a chief and a deputy craft. These coordinates are a cartesian description, and applying them to the special case of a circular chief orbit with small separation distances results in the Clohessy-Wiltshire (CW) equations.[24] For some applications, a curvilinear coordinate frame is preferred and used to describe the relative motion; this curvilinear coordinate frame is typically a spherical frame, defined by the separation distance between the craft and two angles which provide information about the orientation of the line of sight vector from the chief to deputy.[30] Another relative motion description uses differential orbital elements.[15,53] Here, one craft in the formation is specified as the reference craft, and all other craft in the formation are defined by differencing their orbital elements with those of the reference. The relative motion problem has also been parameterized and studied using a quaternion formulation.[25]

In this dissertation, motion with respect to a circular chief orbit is investigated using a novel relative motion description. The electrostatic forces used for tugging are inversely proportional to the separation distance between tug and deputy squared. As such, it is advantageous to chose a relative motion description that isolates separation distance directly as a coordinate. Furthermore, due to the close (10s of meters) proximity required for tugging, it would be beneficial to be able

to feedback directly on separation distance to prevent collision. If a circumnavigation is required, the separation distance is maintained while the tug safely flies around the deputy. In prior work considering relative motion in the electrostatic tractor application, spherical coordinates are used for this purpose.[44] When it comes to general reorbiting maneuvers beyond simple semi-major axis corrections, however, spherical coordinates are not ideal. There are certain relative orientations, necessary for corrections to some orbital elements, at which spherical coordinates suffer kinematic singularities. To that end, new relative motion descriptions are sought that utilize separation distance directly, while avoiding the kinematic singularities that arise from the use of spherical coordinates. Another application that would benefit from such a study is the Ion Beam Shepherd method of large debris removal.[12,13,62] Here, an ion beam is focused onto a debris object, and the resulting momentum transfer is used for orbit modification. The ion-beam shepherd method of large debris removal method also requires close proximity flying on the order of dozens of meters where the separation distance errors should be controlled more strongly than the relative heading errors. The space based laser ablation and electrostatic despin concepts also have similar close-flying requirements, with separation distances under twenty meters.[101,107]

1.3.2 Spacecraft Charging and the Plasma Environment

Due to the potential impacts of spacecraft charging on operations and spacecraft lifetime, much work has been performed in this area.[7,21,31,38,58,78] Typically, these studies focus on a single satellite in orbit and investigate natural charging events that occur as a result of the space weather environment. A serious concern for spacecraft that experience differential charging across their outer surface is electrostatic discharge (ESD) events, where arcing occurs between different substructures possessing a significant surface potential difference.[58] These ESD events can be destructive to electronic hardware. Recent studies indicate that large satellites in GEO may experience many thousands of discharges over their lifetimes.[21] With the electrostatic tug concept, the electron beam is used to raise the absolute potential of the vehicle, and thus avoids the differential charging issues. Current GEO spacecraft construction practice ensures that all outer surfaces are interconnected to a

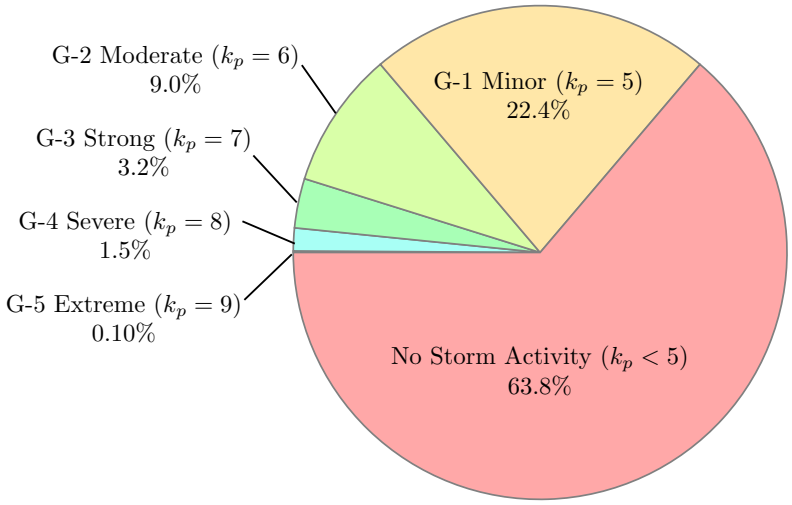

Figure 1.2: Percent of days in an 11 year solar cycle for which various geomagnetic storm levels occur. Data adapted from Reference 87

common ground, thus minimizing differential charging issues.[93] This also has the benefit of helping to distribute charge over a deputy structure, which improves electrostatic tractor performance. For electrostatic tugging, potential levels on the order of tens of kiloVolts are required.[96] While certainly the near proximity of highly charged spacecraft raises a concern of potential arcing between tug and debris, in GEO arcing occurs over distances of a few centimeters for kiloVolt levels of potential difference.[20] This is many times smaller than the separation distances considered, so arcing between tug and debris is not a concern.

The charging of a spacecraft is dependent on the space plasma environment.[67,81] Because of the potential threats to mission viability caused by charging events, much work has been done to characterize the space weather environment both in LEO and GEO.[32,59] The plasma environment is typically characterized by two parameters: density and temperature. The LEO plasma environment is much more cold and dense than in GEO, with typical densities ranging from $10^4 - 10^6$ particles/cm^{-3} and corresponding temperatures below 1 eV. In GEO, the plasma densities are orders of magnitude smaller, ranging from $.1 - 10$ particles/cm^{-3}. Depending on geomagnetic storm activity, ion temperatures may range from below 100 eV to 20 keV or more. Electron temperatures are typically above 1 keV, and may reach tens of keV depending on storm activity. The severity of

geomagnetic storms is classified using the k_p index, which is based on the observed variation in the degree of irregular magnetic activity throughout each day, observed at various ground stations.[9] The k_p index utilizes an integer scale ranging from 0-9, and values of 5 and up indicate that a geomagnetic storm is occurring. The National Oceanic and Atmospheric Administration (NOAA) has also developed a scale for classifying the severity of geomagnetic storms.[87] The scale ranges from G-1 minor storms ($k_p = 5$) to G-5 extreme storms ($k_p = 9$). The NOAA scale provides information about expected impacts to spacecraft for different storm levels. In a minor storm (G-1, $k_p = 5$), minimal impacts to spacecraft operations can be expected. At the other end of the spectrum, an extreme storm (G-5, $k_p = 9$) may cause extensive surface charging, loss of attitude, and problems with communications and satellite tracking. Fortunately, stronger storms only occur a few times per eleven year solar cycle. The frequency of occurrence for the various storm conditions in a typical solar cycle is shown in Figure 1.2. The vast majority of the time ($> 85\%$), there is either no storm activity or a minor storm occurrence.

Geomagnetic storm activity has been linked to spacecraft anomalies for vehicles operating in GEO.[22,34] Such anomalies include loss of attitude, power failure, glitches in software, short circuits in the electrical system, processor failure, and even malfunctions of the thruster systems. The severity of these events has ranged from temporary outages lasting no more than a few hours to total loss of operations. While exact causes behind such anomalies are often not found, a correlation does exist between storm activity and the frequency of these events. Further, the majority of the anomalies were recorded between local midnight and late morning. This is the same region where the highest natural charging events were recorded on the ATS-5 and ATS-6 missions.[31,89]

Because of the potential danger to mission operations posed by uncontrolled charging, numerous methods for both passive and active charge control have been developed.[68] When high-level charging events occur, a spacecraft will charge negatively owing to the presence of high energy electrons. Thus, charge control methods are used to return to a more neutral potential. One passive method for charge control is the use of a sharp spike connected to a conductive surface. This creates an electric field at the tip of the spike, which will emit electrons when the field is

high enough, helping to reduce the negative charge buildup on the satellite. This method, however, only allows for self-charge control, and would not enable charge transfer to a neighboring object. Another, more active, method of charge control is the use of a hot filament made of high-melting point materials. At high temperatures below the filament melting point, electrons are emitted, which reduces the charging of the spacecraft. The sharp spike and hot filament methods are only able to draw electrons from, and subsequently reduce the charging of, the conducting spacecraft ground. These methods do not help with the charging of dielectric materials on the spacecraft, and differential charging may result. This differential charging may result in arcing between spacecraft surfaces, which can be destructive to onboard electronics and solar panels.[20,21] To help mitigate dielectric charging, partially conducting paint is applied on dielectric surfaces.[93]

A more active method of charge control that provides more control authority is the emission of electron and ion beams.[66,68,71,88] This may be done with ejection of electrons or ions, or both simultaneously. To drive an electron beam, electrons are drawn from the spacecraft ground and expelled. For a negatively charged spacecraft, these electrons are lost, lowering the vehicle potential. Electron beam emission does have the problem of only discharging the conductive ground, and not dielectric materials, which can result in differential charging. It seems that emitting positively charged ions would actually drive the spacecraft to a higher negative potential, owing to the loss of positive charge. However, this is not necessarily the case. If low energy ions are emitted, they will be recaptured by the negatively charged spacecraft. This method, which was used on the SCATHA mission, can only lower the vehicle potential to the energy level of the emitted ions.[64]

A spacecraft may take advantage of the benefits of electron and ion emission by emitting both simultaneously. Here, electrons and ions are emitted together in a low energy plasma. Electrons are lost, and the low energy ions are recollected. This method was implemented on a geosynchronous Defense Satellite Communication System (DSCS) satellite as part of an autonomous charge control system, which was able to detect the onset of high charging events and initiate plasma expulsion for charge mitigation.[79] The International Space Station (ISS) also makes use of plasma emission to mitigate charging issues; the plasma helps to serve as a ground between the ISS structure, which

can charge to over -100 V relative to the local space environment, and the ionosphere.[17,37,57]

For the electrostatic tractor application, a method of active charge control is needed. Charged particle beams are the most ideal candidates for this purpose. Emitting a high-energy beam (10s of keV) at sufficient current levels will enable the tug to reach high potentials. Either an ion or electron beam may be used, though an electron beam is preferred. Directing the beam onto the deputy provides a current that will affect the deputy charging, much like the the natural charging that occurs due to the plasma environment. The vast majority of prior work with Coulomb formations merely assume either a charge or a potential on the different spacecraft in the formation, without actually modeling the mechanism for and environmental influences on achieving the charging.[44,47,82,96,101,113] The electrostatic tractor performance is dependent on the charging that is achieved with electron or ion beam emission, and it is important to characterize the charge transfer process. Reference 101 presents a first-order charging model to compute potentials on tug and deputy as a function of various environmental current sources, applied to the electrostatic tractor problem. Assuming an electron beam is used for charge control, one particular tug and deputy configuration is considered, and the resulting electrostatic forces are computed for specific space weather conditions. The work does not consider the impact of changing space weather conditions on tractor performance, or different sizes of tug and deputy. This first-order charging model provides the tools needed to analyze the general charging trends that may be encountered for the electrostatic tractor application, and is used extensively in the current study.

1.4 Scope of the Research

The electrostatic tractor concept is still in the early stages of investigation. There are many potential avenues of related research that could be pursued. The purpose of the study at hand is to address some of the fundamental questions related to the electrostatic tractor, namely:

(1) How might the relative motion of tug and deputy be controlled autonomously?

(2) What levels of reorbiting performance are expected for a variety of orbital corrections?

(3) What are some general trends that may be encountered during the charge transfer process?

Helping to answer these questions would go a long way towards verifying the feasibility of the electrostatic tractor. The different aspects of this study can be subdivided into three major tasks. The first task will focus on the relative motion control of tug and deputy in the presence of charging, using a novel relative motion description. The second seeks to identify achievable orbital element corrections using the electrostatic tug. Lastly, the third objective focuses on identifying the impacts of space weather variations and relative sizing on the charge transfer process, and considers whether performance may be improved by emitting an electron and ion beam simultaneously from the tug. The scope for each of these three tasks is detailed below.

1.4.1 Relative Motion Control

Performing deputy orbital corrections dictates certain requirements on the relative positioning of tug and deputy. To meet these requirements, the relative equations of motion are derived and a control law is developed to stabilize the relative motion of tug and deputy. Thrusters are used to affect this relative motion, and it is assumed that the tug has full three-dimensional control authority. If the tug thrusters impinge on the deputy, then the electrostatic tractor will not work, as a repulsive force will result. Thus, it is assumed that the thrusters are angled in such a way that no impingement occurs. In practice, this could be accomplished by angling thruster nozzles, or by installing the thrusters on booms extended from the tug vehicle. The main research tasks are:

(1) Develop a novel relative motion description that isolates separation distance as a coordinate.

(2) Derive a feedback control law to stabilize the relative motion of tug and deputy using this novel description.

(3) Characterize the impact of improperly modeled charges on control performance.

(4) Perform full 9-DOF (3 for the tug, 6 for the deputy) relative motion simulation, incorporating the charge transfer model.

1.4.2 Analysis of Orbital Corrections

To understand the feasibility of applying the electrostatic tug to general reorbiting maneuvers, analytic predictions of achievable orbital element changes are sought. For the case of two-body orbital dynamics, Gauss's variational equations provide a method to analyze the evolution of orbital elements resulting from various forces acting on the spacecraft (thrusters, electrostatic forces, etc.).[16,97] The following items are addressed:

(1) Use Gauss's variational equations to obtain analytic predictions for achievable orbital element corrections.

(2) Investigate changes in radius of perigee (for eccentric orbits), eccentricity, inclination, and right ascension of the ascending node.

(3) Analyze the performance of electrostatic tugging for GEO slot changes (longitude corrections).

(4) Characterize the impacts of tug repositioning during towing phases.

For this analysis, several assumptions are invoked. First, only two-body dynamics are considered, which allows for the application of Gauss's variational equations. Second, the electrostatic forces are assumed to be piecewise constant in magnitude and direction throughout the duration of the reorbiting maneuver. Lastly, simplifying assumptions are made about the geometries of tug and deputy to enable analytic force calculations.

1.4.3 Characterizing the Charge Transfer Process

Modeling the charge transfer process is, perhaps, the area most ripe for investigation. There are many factors that influence charging, and the space weather environment is highly dynamic. Further, different materials exhibit different charging behavior. Providing a very detailed analysis of the charging for complex tug and deputy geometries is beyond the scope of this research. Rather,

the goal of this study is to identify general trends in charging behavior that directly affect tractor performance. The completed tasks are:

(1) Study the impact of nominal variations in GEO space weather that occur during a typical, quiet day on tractor performance.

(2) Investigate the effects of geomagnetic storms on tractor performance.

(3) Characterize the impact of relative sizing between tug and deputy on charge transfer and tractor performance.

(4) Investigate the simultaneous use of electron and ion beam emission for improving charge transfer performance.

(5) Consider the effects of emitted deputy photo- and secondary electrons on tug charging.

The goal of the study is to assess the feasibility of the electrostatic tugging concept and identify important phenomena that impact the charge transfer process. As such, a high fidelity model of the complex plasma behavior that occurs during the charging process is not needed. Rather, first order predictions of charging behavior are sufficient.

Chapter 2

Relative Motion Description and Control

2.1 Electrostatic Force Model

Before investigating the relative motion, the electrostatic force model used throughout the thesis is introduced. The performance of the electrostatic tug is dependent on the electrostatic force in place between the tug and deputy. To allow for analytic expressions, the tug and deputy object are treated geometrically as spheres, and are assumed to be perfectly conducting. The potential on the tug object is a result of its own charge and the potential due to the charged deputy object as[96]

$$\phi_T = k_c \frac{q_T}{r_T} + k_c \frac{q_D}{\rho}, \tag{2.1}$$

where $k_c = 8.99 \times 10^9$ Nm^2/C^2 is the Coulomb constant, ρ is the distance between tug and deputy, q_T is the charge on the tug, q_D is the charge on the deputy, and r_T is the radius of the tug craft. Similarly, the potential on the deputy object is computed as

$$\phi_D = k_c \frac{q_D}{r_D} + k_c \frac{q_T}{\rho}, \tag{2.2}$$

where r_D is the radius of the deputy object.

If the potentials on the tug and deputy are controlled, then the above relationships may be rearranged to solve for charge,[96]

$$\begin{bmatrix} q_T \\ q_D \end{bmatrix} = \frac{\rho}{k_c(\rho^2 - r_T r_D)} \begin{bmatrix} r_T\rho & -r_T r_D \\ -r_T r_D & r_D\rho \end{bmatrix} \begin{bmatrix} \phi_T \\ \phi_D \end{bmatrix}. \tag{2.3}$$

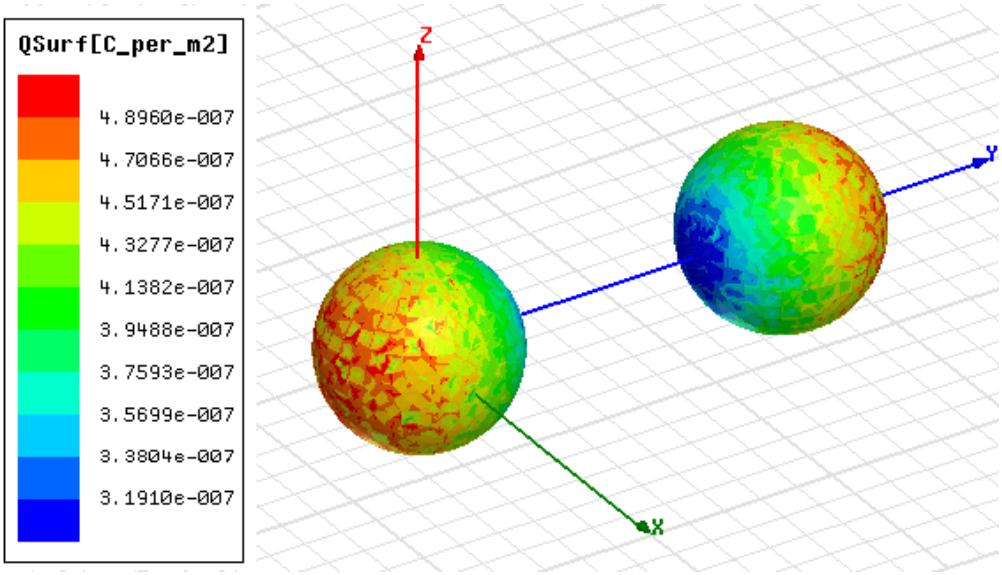

Figure 2.1: Maxwell 3-D computation of non-uniform charge distribution on two spheres charged to +30 kV.[109]

After computing the charges, the electrostatic force between tug and deputy is computed using

$$F_c = k_c \frac{q_T q_D}{\rho^2}. \tag{2.4}$$

Note that this force may be either attractive or repulsive depending on the polarity of the potentials of the tug and deputy. For the electrostatic tractor application, the tug may be employed either in a pushing or pulling configuration. In the pushing configuration, a repulsive force is applied with the tug behind the deputy object. In the pulling configuration, an attractive force is used with the tug ahead of the deputy object. As detailed in Reference 96, it is advantageous to use the pulling configuration in terms of electrostatic force magnitudes and stability of the tug-deputy alignment. In this study, only the pulling configuration will be considered, with tug and deputy charged to opposite polarity. This is also the easiest configuration to achieve with charge transfer because only an electron beam is needed. To use the pushing configuration, tug and deputy must be charged to the same polarity, which would require the tug to emit an ion beam to charge itself and an electron beam for charge control of the deputy.

It is worth noting that the preceding electrostatic force model does not account for induced

effects.[108] As two charged spheres are brought in close proximity, the charge distribution becomes non-uniform on the surfaces as illustrated in Figure 2.1. In the case of opposite polarity, more charge will accumulate on the near sides of the spheres. When the spheres are the same polarity, the charges will accumulate more on the far sides of the spheres. This has the effect of increasing the electrostatic force for the attractive case, and decreasing it in the case of repulsion. The induced charge effect, however, is most apparent at shorter separation distances of less than a few sphere radii. For the electrostatic tug concept, larger separation distances (>10 m) are considered where these induced effects are negligible.[96] Thus, the capacitance model in Eq. (2.3) is a sufficient approximation for the study at hand.

Due to the space weather environment, some shielding of this electrostatic force will occur. The distance over which this shielding is prevalent is described by the Debye length of the local plasma.[11] The space weather conditions considered in this study yield Debye lengths that are on the order of tens of meters. However, because of the high potential levels obtained by tug and deputy, the Debye shielding effect will be several times smaller than predicted by the standard Debye length calculation. As discussed in References 80 and 111, objects charged to tens of kiloVolts in the space environment experience effective Debye lengths several times larger. Looking specifically at this phenomenon as it pertains to charging in quiet GEO space weather conditions, the effective Debye lengths are predicted to be roughly 5 times larger than the classic Debye shielding model predicts.[111] The shortest Debye lengths considered here range from 15-35 meters, leading to effective Debye lengths over 75 meters. This means that the space weather environment will not contribute significant shielding of the electrostatic force below distances of 75 meters. Because the separation distances considered here are less than 20 meters, the impacts of Debye shielding are insignificant and will not be included in the force model.

2.2 Clohessy-Wiltshire Equations

Now, the relative motion of the tug with respect to the deputy is studied. This scenario is depicted in Figure 2.2. Here, $\boldsymbol{r}_d$ describes the inertial position of the deputy and $\boldsymbol{r}_t$ describes the

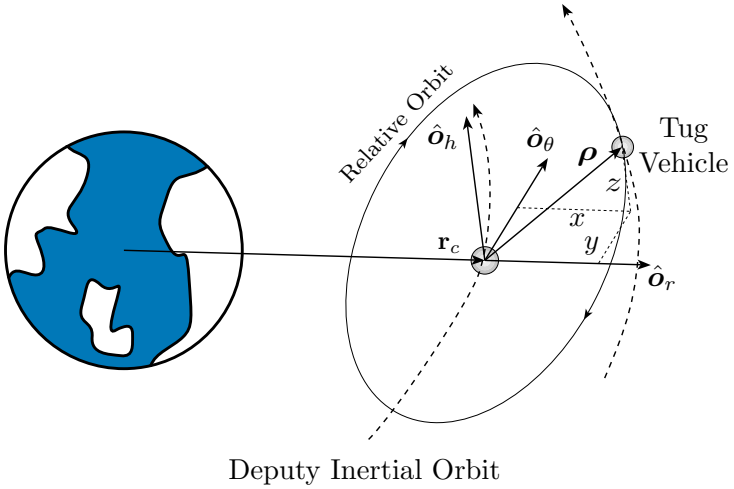

Figure 2.2: Relative motion of tug and deputy, illustrated using rotating Hill frame

position of the tug. The relative position, $\boldsymbol{\rho}$, is defined as

$$\boldsymbol{\rho} = \boldsymbol{r}_t - \boldsymbol{r}_d. \tag{2.5}$$

Of interest is how this relative position evolves under the influence of gravity, electrostatic forces, and tug thrusting. One relative motion description frequently used is the cartesian Hill-frame coordinate system, illustrated in Figure 2.2. The axes of the Hill frame, denoted as $\mathcal{H}$, are computed using

$$\hat{\boldsymbol{o}}_r = \frac{\boldsymbol{r}_d}{r_d}, \qquad \hat{\boldsymbol{o}}_\theta = \hat{\boldsymbol{o}}_h \times \hat{\boldsymbol{o}}_r, \qquad \hat{\boldsymbol{o}}_h = \frac{\boldsymbol{r}_d \times \dot{\boldsymbol{r}}_d}{|\boldsymbol{r}_d \times \dot{\boldsymbol{r}}_d|}. \tag{2.6}$$

The Hill frame is convenient for describing relative motion because the inertial position of the deputy object is described completely by

$$\boldsymbol{r}_d = r_d \hat{\boldsymbol{o}}_r. \tag{2.7}$$

Furthermore, the angular velocity of the Hill frame with respect to an inertial frame is given by

$$\boldsymbol{\omega}_{\mathcal{H}/\mathcal{N}} = \dot{f}\hat{\boldsymbol{o}}_h, \tag{2.8}$$

where the script $\mathcal{N}$ refers to an inertial frame, and $\dot{f}$ is the instantaneous true anomaly rate. Using the Hill frame, the position of the tug craft may be expressed as

$$\boldsymbol{r}_t = \boldsymbol{r}_d + \boldsymbol{\rho} = (r_d + x)\hat{\boldsymbol{o}}_r + y\hat{\boldsymbol{o}}_\theta + z\hat{\boldsymbol{o}}_h, \tag{2.9}$$

where x, y, and z are Hill frame components of the relative position vector $\boldsymbol{\rho}$. Using this Hill-frame description, the relative equations of motion are found to be[97]

$$\ddot{x} - 2\dot{f}\left(\dot{y} - y\frac{\dot{r}_d}{r_d}\right) - x\dot{f}^2 - \frac{\mu}{r_d^2} = -\frac{\mu}{r_t^3}(r_d + x) + u_x \tag{2.10a}$$

$$\ddot{y} + 2\dot{f}\left(\dot{x} - x\frac{\dot{r}_d}{r_d}\right) - y\dot{f}^2 = -\frac{\mu}{r_t^3}y + u_y \tag{2.10b}$$

$$\ddot{z} = -\frac{\mu}{r_t^3}z + u_z, \tag{2.10c}$$

where u_x, u_y, and u_z are control accelerations in the x, y, and z directions, respectively.

In Eq. (2.10) no assumptions have been made about the distance between tug and deputy, and no restrictions have been placed on the deputy orbit. Thus, these equations are valid for arbitrary relative motion. In the electrostatic tractor application, the tug and deputy are flown at separation distances much smaller than the orbit radii. This allows for a linearization of Eq. 2.10 about the deputy motion. If only the case of circular deputy motion is considered, a reasonable assumption for GEO orbits, the true anomaly rate is constant and determined by

$$\dot{f} = \text{constant} = \sqrt{\frac{\mu}{r_d^3}} = n. \tag{2.11}$$

Under these assumptions, the relative equations of motion may be simplified to the well-known Clohessy-Wiltshire (CW) equations[24]

$$\ddot{x} - 2n\dot{y} - 3n^2x = u_x \tag{2.12a}$$

$$\ddot{y} + 2n\dot{x} = u_y \tag{2.12b}$$

$$\ddot{z} + n^2z = u_z, \tag{2.12c}$$

where u_x, u_y, and u_z are the control accelerations of the tug in the Hill-frame. These control accelerations consist of both the thrusters employed by the tug and the electrostatic forces acting between tug and deputy. The CW equations are useful because they have an analytic solution as a function of initial conditions. There are drawbacks, however, that one may encounter when working with these equations. Because the Hill-frame description is cartesian in nature, and orbits form a curvilinear space, the CW equations will not accurately capture the relative motion for

moderately large separation distances. This is due to the fact that the local curvature of the orbit is approximated as linear.

In the CW equations, n represents the mean motion of the deputy object. However, as the deputy object is towed this will no longer be the case. This issue is analyzed in Reference 44; because the electrostatic forces are small (on the order of mN), neglecting the mean motion rate of change does not introduce significant errors into the linearized CW equations. To illustrate this fact, consider the relative magnitudes of $\dot{n}$ and n^2. The rate of change of mean motion is approximated as

$$\dot{n} = \frac{F_c}{m_d r_d}. \tag{2.13}$$

Considering a 1000 kg deputy object in GEO (r_d =42164 km), a 1 mN electrostatic force results in $\dot{n} = 2.37 \times 10^{-14}$ rad/s^2 and $n^2 = 7.29 \times 10^{-5}$ rad^2/s^2. Since $\dot{n}$ is several orders of magnitude below n^2, neglecting these terms does not impact the accuracy of the CW equations significantly. To account for the change in n over time, n is simply replaced with the time-dependent $n(t)$. For the remainder of the relative motion developments, n represents the time-varying mean motion of the deputy orbit.

2.3 Relative Orbit Descriptions using Heading and Separation Distance Measures

2.3.1 The Unit-vector Description

For the electrostatic tractor application, it is of interest to use the separation distance between the tug and deputy directly as a coordinate, breaking up the description of relative motion into a distance and relative orientation measure. To avoid the singularity issues associated with a spherical coordinate description, an alternate method is proposed which uses the separation distance, $L = \rho$, and the unit-vector pointing from deputy to tug, as illustrated in Figure 2.3. This unit-vector is defined as

$$\hat{\boldsymbol{e}} = \frac{\boldsymbol{\rho}}{\rho}. \tag{2.14}$$

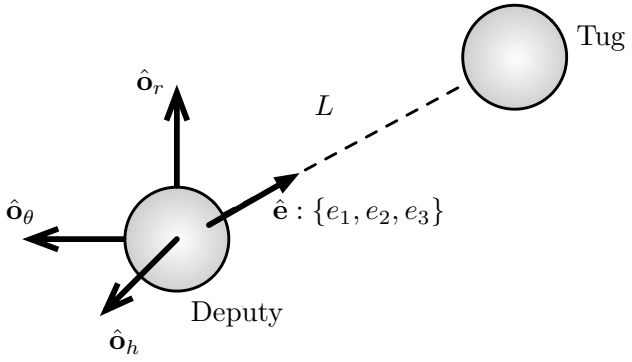

Figure 2.3: Unit-vector description of relative motion

Using this description, the position of the tug with respect to the deputy in Hill frame components is given by

$$\boldsymbol{\rho} = Le_1\hat{\boldsymbol{o}}_r + Le_2\hat{\boldsymbol{o}}_\theta + Le_3\hat{\boldsymbol{o}}_h, \tag{2.15}$$

where e_i are the Hill frame components of $\hat{\boldsymbol{e}}$. The forward and inverse mapping between the cartesian Hill frame components and the unit-vector description is given by

$$\begin{bmatrix} x \\ y \\ z \end{bmatrix} = \begin{bmatrix} Le_1 \\ Le_2 \\ Le_3 \end{bmatrix}, \quad \begin{bmatrix} e_1 \\ e_2 \\ e_3 \end{bmatrix} = \begin{bmatrix} x/L \\ y/L \\ z/L \end{bmatrix} \tag{2.16}$$

with

$$L^2 = x^2 + y^2 + z^2. \tag{2.17}$$

The conversion between the rates is given by

$$\begin{bmatrix} \dot{x} \\ \dot{y} \\ \dot{z} \end{bmatrix} = \begin{bmatrix} \dot{L}e_1 + L\dot{e}_1 \\ \dot{L}e_2 + L\dot{e}_2 \\ \dot{L}e_3 + L\dot{e}_3 \end{bmatrix}, \quad \begin{bmatrix} \dot{e}_1 \\ \dot{e}_2 \\ \dot{e}_3 \end{bmatrix} = \begin{bmatrix} (\dot{x} - \dot{L}e_1)/L \\ (\dot{y} - \dot{L}e_2)/L \\ (\dot{z} - \dot{L}e_3)/L \end{bmatrix} \tag{2.18}$$

with the separation-distance rate determined as

$$\dot{L} = \frac{x\dot{x} + y\dot{y} + z\dot{z}}{L}. \tag{2.19}$$

Geometrically, the components e_i may be interpreted as angle measures between the unit-vector $\hat{\boldsymbol{e}}$ and the Hill-frame axes $\hat{\boldsymbol{o}}_r$, $\hat{\boldsymbol{o}}_\theta$, and $\hat{\boldsymbol{o}}_h$. More specifically, they represent the direction

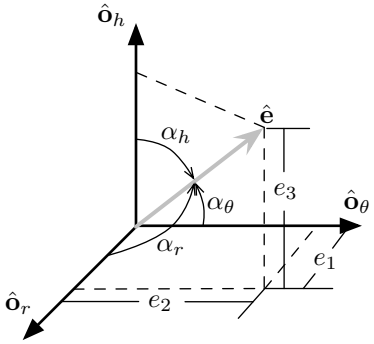

Figure 2.4: The unit-vector components are equivalent to the cosines of the angles between $\hat{\boldsymbol{e}}$ and the Hill frame axes

cosines of $\hat{\boldsymbol{e}}$ with respect to the Hill frame. If the angle between $\hat{\boldsymbol{e}}$ and the $\hat{\boldsymbol{o}}_i$ axis is denoted as α_i, as illustrated in Figure 2.4, then the components of $\hat{\boldsymbol{e}}$ are equivalent to

$$\begin{bmatrix} e_1 \\ e_2 \\ e_3 \end{bmatrix} = \begin{bmatrix} \cos\alpha_r \\ \cos\alpha_\theta \\ \cos\alpha_h \end{bmatrix}. \tag{2.20}$$

Considering the relationship between the cartesian Hill frame coordinates and the unit-vector description, an apparent singularity occurs at $L = 0$. This singularity is a result of the non-uniqueness of the unit-vector at this separation distance. In fact, when the separation distance is zero, any arbitrary unit-vector will appropriately convert the unit-vector description into the cartesian coordinates. While this presents an issue mathematically, it is of little practical concern because a separation distance of zero is impossible with actual craft. The unit-vector description is well defined everywhere else, and is thus a good candidate for describing arbitrary relative motion.

With the unit-vector description, four parameters are used to describe a three-dimensional location. Similar to the use of the 4-dimensional Euler parameter (EP) set to describe a three dimensional attitude, there must be a constraint on the parameters. In this case, the unity constraint

$$e_1^2 + e_2^2 + e_3^2 = 1 \tag{2.21}$$

must be satisfied at all times. Differentiating this constraint twice with respect to time yields

$$e_1\ddot{e}_1 + e_2\ddot{e}_2 + e_3\ddot{e}_3 + \dot{e}_1^2 + \dot{e}_2^2 + \dot{e}_3^2 = 0. \tag{2.22}$$

Considering Eq. (2.22), it appears that singularities may present a problem when one of the vector components is zero. However, when combined with the relative motion differential equations, this singularity will vanish.

Another parallel with the Euler parameter attitude description is the issue of uniqueness. When the four dimensional Euler parameters are used to describe attitude, there are two sets that describe the same orientation. With the unit-vector relative motion description, there are two sets of parameters that describe the exact same relative position. In addition to the $\boldsymbol{\rho} = L\hat{\boldsymbol{e}}$ description detailed above, the same location may be obtained using $\boldsymbol{\rho} = -L(-\hat{\boldsymbol{e}})$. This non-uniqueness has an important implication for the $\boldsymbol{\sigma}$ set introduced in the next section.

To determine the relative equations of motion, Eqs. (2.16) and (2.18) are substituted into Eq. (2.12) and the constraint in Eq (2.22) is used to yield

$$\begin{bmatrix} \ddot{L} \\ \ddot{e}_1 \\ \ddot{e}_2 \\ \ddot{e}_3 \end{bmatrix} = [f(L, \dot{L}, \hat{\boldsymbol{e}}, \dot{\hat{\boldsymbol{e}}})] + [G_e]^{\mathcal{H}}\boldsymbol{u} \tag{2.23}$$

where

$$[f(L,\dot{L},\hat{\boldsymbol{e}},\dot{\hat{\boldsymbol{e}}})] = \begin{bmatrix} L\left(2n(e_1\dot{e}_2 - e_2\dot{e}_1) + n^2(3{e_1}^2 - {e_3}^2) + \dot{e}_1^2 + \dot{e}_2^2 + \dot{e}_3^2\right) \\ e_1\left(2ne_2\dot{e}_1 + n^2\left(3{e_2}^2 + 4{e_3}^2\right) - \dot{e}_1^2 - \dot{e}_2^2 - \dot{e}_3^2\right) - 2n{e_1}^2\dot{e}_2 + 2n\dot{e}_2 + 2\frac{\dot{L}}{L}\left(ne_2 - \dot{e}_1\right) \\ e_2\left(2n(e_2\dot{e}_1 - e_1\dot{e}_2) + n^2({e_3}^2 - 3{e_1}^2) - \dot{e}_1^2 - \dot{e}_2^2 - \dot{e}_3^2\right) - 2n\dot{e}_1 - 2\frac{\dot{L}}{L}\left(ne_1 + \dot{e}_2\right) \\ -e_3\left(\left(\dot{e}_1 - ne_2\right)^2 + 2ne_1\dot{e}_2 + 4n^2{e_1}^2 + \dot{e}_2^2 + \dot{e}_3^2\right) - 2\dot{e}_3\frac{\dot{L}}{L} \end{bmatrix} \tag{2.24a}$$

$$[G_e] = \frac{1}{L}\begin{bmatrix} Le_1 & Le_2 & Le_3 \\ 1-e_1^2 & -e_1e_2 & -e_1e_3 \\ -e_1e_2 & 1-e_2^2 & -e_2e_3 \\ -e_1e_3 & -e_2e_3 & 1-e_3^2 \end{bmatrix} = \begin{bmatrix} \hat{\boldsymbol{e}}^T \\ \frac{1}{L}\left([I] - \hat{\boldsymbol{e}}\hat{\boldsymbol{e}}^T\right) \end{bmatrix} \tag{2.24b}$$

$${}^{\mathcal{H}}\boldsymbol{u} = \begin{bmatrix} u_x \\ u_y \\ u_z \end{bmatrix} \tag{2.24c}$$

Note that the only singularity in Eq. (2.23) occurs when $L = 0$. For reasons discussed above, this is of little concern for the scope of this study. The unit-vector description provides practically non-singular equations of motion that use the separation distance and a redundant set of orientation parameters to describe relative motion. In this manner, the singular issues that plague the spherical frame description are avoided while still maintaining a direct measure of the distance between the tug and deputy.

2.3.2 The σ-Set Relative Motion Description

The unit-vector description detailed previously is inspired by the Euler parameter attitude description. Now, an additional relative motion description is considered which is inspired by modified Rodrigues parameters (MRPs).[97] The unit-vector description is used to define new orientation parameters that reduce the relative motion description from 4 parameters ($\boldsymbol{L}$, $\hat{\boldsymbol{e}}$) to three. Similar to the manner in which MRPs are defined using the Euler parameter set, a new relative motion

orientation description is defined using the unit-vector components. The $\boldsymbol{\sigma}$-set contains L, the separation distance, and two orientation parameters defined as

$$\begin{bmatrix} \sigma_1 \\ \sigma_2 \end{bmatrix} = \frac{1}{1+e_1} \begin{bmatrix} e_2 \\ e_3 \end{bmatrix} \tag{2.25}$$

The once-redundant unit-vector description is used to define a new, minimal-set description of relative motion. The inverse mapping from the $\boldsymbol{\sigma}$-set to unit-vector components is

$$\begin{bmatrix} e_1 \\ e_2 \\ e_3 \end{bmatrix} = \frac{1}{1+\sigma^2} \begin{bmatrix} 1-\sigma^2 \\ 2\sigma_1 \\ 2\sigma_2 \end{bmatrix}, \tag{2.26}$$

where $\sigma^2 = \sigma_1^2 + \sigma_2^2$. Using Eq. (2.16), the mapping between $\boldsymbol{\sigma}$-set and Hill frame coordinates is determined to be

$$\begin{bmatrix} x \\ y \\ z \end{bmatrix} = \frac{L}{1+\sigma^2} \begin{bmatrix} 1-\sigma^2 \\ 2\sigma_1 \\ 2\sigma_2 \end{bmatrix}. \tag{2.27}$$

Taking the derivative with respect to time yields the velocity mapping

$$\begin{bmatrix} \dot{x} \\ \dot{y} \\ \dot{z} \end{bmatrix} = \frac{\dot{L}}{1+\sigma^2} \begin{bmatrix} 1-\sigma^2 \\ 2\sigma_1 \\ 2\sigma_2 \end{bmatrix} + \frac{2L}{(1+\sigma^2)^2} \begin{bmatrix} -2\dot{\boldsymbol{\sigma}}^T\boldsymbol{\sigma} \\ (1-\sigma_1^2+\sigma_2^2)\dot{\sigma}_1 - 2\sigma_1\sigma_2\dot{\sigma}_2 \\ (1+\sigma_1^2-\sigma_2^2)\dot{\sigma}_2 - 2\sigma_1\sigma_2\dot{\sigma}_1 \end{bmatrix}. \tag{2.28}$$

Inverting the above relationships, the mapping from Hill-frame coordinates to $\boldsymbol{\sigma}$-set is found to be

$$\begin{bmatrix} \sigma_1 \\ \sigma_2 \end{bmatrix} = \frac{1}{x+L} \begin{bmatrix} y \\ z \end{bmatrix}, \tag{2.29}$$

with the corresponding velocity mapping

$$\begin{bmatrix} \dot{\sigma}_1 \\ \dot{\sigma}_2 \end{bmatrix} = \frac{1}{x+L} \begin{bmatrix} \dot{y} \\ \dot{z} \end{bmatrix} - \frac{\dot{x}+\dot{L}}{(x+L)^2} \begin{bmatrix} y \\ z \end{bmatrix}. \tag{2.30}$$

To obtain the equations of motion for the $\boldsymbol{\sigma}$ set, the above relationships are inserted into the CW equations. The result is expressed in the form

$$\begin{bmatrix} \ddot{L} \\ \ddot{\sigma}_1 \\ \ddot{\sigma}_2 \end{bmatrix} = \begin{bmatrix} h_L \\ h_{\sigma_1} \\ h_{\sigma_2} \end{bmatrix} + [G_\sigma]^{\mathcal{H}}\boldsymbol{u}, \tag{2.31}$$

where

$$h_L = \frac{L}{(1+\sigma^2)^2}\Big[3n^2(\sigma_1^4+\sigma_2^4+1)+4\dot{\sigma}_1 n - 2n\sigma_2^2(5n+2\dot{\sigma}_1)+2n\sigma_1^2(3n(-1+\sigma_2^2)+2\dot{\sigma}_1) + 8n\sigma_1\sigma_2\dot{\sigma}_2 + 4\dot{\boldsymbol{\sigma}}^T\dot{\boldsymbol{\sigma}}\Big]$$

$$h_{\sigma_1} = -\frac{1}{2L(1+\sigma^2)}\Big[-6n^2L\sigma_1^3+2n\sigma_1^4\dot{L}+4\sigma_1^2\dot{L}(n+\dot{\sigma}_1)-\left(1+\sigma_2^2\right)\dot{L}\left(2n\sigma_2^2-2(n+2\dot{\sigma}_1)\right) - 8L\sigma_2(n+\dot{\sigma}_1)\dot{\sigma}_2+2L\sigma_1\left(3n^2-5n^2\sigma_2^2-2\dot{\sigma}_1^2+2\dot{\sigma}_2^2\right)\Big]$$

$$h_{\sigma_2} = \frac{1}{2L(1+\sigma^2)}\Big[-4n\sigma_1^3\sigma_2\dot{L}-4n\sigma_1\left(\sigma_2+\sigma_2^3\right)\dot{L}-4\dot{L}\dot{\sigma}_2+8L\sigma_1\dot{\sigma}_1\dot{\sigma}_2+2\sigma_1^2\left(2n^2L\sigma_2-2\dot{L}\dot{\sigma}_2\right) - \sigma_2\left(4\sigma_2\dot{L}\dot{\sigma}_2+4L\left(2n^2\left(1-\sigma_2^2\right)+2n\dot{\sigma}_1+\dot{\sigma}_1^2-\dot{\sigma}_2^2\right)\right)\Big]$$

and

$$[G_\sigma] = \begin{bmatrix} \frac{1-\sigma^2}{1+\sigma^2} & \frac{2\sigma_1}{1+\sigma^2} & \frac{2\sigma_2}{1+\sigma^2} \\ -\frac{\sigma_1}{L} & \frac{1-\sigma_1^2+\sigma_2^2}{2L} & -\frac{\sigma_1\sigma_2}{L} \\ -\frac{\sigma_2}{L} & -\frac{\sigma_1\sigma_2}{L} & \frac{1+\sigma_1^2-\sigma_2^2}{2L} \end{bmatrix}$$

$$^{\mathcal{H}}\boldsymbol{u} = \begin{bmatrix} u_x \\ u_y \\ u_z \end{bmatrix}.$$

An examination of the $\boldsymbol{\sigma}$ set equations reveals singularities in two different positions. One occurs when $L = 0$, which corresponds to a collision between tug and deputy. As discussed previously, this is of little practical importance. The second singularity occurs when $x = -L$ (or $e_1 = -1$). This singularity must be given attention, as there are many possible trajectories which may encounter this configuration.

2.3.3 The σ Shadow Set

As with the unit-vector description, there are two sets of L and $\boldsymbol{\sigma}$ values that describe the same relative position. This phenomenon is similar to the existence of a shadow set in the Modified Rodrigues parameter attitude description.[97] Using the alternate unit-vector description ($-L$,-$\hat{\boldsymbol{e}}$), the alternate $\boldsymbol{\sigma}$ set may be found. This shadow set, denoted as $\boldsymbol{\sigma}_s$, is defined as

$$\boldsymbol{\sigma}_s = -\frac{\boldsymbol{\sigma}}{\sigma^2}. \tag{2.34}$$

Differentiating yields the shadow set velocity

$$\dot{\boldsymbol{\sigma}}_s = -\frac{\dot{\boldsymbol{\sigma}}}{\sigma^2} + 2\frac{\boldsymbol{\sigma}^T\dot{\boldsymbol{\sigma}}}{\sigma^4}\boldsymbol{\sigma}, \tag{2.35}$$

where $\sigma^4 = (\sigma_1^2 + \sigma_2^2)^2$. For any relative motion, a set of $-L$, $-\dot{L}$, $\boldsymbol{\sigma}_s$, and $\dot{\boldsymbol{\sigma}}_s$ describes the exact same relative position and velocity as L, $\dot{L}$, $\boldsymbol{\sigma}$ and $\dot{\boldsymbol{\sigma}}$. In fact, one may switch between the original and shadow set arbitrarily. Each set evolves according to the same differential equations.

This has important implications regarding the singularity at $x = -L$. If this singularity is approaching, a switch to the shadow set may be used to avoid it. When the original set is at the singularity, the shadow set is well defined at $\boldsymbol{\sigma} = \mathbf{0}$. By choosing an appropriate switching location, arbitrary relative motion may be described using the $\boldsymbol{\sigma}$ set without encountering any singularities. Here, a switching condition of $\sigma^2 = 1$ is used. That is, when the magnitude of $\boldsymbol{\sigma}$ becomes larger than 1 a switch to the shadow set is employed. Considering the relationship between the unit-vector description and $\boldsymbol{\sigma}$ set, switching at this location restricts e_1 to only positive values, i.e. $e_1 \geq 0$. If $|\boldsymbol{\sigma}| \leq 1$, as is guaranteed by this switching condition, then e_1 is restricted to positive values due to the relationship $e_1 = (1 - \sigma^2)/(1 + \sigma^2)$. Changing back and forth between original and shadow set is equivalent to switching between L, $\hat{\boldsymbol{e}}$ and $-L$, $-\hat{\boldsymbol{e}}$.

2.4 Relative Motion Control

In this section relative motion control is considered, using the $\boldsymbol{\sigma}$ set. The goal is tracking an arbitrary tug trajectory. Because the equations of motion are based on the CW equations, only

trajectories with small separation distances are considered. For the electrostatic tractor application, these separation distances are typically less than 100 meters, compared with orbit radii in excess of 42,000 km. Relative motion control with the unit-vector description does not behave as well as the control using the $\boldsymbol{\sigma}$-set, so these details are reserved for the appendix. The $\boldsymbol{\sigma}$-set relative motion control strategy is presented as the viable alternative to the singular spherical coordinates in Reference 44.

2.4.1 σ Set Control

The $\boldsymbol{\sigma}$ set is a minimal description. That is, three parameters are used to describe motion in a three-dimensional system. To develop a $\boldsymbol{\sigma}$-based control law the error parameter $\delta\boldsymbol{\zeta}$ is used, where

$$\delta\boldsymbol{\zeta} = \boldsymbol{\zeta} - \boldsymbol{\zeta}_r = \begin{bmatrix} L \\ \boldsymbol{\sigma} \end{bmatrix} - \begin{bmatrix} L_r \\ \boldsymbol{\sigma}_r \end{bmatrix}. \tag{2.36}$$

Consider the candidate Lyapunov function

$$V_3(\delta\boldsymbol{\zeta}, \delta\dot{\boldsymbol{\zeta}}) = \frac{1}{2}\delta\boldsymbol{\zeta}^T[K]\delta\boldsymbol{\zeta} + \frac{1}{2}\delta\dot{\boldsymbol{\zeta}}^T\delta\dot{\boldsymbol{\zeta}} \tag{2.37}$$

where $[K]$ is a positive definite gain matrix. The derivative of this Lyapunov function is

$$\dot{V}_3(\delta\boldsymbol{\zeta}, \delta\dot{\boldsymbol{\zeta}}) = \delta\dot{\boldsymbol{\zeta}}^T\left([K]\delta\boldsymbol{\zeta} + \ddot{\boldsymbol{\zeta}} - \ddot{\boldsymbol{\zeta}}_r\right).$$

Substituting in Eq. (2.31) yields

$$\dot{V}_3(\delta\boldsymbol{\zeta}, \delta\dot{\boldsymbol{\zeta}}) = \delta\dot{\boldsymbol{\zeta}}^T\left([K]\delta\boldsymbol{\zeta} + [h] + [G_\sigma]^{\mathcal{H}}\boldsymbol{u} - \ddot{\boldsymbol{\zeta}}_r\right).$$

To ensure Lyapunov stability, the control law

$${}^{\mathcal{H}}\boldsymbol{u} = [G_\sigma]^{-1}\left(-[K]\delta\boldsymbol{\zeta} - [P]\delta\dot{\boldsymbol{\zeta}} - [h] + \ddot{\boldsymbol{\zeta}}_r\right)$$

is chosen, where $[P]$ is a positive definite gain matrix. This reduces the Lyapunov rate to

$$\dot{V}_3(\delta\boldsymbol{\zeta}, \delta\dot{\boldsymbol{\zeta}}) = -\delta\dot{\boldsymbol{\zeta}}^T[P]\delta\dot{\boldsymbol{\zeta}},$$

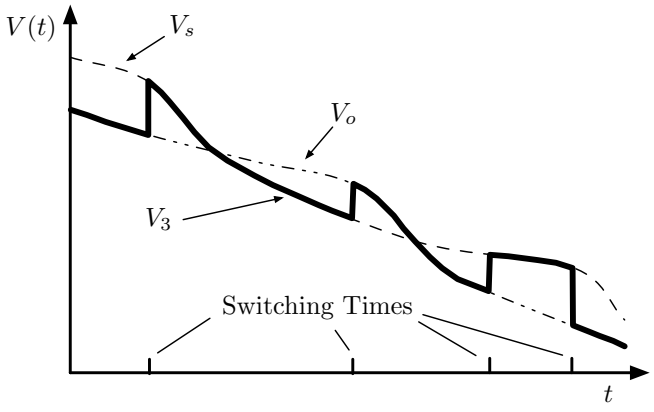

Figure 2.5: The Lyapunov function V_3 switches between two continuously decreasing functions as $\boldsymbol{\sigma}$ is switched to the shadow set.

which is negative semi-definite. To determine asymptotic stability, higher order derivatives of the Lyapunov function are taken and evaluated on the set $\delta\dot{\boldsymbol{\zeta}} = 0$.[77] The first non-zero derivative is

$$\dddot{V}_3(\delta\boldsymbol{\zeta}, \delta\dot{\boldsymbol{\zeta}}) = -2\delta\boldsymbol{\zeta}^T[K]^T[P][K]\delta\boldsymbol{\zeta},$$

which is negative definite in terms of $\delta\boldsymbol{\zeta}$. Thus, the control law tracks the reference trajectory asymptotically.

The act of switching between original and shadow set has important implications for the control response. The preceding Lyapunov stability analysis assumes that V_3 and its derivatives are continuous. Switching to the shadow set violates this continuity assumption. Furthermore, the signs of L and L_r may present problems. If $L < 0$ and $L_r > 0$, for instance, the control law will strive to move the deputy through $L = 0$ to positive values where it will track L_r. Not only is this a collisional hazard, but passing through $L = 0$ is a singularity for the $\boldsymbol{\sigma}$ set.

Each of these issues may be addressed by switching the reference trajectory to its shadow set, so that the signs of L and L_r are always the same. If the deputy position description is switched from original to shadow set, then the reference trajectory must be switched as well. Consider two Lyapunov functions V_o and V_s formed using the original and shadow $\boldsymbol{\sigma}$-set. With the control law in Eq. (2.4.1) formulated as a function of the original $\boldsymbol{\sigma}$-set, the Lyapunov stability analysis guarantees that the system will converge towards the reference. Because the original and shadow

$\boldsymbol{\sigma}$-sets describe the exact same relative positions, a convergence in one implies a convergence in the other. Thus, as V_o is decreasing, V_s must also be decreasing. When a switch is called for, the value of V_3 changes from V_o to V_s. In fact, at each switching time the value of V_3 changes back and forth between these two continuously decreasing functions, as illustrated in Figure 2.5. Thus, the system is still guaranteed to converge asymptotically in spite of the discontinuous switching.

There is a potential issue with switching the reference trajectory to its shadow set. It is possible that the reference trajectory may be switched onto a singularity. Consider the following example. If the reference location is at $x = -50$ m in the Hill frame, the only defined $\boldsymbol{\sigma}$ set description for this position is $L = -50$ m, $\boldsymbol{\sigma} = \mathbf{0}$. If the deputy motion calls for the reference trajectory to switch to its shadow set, it will shift onto the singularity.

The control acceleration contains contributions from the electrostatic force and tug thrusters, and is expressed as

$$^{\mathcal{H}}\boldsymbol{u} = {}^{\mathcal{H}}\boldsymbol{F}_e \left(\frac{1}{m_T} + \frac{1}{m_D} \right) + \frac{^{\mathcal{H}}\boldsymbol{T}_t}{m_T}, \tag{2.38}$$

where $^{\mathcal{H}}\boldsymbol{F}_e$ is the electrostatic force acting on the tug in Hill-frame components, $^{\mathcal{H}}\boldsymbol{T}_t$ is the tug thrust force in Hill-frame components, m_T is the tug mass, and m_D is the deputy mass. The electron beam is used to affect the tug and deputy charging, which will generate the electrostatic force $^{\mathcal{H}}\boldsymbol{F}_e$. The thrusting must compensate for this electrostatic force to generate the required control acceleration $^{\mathcal{H}}\boldsymbol{u}$. The commanded thrust, then, is computed as

$$^{\mathcal{H}}\boldsymbol{T}_t = m_T \left[{}^{\mathcal{H}}\boldsymbol{u} - {}^{\mathcal{H}}\boldsymbol{F}_e \left(\frac{1}{m_T} + \frac{1}{m_D} \right) \right]. \tag{2.39}$$

In order to estimate the electrostatic force for the feedforward compensation of $^{\mathcal{H}}\boldsymbol{F}_e$, some estimate of the charging on tug and deputy is required. Practically this can be challenging, as uncertainties in space weather conditions, craft geometries, and charging properties will result in differences between estimated values and the truth.

The need to continuously offset the electrostatic force with thrusting raises the question of fuel consumption. Throughout the duration of a reorbiting maneuver lasting several months,

continuous thrusting is required. The mass flow rate of fuel needed for thrusting is given by[41]

$$\dot{m}_F = \frac{T_t}{I_{\text{sp}} g_e} \tag{2.40}$$

where I_{sp} is the specific impulse of the thrusters and g_e is the acceleration due to gravity at the earth's surface (9.81 m/s^2). For cold gas thrusters, specific impulses are on the order of 50-100 seconds.[63] Using $I_{\text{sp}} = 100$ seconds and assuming a thrust magnitude of $T_t = 2$ mN is required to compensate for the electrostatic force, the fuel mass flow rate is 2.04×10^{-6} kg/s. Over a four month reorbiting time period, this results in a total fuel consumption of 21 kg. Cold gas thrusters are somewhat inefficient compared to low-thrust electric propulsion systems, which have I_{sp} values in excess of 1000 seconds. The challenge with using electric propulsion methods is they emit charged particles (ions) to generate thrust. These ions could be recaptured by the deputy object, inhibiting charging. If more efficient propulsion systems than cold gas thrusters are used, the fuel consumption would be reduced.

2.4.2 Uncertainties in Craft Charging

The craft charges will likely be an uncertain factor in an implementation of the control law. Obtaining a very accurate estimate of the charges will be difficult, and it is possible that the exact values may be unobtainable without touching the uncooperative object. The control system formulation assumes that the charges on the craft are known exactly. Naturally, it is of interest to determine the effects on the control system response when the craft charges are modeled imperfectly. This is an important consideration because in actual implementation, the charges will not be known precisely. When the charges are not modeled correctly, the closed loop response of the control system for the separation distance L is

$$\ddot{L} + P_L \dot{L} + K_L (L - L_r) = \frac{k_T}{L^2} (Q_{12} - Q_{12e}) \left(\frac{1}{m_T} + \frac{1}{m_d} \right), \tag{2.41}$$

where k_T is Coulombs constant, Q_{12} is the actual charge product ($q_1 q_2$) of the two craft, and Q_{12e} is the estimated charge product implemented in the controller. It is desired to obtain information

about where the equilibrium separation distance is with improperly modeled charges. To do so, the equilibrium conditions $\ddot{L} = \dot{L} = 0$ are applied. For compactness of notation, introduce

$$\mu = k_T \left(\frac{1}{m_T} + \frac{1}{m_d} \right) \tag{2.42a}$$

$$\Delta Q = (Q_{12} - Q_{12e}). \tag{2.42b}$$

The closed loop equilibrium positions are found by solving

$$K_L(L - L_r) = \frac{\mu}{L^2} \Delta Q.$$

With minor rearranging, a third order polynomial is obtained,

$$K_L L^3 - K_L L_r L^2 - \mu \Delta Q = 0 \tag{2.43}$$

The roots of this polynomial yield the equilibrium separation distance of the tug relative to the deputy. Note that only positive L values are realizable, based on the way the coordinate frame is defined. For simplicity of analysis, we consider only positive L values and ignore the shadow set that contains $-L$. Thus, we are concerned only with the existence of positive roots of the polynomial. The existence of such roots can be determined using Descartes rule of signs. Note that the same analysis may be applied to the $-L$ shadow set, yielding the same final results.

The sign of ΔQ plays an important role in determining the existence of positive roots. First, consider the case when the control system over-predicts the craft charge magnitudes. That is, the actual magnitudes of the craft charges are smaller than implemented in the control system. Because Q_{12} is negative, ΔQ will be positive. In the polynomial, only one sign change will occur between the L^3 and L^2 terms. As a result, it is certain that there will be one positive root, meaning the control system will drive the system to a positive L value. The magnitude of this equilibrium L is dependent on the feedback gain, the charges, and the craft masses.

Different behavior is obtained when the charge magnitudes are under-predicted. When the controller assumes smaller charge magnitudes than the craft actually experience, ΔQ is negative. Now, the polynomial will have two sign changes. This means that there will be either zero or two

real positive roots. The possibility of no equilibria is intriguing, as it implies the control system may fail to prevent a collision between the tug and deputy. To determine at which point the transition between zero and two positive roots occurs, the condition where Eq. (2.43) and its derivative both equal zero simultaneously is considered. The derivative of (2.43) taken with respect to L is

$$3K_L L^2 - 2K_L L_r L = 0, \tag{2.44}$$

which has a root at

$$L = \frac{2}{3} L_r. \tag{2.45}$$

Plugging this value back into the original polynomial yields the necessary gain that will ensure the existence of positive real roots. In order to ensure that an equilibrium exists in the closed loop system response, it is required that

$$K_L \geq \frac{27\mu|\Delta Q|}{4L_r^3}. \tag{2.46}$$

Interestingly, the requirement on the gain is dependent on the reference separation distance, L_r, and the error in the estimate of the craft charges. The required gain actually decreases with the cube of the reference distance. As a result, much higher gains are needed to ensure an equilibrium exists when the craft are desired to fly close than when they are desired to fly far apart. In order to properly bound K_L, some knowledge is needed regarding what errors may be expected in the estimation of the craft charges.

To illustrate the importance of proper gain selection, equilibrium locations are determined for an example case as a function of uncertainty in the craft charges. For this study, the true charge product is assumed to be $Q_{12} = -2.5 \times 10^{-11}$ C. The reference separation distance is set at $L_r = 15$ m, and the masses are $m_d = 500$ kg and $m_T = 2000$ kg. Assuming a feedback gain of $K_L = 5 \times 10^{-7}$, a range of Q_{12e} values are considered to simulate over- and under-prediction of the true charge magnitudes. The resulting equilibrium locations are shown in Figure 2.6. The plot is divided into two main regions. The first is $\Delta Q > 0$, which corresponds to the controller over-predicting the craft charges. As expected, only one equilibrium exists in this region. As the over-prediction becomes more severe, the location of the equilibrium configuration moves further

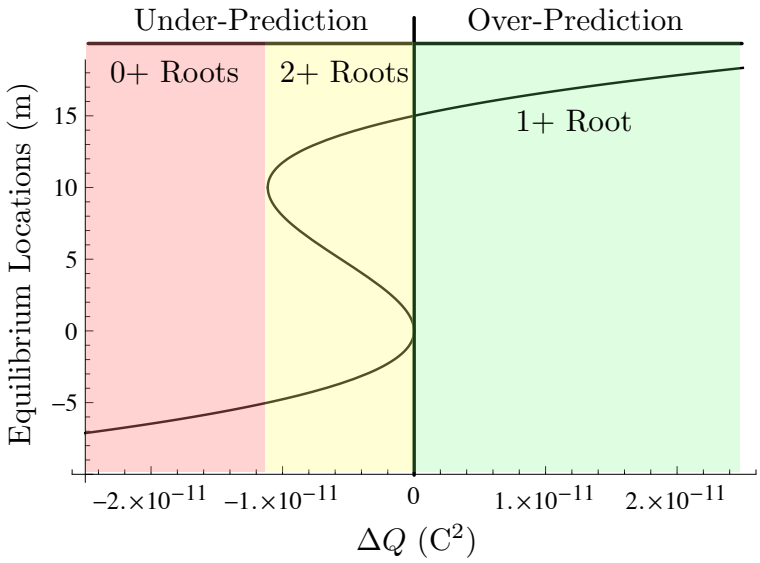

Figure 2.6: Effects of incorrect charge estimate on equilibrium locations.

and further away from the desired nominal position of $L = 15$ m. Note that when $\Delta Q = 0$, the equilibrium falls exactly at 15 m. This corresponds to perfect prediction of the craft charges by the controller. When $\Delta Q < 0$, the controller is under-predicting the actual craft charge magnitudes. The region of under-prediction is subdivided into two different cases: one with two positive roots, and one with zero positive roots. As ΔQ moves away from zero in the negative direction, the larger equilibrium location decreases from 15 meters, and a new equilibrium appears at $L = 0$ m. This new equilibrium grows from zero as the underprediction becomes more severe, until it coincides with the larger equilibrium and vanishes. Numerical simulations indicate that the larger equilibrium value is stable, while the lower one is unstable. When ΔQ is lower than this value, no positive equilibria exist. This is a dangerous region to be in, as the craft may impact if nothing is done to prevent a collision.

The example shown here is not intended to represent a specific operational scenario. Rather, the parameters used to generate the plot were chosen in order to demonstrate all of the possible behavior that may occur when the charges are improperly modeled. Practically, the gain should be increased to a reasonably high level so as to avoid the region with zero positive roots. As K_L

Table 2.1: Orbit elements for tug and deputy craft

	a (km)	e	i (°)	Ω (°)	ω (°)	M_0 (°)
Deputy	7500	0	20	10	250	0
Tug	a_d+0.05	$e_d + 0.00001$	$i_d - 0.001$	Ω_d	$\omega_d + 0.0001$	$M_{0,d}$

increases, the width of the yellow region in Figure 2.6 will increase as well. Likewise, this region will shrink when K_L is decreased. It is advantageous to make this region as large as possible, as it provides a wider allowable margin of error in predicting the craft charges.

The preceding results are obtained assuming the craft charges are fixed with time. This assumption is made in order to provide analytical insight into the issue of improperly modeled charges. In the actual system model, the charges change as the distance between the bodies evolves. Unfortunately, including this behavior in the analytical developments precludes the existence of useable insight. Qualitatively, however, the behavior is the same. The preceding developments provide a starting point for proper gain selection and potential outcomes that may occur with improperly modeled charges.

2.5 Numerical Simulation

To validate and illustrate the performance of the $\boldsymbol{\sigma}$-set control law, numerical simulation is used. The controller is implemented into an inertial simulation, where the trajectory of each craft is determined from integration of

$$\ddot{\boldsymbol{r}}_i = -\frac{\mu}{r^3}\boldsymbol{r}_i + \boldsymbol{u}, \tag{2.47}$$

where $\boldsymbol{u}$ is determined from the control law developed above. The relative motion is then computed using the inertial trajectories of each craft. The initial conditions for each simulation are determined by defining a set of orbital elements for the chief, and orbit element differences for the deputy. Because the $\boldsymbol{\sigma}$-set equations of motion are obtained from the linearized CW equations, the orbital element differences are kept at small levels such that the linear approximation is valid. The initial conditions of tug and deputy are shown in Table 2.1. For this validation, no charging is modeled and there is no electrostatic force. Once the charging model is introduced in Section 4.1.1, a full

simulation incorporating charged relative motion is performed.

A major advantage of the $\boldsymbol{\sigma}$-set description is that it isolates the separation distance from the relative orientation. Using proper gain selection, a desired separation distance may be achieved quickly and maintained during reorientation. For example, if the tug is to be repositioned from ahead to behind the deputy, a safe separation distance may be maintained while the tug moves around the deputy. To illustrate this point, gains are chosen that cause the deputy to track the reference separation distance (L_r) more quickly than the relative orientation ($\boldsymbol{\sigma}$). The $\boldsymbol{\sigma}$-set control law developed above effectively linearizes the closed-loop dynamics into the form

$$\delta\ddot{\boldsymbol{\zeta}} + [P]\delta\dot{\boldsymbol{\zeta}} + [K]\boldsymbol{\zeta} = 0.$$

By choosing diagonal $[K]$ and $[P]$ gain matrices, the response of the system for L-tracking is independent of $\boldsymbol{\sigma}$-tracking. Here, a slightly underdamped response is desired with a damping ratio of $\zeta = 0.925$. For this system the desired gains for a given settling time, T_s, are computed as[44,86]

$$K_i = \frac{27.829}{T_s^2}$$

$$P_i = 1.85\sqrt{K_i}.$$

The settling time for L is chosen as 30 minutes, while the settling time for $\boldsymbol{\sigma}$ is chosen as 1 hour.

To illustrate tracking performance, a time varying trajectory is specified in Hill-frame coordinates. The trajectory used is

$$x_r(t) = 0.05\cos(nt) \text{ (km)} \tag{2.48a}$$

$$y_r(t) = 0.05\sin(nt) \text{ (km)} \tag{2.48b}$$

$$z_r(t) = 0.02\sin(2nt + \pi/2)(\text{km}). \tag{2.48c}$$

During the simulation the switching conditions of $|\boldsymbol{\sigma}| = 1$ is employed, and the reference trajectory is switched to its shadow set during every tug switch so that $\text{sign}(L) = \text{sign}(L_r)$. The time histories of L and $\boldsymbol{\sigma}$ during the maneuver are shown in Figure 2.7. The state errors over the same time period are shown in Figure 2.8. The switching times are evident, both for the actual and reference

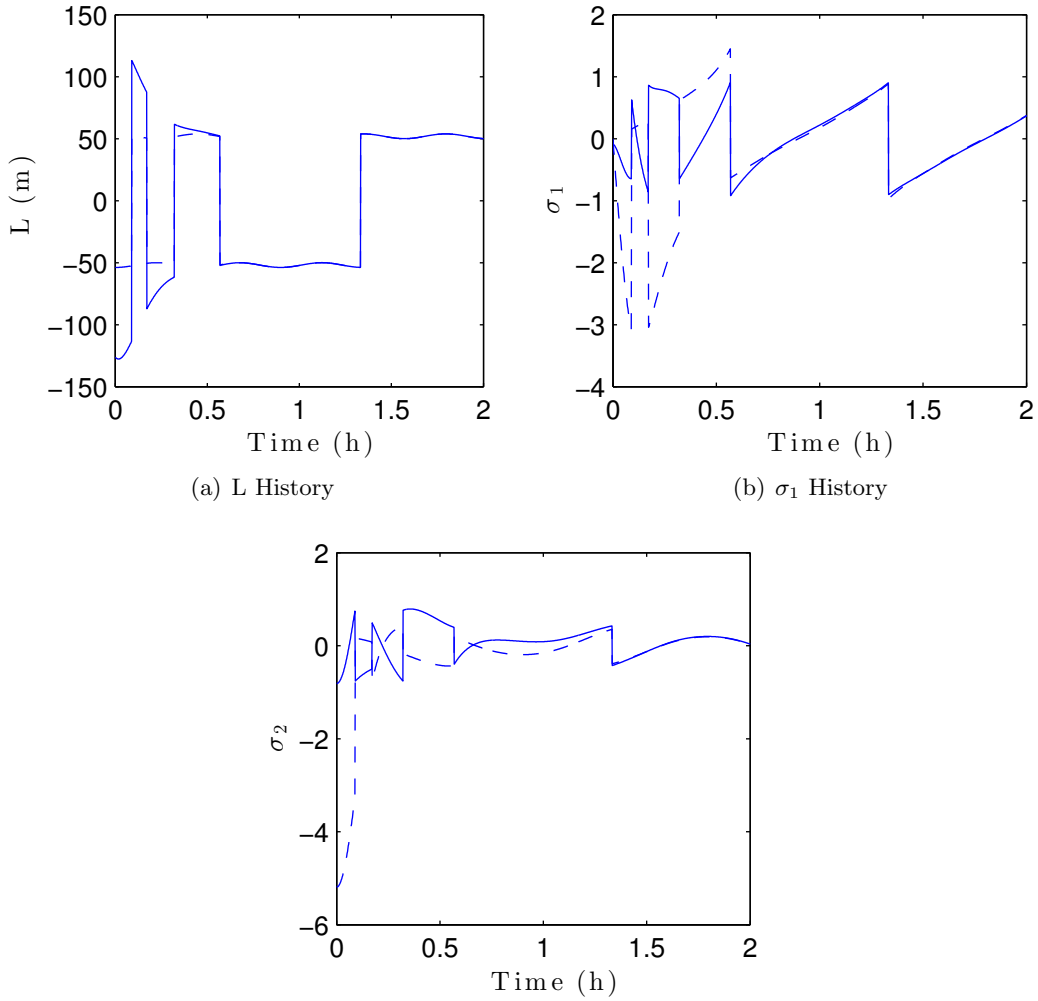

(a) L History

(b) σ_1 History

(c) σ_2 History

Figure 2.7: Time histories of L and $\boldsymbol{\sigma}$ during tracking maneuver. The reference trajectory is shown as a dashed line.

trajectories. While the magnitude of $\boldsymbol{\sigma}$ is constrained to be less than 1, the magnitude of $\boldsymbol{\sigma}_r$ is not. The reason is due to the fact that $\boldsymbol{\sigma}_r$ is automatically switched to its shadow set when $|\boldsymbol{\sigma}|$ calls for it, regardless of whether or not $|\boldsymbol{\sigma}_r| \leq 1$.

The effects of gain selection on the system response are clear in Figure 2.8. The separation distance has a rate of convergence to the reference that is twice as fast as the rate of convergence for $\boldsymbol{\sigma}$. The practical application for such a response is maintaining a safe separation distance during a reorientation maneuver. The control history for the $\boldsymbol{\sigma}$ set control law is shown in Fig 2.9. Again,

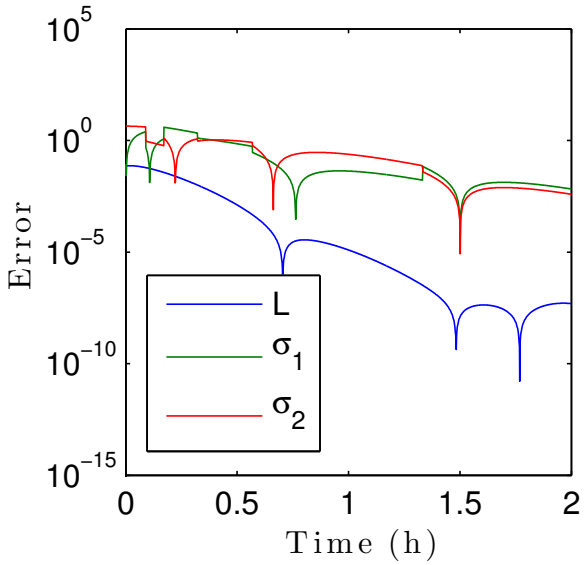

Figure 2.8: State errors for $\boldsymbol{\sigma}$ set control law throughout tracking maneuver.

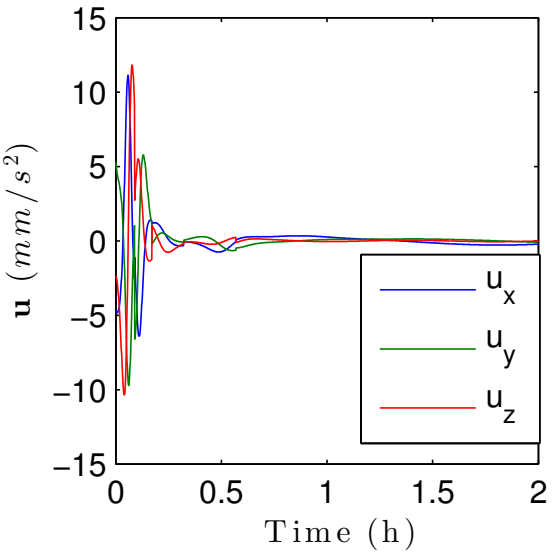

Figure 2.9: Control inputs for $\boldsymbol{\sigma}$ set control law.

mm/s^2 level control inputs are needed and a non-zero control is required to track the reference trajectory.

Chapter 3

Reorbiting Performance Analysis

Now, the electrostatic tractor performance for a variety of reorbiting maneuvers is considered. Radius of perigee, eccentricity, inclination, and right ascension of the ascending node corrections are investigated, along with GEO slot changes (longitude corrections). These more general orbit corrections are applicable to scenarios beyond just debris mitigation, such as station keeping or reorbiting a general Coulomb formation. For this analysis, tug and deputy potentials are assumed. The full charging dynamics are not incorporated at this point. Rather, reorbiting performance is determined for different potential levels. The problem of achieving these potential levels using charge transfer is reserved for the next chapter.

3.1 Deputy Mass-to-Radius Relationship

The charge expressions in Eq. (2.3) require the radius of the deputy object. Considering that arbitrary deputy objects may be targeted for removal, a range of craft sizes must be considered to evaluate the performance of the electrostatic tug for general reorbiting maneuvers. In Reference 96, publicly available data on geostationary satellites is used to obtain a relationship that relates mass (m_d) to an effective radius of the nearest spherical shape approximation. Because the objects considered are not truly spheres, the radii obtained are only approximations which allow for analytic charge predictions. The data considered result in the mean mass to radius relationship[96]

$$r_d(m_d) = 1.152 \text{ m} + 0.00066350 \frac{\text{m}}{\text{kg}} m_d. \tag{3.1}$$

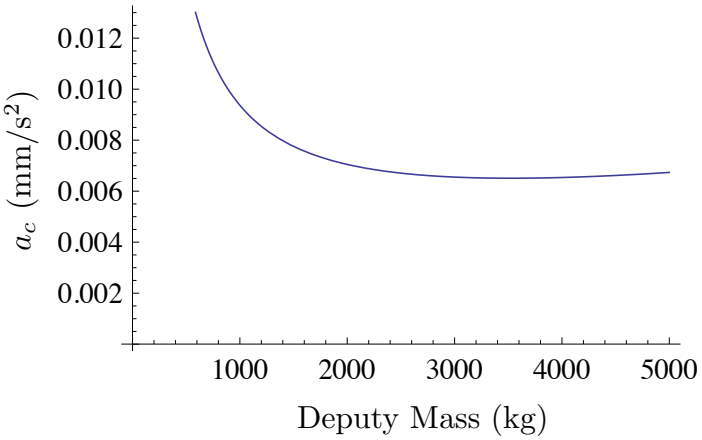

Figure 3.1: Acceleration due to electrostatic force for different deputy object masses. The tug of radius 3 m is charged to 30 kV, and the deputy to -30 kV.

Intuitively, it seems as though a more massive deputy object would be more challenging to move. That is, for a given set of tug and deputy potentials, it would take longer to move a larger deputy object than a smaller one. However, this is only true up to a point; beyond a critical deputy size, the trend reverses and it becomes easier to move an object. As an example, consider a tug with a potential of 30 kV and a deputy object charged to -30 kV. The tug is assumed to have a radius of 3 m, and the separation distance, L, is 10 m. The transfer time required to perform a deputy object reorbiting is dependent on the acceleration due to the electrostatic force, defined as

$$a_c = \frac{F_c}{m_d} \tag{3.2}$$

The resulting acceleration for a wide range of deputy masses is shown in Figure 3.1. Beyond a critical value of 3524 kg, the acceleration in this scenario begins to increase again. This means that a deputy object of 4000 kg could actually be reorbited more quickly than one with a mass of 3500 kg under the conditions specified above. This trend is due to the increased capacitance present for larger objects. The capacitance increases linearly with tug vehicle radius, which increases linearly with mass according to Eq. (3.1). While the higher masses require more force to achieve the same acceleration levels as lower mass objects, their increased size results in a larger craft radius. This larger size results in higher charges on the craft for the same levels of potential.

3.2 Variational Equations

To study the reorbiting capabilities of the electrostatic tug concept, Gauss' variational equations are used. In prior work, semi-major axis changes are considered for debris objects located at geosynchronous altitudes with the tug leading the deputy in the along-track direction.[44,96,98] Here, the electrostatic tugging research is extended in two ways by 1) considering more general orbital element changes, as well as 2) considering the required relative tug/debris positions to achieve these maneuvers. The orbital position of the deputy object is assumed to be described by a set of osculating classical orbital elements: the semi-major axis (a), eccentricity (e), inclination (i), right ascension of the ascending node (Ω), argument of perigee (ω), and true anomaly (f).[97]

The acceleration of the deputy due to the electrostatic force (a_c) is decomposed into components in the rotating Hill frame of the deputy, also referred to as the local-vertical local-horizontal (LVLH) frame: a_r, a_θ, and a_h. The a_r component is aligned with the orbit radius vector, the a_h component is aligned normal to the orbit plane, and the a_θ component acts orthogonal to a_r and a_h, in the along-track direction.

Gauss' variational equations provide the rates of change for the set of osculating orbit elements as[97]

$$\frac{\mathrm{d}a}{\mathrm{d}t} = \frac{2a^2}{h}\left(e\sin f a_r + \frac{p}{r}a_\theta\right) \tag{3.3a}$$

$$\frac{\mathrm{d}e}{\mathrm{d}t} = \frac{1}{h}\left(p\sin f a_r + ((p+r)\cos f + re)a_\theta\right) \tag{3.3b}$$

$$\frac{\mathrm{d}i}{\mathrm{d}t} = \frac{r\cos(\omega+f)}{h}a_h \tag{3.3c}$$

$$\frac{\mathrm{d}\Omega}{\mathrm{d}t} = \frac{r\sin(\omega+f)}{h\sin i}a_h \tag{3.3d}$$

$$\frac{\mathrm{d}\omega}{\mathrm{d}t} = \frac{1}{he}(-p\cos f a_r + (p+r)\sin f a_\theta) - \frac{r\sin(\omega+f)\cos i}{h\sin i}a_h \tag{3.3e}$$

$$\frac{\mathrm{d}f}{\mathrm{d}t} = \frac{h}{r^2} + \frac{1}{he}(p\cos f a_r - (p+r)\sin f a_\theta), \tag{3.3f}$$

where r is the orbit radius, $p = a(1-e^2)$ is the semi-lactus rectum, and $h = r^2\dot{f}$ is the orbit specific angular momentum magnitude. Generally, these equations must be numerically integrated to determine how the osculating elements evolve with time. For the case of the electrostatic tractor,

however, a few assumptions are made that allow for analytic predictions of orbit element changes. First, the electrostatic force magnitudes are small ($\sim$ mN or less) and do not create large changes in the orbital elements over one orbital period. Second, during the tugging maneuver the relative position of the tug and deputy is held piecewise constant, meaning that the direction of a_c is also piecewise constant. Lastly, the assumption is made that the magnitude of the electrostatic force, and the corresponding acceleration, is constant throughout the maneuver.

With these assumptions, it is possible to predict how the orbital elements of the deputy object will evolve over one orbit without requiring numerical integration of the variational equations. By extending this prediction to multiple orbits, a reasonable approximation may be obtained for the performance of the electrostatic tug for general reorbiting maneuvers. To arrive at the analytic predictions, the procedure detailed in Reference 16 is used. The independent variable in the variational equations is changed from time to eccentric anomaly. The modified equations may then be integrated analytically over one orbital period. First, the rate of change for the orbit eccentric anomaly is introduced,[16]

$$\frac{\mathrm{d}E}{\mathrm{d}t} = \sqrt{\frac{\mu}{a}}\frac{1}{r} + \frac{1}{e\sin E}\left(\frac{\mathrm{d}e}{\mathrm{d}t}\cos E - \frac{r}{a^2}\frac{\mathrm{d}a}{\mathrm{d}t}\right), \tag{3.4}$$

where μ is the gravitational parameter of earth. Based on the assumption of small perturbing forces and negligible changes in the orbit elements over one orbital period, Eq. (3.4) may be approximated as

$$\frac{\mathrm{d}E}{\mathrm{d}t} \approx \sqrt{\frac{\mu}{a}}\frac{1}{r}. \tag{3.5}$$

Using this approximation for the eccentric anomaly rate, the independent variable in Gauss' variational equations is changed from time to eccentric anomaly. The resulting modified rate equations

are[16]

$$\frac{\mathrm{d}a}{\mathrm{d}E} = \frac{2a^{5/2}}{\mu\sqrt{p}}\left(ae\sqrt{(1-e^2)}\sin E a_r + pa_\theta\right) \tag{3.6a}$$

$$\frac{\mathrm{d}e}{\mathrm{d}E} = \frac{\sqrt{ap}}{\mu}\left(a\sqrt{(1-e^2)}\sin E a_r + a(2\cos E - e - e\cos^2 E)a_\theta\right) \tag{3.6b}$$

$$\frac{\mathrm{d}i}{\mathrm{d}E} = \frac{a^{5/2}}{\mu\sqrt{p}}\left(\cos\omega(\cos E - e) - \sqrt{1-e^2}\sin\omega\sin E\right)(1 - e\cos E)a_h \tag{3.6c}$$

$$\frac{\mathrm{d}\Omega}{\mathrm{d}E} = \frac{a^{5/2}}{\mu\sqrt{p}}\left(\sin\omega(\cos E - e) + \sqrt{1-e^2}\cos\omega\sin E\right)(1 - e\cos E)a_h. \tag{3.6d}$$

Note that the argument of perigee and true anomaly equations have been omitted, as they will not be used here.

Using the assumptions outlined previously, the only term in Eq. (3.6) that changes significantly over one orbital period is the eccentric anomaly, E. An analytic expression for the orbit element changes over one orbital period is obtained by integrating Eq. (3.6) on the interval $E = [0, 2\pi]$. In this study, five different scenarios are considered. The first is a change in radius of perigee, with a focus on debris reorbiting applications. International guidelines call for debris in the GEO belt to be raised to a higher disposal orbit.[1,2] Over time, solar radiation pressure will introduce eccentricity into the disposal orbit of a debris object. If this eccentricity is large enough, the radius of perigee of the orbit may dip back into the GEO belt. Here, we consider how much effort is required to raise the radius of perigee back to a safe altitude. Beyond the radius of perigee corrections, changes in eccentricity, inclination, right ascension of the ascending node, and GEO slot are considered. Such orbital element corrections are more suitable for a non-debris related scenario where a change in the deputy orbit is called for. Here the tug is performing an orbit change service for the deputy, without requiring the deputy to use it's own fuel.

3.3 Orbit Modification Predictions

In this section, analytic predictions are made for the various orbit modifications considered in this study. The electrostatic force expression in Eq. (2.4) is computed for a range of vehicle sizes and potential levels. Different separation distances are also considered. Sweeping these parameters

allows for the computation of performance predictions for a wide range of cases. For each of the orbit element corrections, maneuvers are designed such that changes occur only to the orbital parameter considered out of the four (r_p, e, i, Ω). For example, when considering inclination changes, the tug craft is placed such that only inclination is changed over one orbit. Designing the maneuvers in this way requires a repositioning of the tug craft during the orbit in certain cases. This issue will be discussed shortly.

3.3.1 Radius of Perigee Corrections

The radius of perigee corrections are motivated by a debris mitigation scenario in the GEO regime. As discussed above, a situation is conceivable where a once-circular disposal orbit has dipped back into the GEO belt due to an injection of eccentricity. Rather than recircularizing and increasing the orbit radius, a simpler solution would be to increase the radius of perigee. This would only raise the lowest debris orbit point to be outside the GEO zone, without wasting fuel raising the already acceptable apogee location. The radius of perigee is defined as

$$r_p = a(1-e). \tag{3.7}$$

Taking the derivative of this expression with respect to the eccentric anomaly yields

$$\frac{\mathrm{d}r_p}{\mathrm{d}E} = \frac{\mathrm{d}a}{\mathrm{d}E}(1-e) - a\frac{\mathrm{d}e}{\mathrm{d}E}. \tag{3.8}$$

Using the relationships in Eq. (3.6), the rate of change of the radius of perigee with respect to the eccentric anomaly is found to be

$$\frac{\mathrm{d}r_p}{\mathrm{d}E} = \frac{2a^3}{\mu}\left(-(e-1)^2\cos\left(\frac{E}{2}\right)\sin\left(\frac{E}{2}\right)a_r + \sqrt{1-e^2}(2-e-e\cos E)\sin^2\left(\frac{E}{2}\right)a_\theta\right) \tag{3.9}$$

To assess performance of the electrostatic tug for raising the radius of perigee, Eq. (3.9) is integrated from $E = [0, 2\pi]$ to determine the change in r_p over one orbit. The result of this integration is

$$\Delta r_p = \frac{\pi a^3}{\mu}(4-e)\sqrt{1-e^2}a_\theta. \tag{3.10}$$

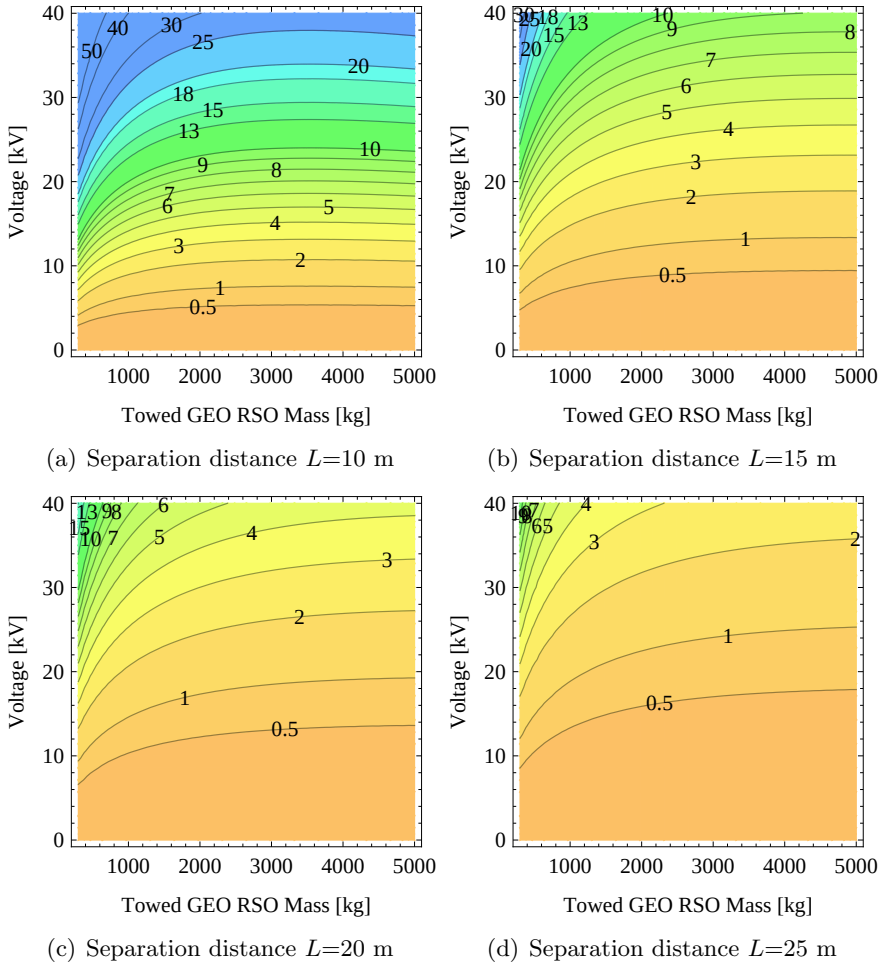

(a) Separation distance L=10 m

(b) Separation distance L=15 m

(c) Separation distance L=20 m

(d) Separation distance L=25 m

Figure 3.2: Kilometer radius of perigee increase per day for a range of debris masses, voltages, and separation distances with $e = 0.00359$. These results assume a mass-to-area relationship for debris objects and a tow vehicle radius of 3 m.

This equation illustrates that higher eccentricity values will hinder the performance of the radius of perigee raising maneuver. If the tug is held at a constant position throughout an orbit, as is assumed here, only the electrostatic force component in the along track direction will affect the radius of perigee. To maximize the force in this direction, the best configuration is one where the tug is ahead of the debris object in the along track direction (the leader-follower alignment). If this configuration is adopted, then $a_\theta = a_c$.

Performance of the radius of perigee raising maneuver is considered for four separation distances: L=10, 15, 20, 25 m. For each separation distance, deputy masses ranging from 300 to

5000 kg are included. The voltage on the tug and debris is assumed to be of equal magnitude, but opposite polarity. The debris object is assumed to have been initially reorbited to a disposal orbit 300 km above GEO, but due to the injection of eccentricity had dropped its radius of perigee back into the GEO belt. This results in an eccentricity of 0.00359 and a semi-major axis of 42,391 km for the debris orbit. The amount of increase in the radius of perigee per orbit for these various conditions is shown in Figure 3.2. Here, the nomenclature of resident space object (RSO) is used, where RSO may refer to a towed debris or cooperative deputy object.

In general, closer separation distances and higher voltage levels lead to larger increases in r_p over one orbital period. These trends are due to the increased magnitude of electrostatic forces that result from higher potentials and smaller L values. Furthermore, note that the contour lines do not continuously increase as the RSO mass grows larger. This is indicative of the higher capacitance available on larger objects, which have higher surface areas. This increased capacitance results in larger charge magnitudes for the same potential, in turn increasing the magnitude of the electrostatic force between tug and debris. The results here indicate that if separation distances on the order of 10-15 meters are maintained, along with potential levels between 20 and 30 kV, the radius of perigee of the debris object may be increased by 300 km over a period of a few months.

3.3.2 Eccentricity Corrections

Let us now turn our attention to eccentricity changes, which may be part of general orbit corrections for a deputy object. Here, a modification of eccentricity is desired where the other orbit elements remain unchanged after one orbital period. This can be accomplished by switching the sign of a_θ, which is assumed to equal a_c, when $E = \pm\pi/2$.[16] This corresponds to moving the tug from ahead to behind the deputy object and back during each orbit. During this repositioning time, it is assumed that the tug will discharge, meaning no electrostatic force is present. If the tug can be repositioned quickly enough, the impact on the overall eccentricity change will be minimal. This is illustrated numerically in the next section. If this procedure is carried out, assuming minimal effects due to the repositioning maneuver, the eccentricity change over one orbital period

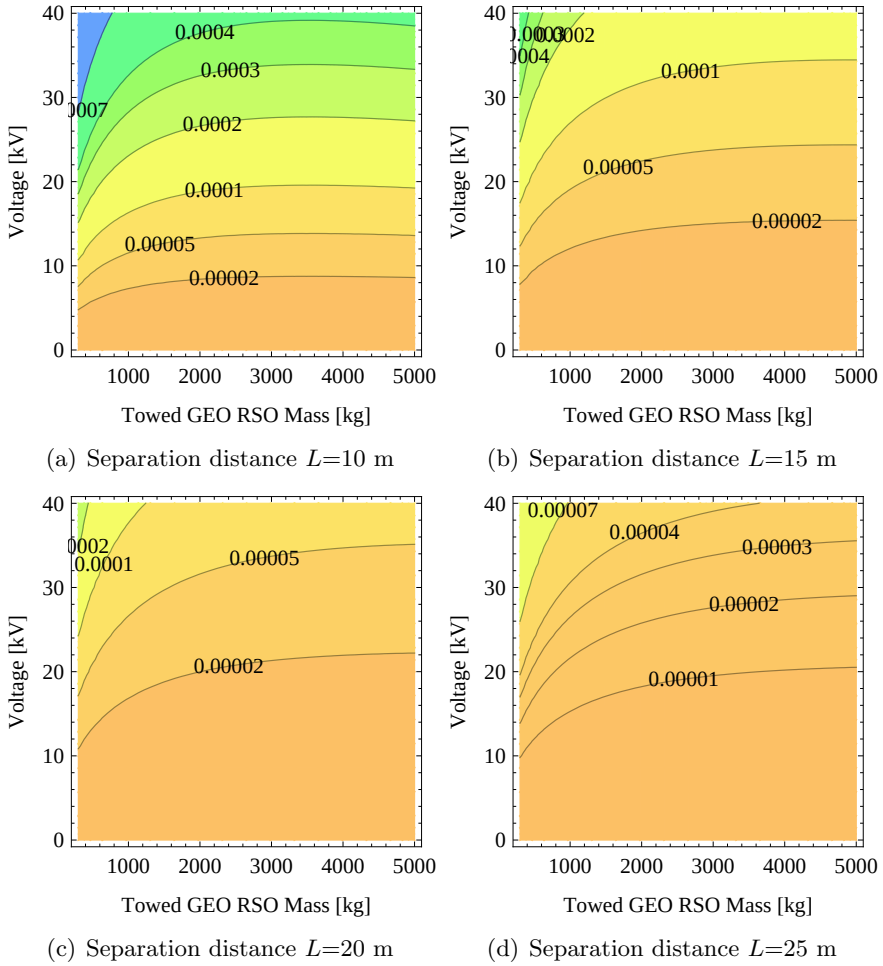

(a) Separation distance L=10 m

(b) Separation distance L=15 m

(c) Separation distance L=20 m

(d) Separation distance L=25 m

Figure 3.3: Eccentricity change per day for a range of RSO masses, voltages, and separation distances assuming initially $e = 0.00359$. These results assume a mass-to-area relationship for debris objects and a tow vehicle radius of 3 m.

is approximately[16]

$$\Delta e = \frac{8a^2}{\mu}\sqrt{1-e^2}a_c. \tag{3.11}$$

Again, a debris object at GEO altitudes with a slight eccentricity is considered. Here, the semi-major axis of the debris orbit is assumed to be 42,391 km with an eccentricity of 0.00359. Performance for various separation distances, RSO masses, and potential levels are considered, again using the mass to radius ratio in Eq. (3.1). The results are shown in Figure 3.3. Similar trends as before are noted, where performance is improved by closer separation distances and higher potential levels. Considering the predictions shown here, the orbit of the modeled deputy object

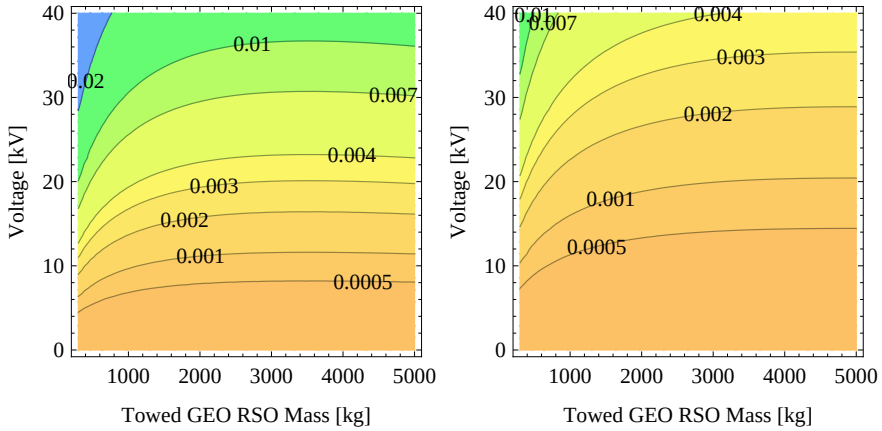

(a) Separation distance L=10 m (b) Separation distance L=15 m

Figure 3.4: Inclination change per day (in degrees) for a range of RSO masses, voltages, and separation distances assuming $e \approx 0$. These results assume a mass-to-area relationship for deputy objects and a tow vehicle radius of 3 m.

could be recircularized over a period of 1-3 months, depending on the separation distance, potential, and mass. Note that this corresponds to a change in position of a few hundred kilometers, which is a similar performance result as the radius of perigee corrections over a similar time frame.

3.3.3 Inclination Corrections

For the inclination corrections, a maneuver is sought in which only the inclination is changed after one orbital period. This may be accomplished by repositioning the tug during the orbit at $\omega + f = \pm\pi/2$.[16] For pure inclination changes, the tug needs to be moved from above to below (or vice-versa) the deputy orbital plane at these locations in the orbit. Again, it is assumed that this repositioning will occur quickly enough that minimal impact occurs on the inclination change performance, so that an instantaneous repositioning is a valid assumption. Maintaining the tradition of assuming small deputy object eccentricity, the approximate change over one orbital period using this repositioning maneuver is[16]

$$\Delta i = \frac{4a^2}{\mu} a_c. \tag{3.12}$$

Eccentricity does not appear in this expression because of the near-circular orbit assumption.

To assess performance of tug for inclination changes, two separation distances are considered: L=10, 15 m. The same ranges of voltages and masses are considered as before, and the deputy is assumed to be in an orbit with a semi-major axis of 42,241 km. The results are shown in Figure 3.4. In general, modifications to the inclination of no more than a few thousandths of a degree are possible over one orbit. Even over a time period of a few months, it is not possible to achieve inclination changes of 1 degree. The low performance of the electrostatic tug for inclination changes can be attributed to the large ΔV typically required to perform such corrections. The electrostatic forces acting on the deputy are very small (on the order of mN) and are not available at a magnitude significant enough to greatly affect the inclination. The relatively small corrections possible at the separation distances considered here is the reason why L=20 and 25 m were omitted. As the separation distance is decreased, the electrostatic force between tug and deputy becomes smaller and the performance is further reduced.

3.3.4 Right Ascension of the Ascending Node Corrections

For modifications to the right ascension of the ascending node (RAAN), a maneuver is considered which results in only RAAN changes after one orbit. This may be accomplished by reversing the direction of the electrostatic force at each equatorial crossing ($\omega + f$=0).[16] Again, this requires a repositioning of the tug twice per orbit. It is assumed that this repositioning occurs quickly enough so that it will have negligible impact on the amount of RAAN change. Integrating the rate of change of RAAN in Eq. (3.6) across one orbit, assuming both a small eccentricity and the aforementioned changes in electrostatic force direction yields a change per orbit of[16]

$$\Delta\Omega = \frac{4a^2}{\mu \sin i} a_c. \tag{3.13}$$

Here, the inclination of the deputy orbit has a direct impact on the performance of the tug. Smaller inclinations will result in larger changes in Ω for the same a_c.

The performance of the tug for RAAN changes is computed assuming an inclination of both 1 and 5 degrees. Two separation distances are considered for each inclination, L=10 and 15 m, and

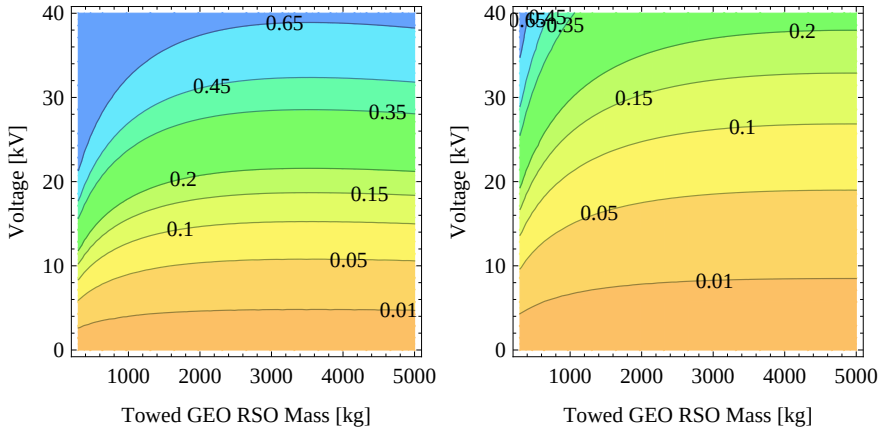

(a) Separation distance L=10 m, $i = 1°$ (b) Separation distance L=15 m, $i = 1°$

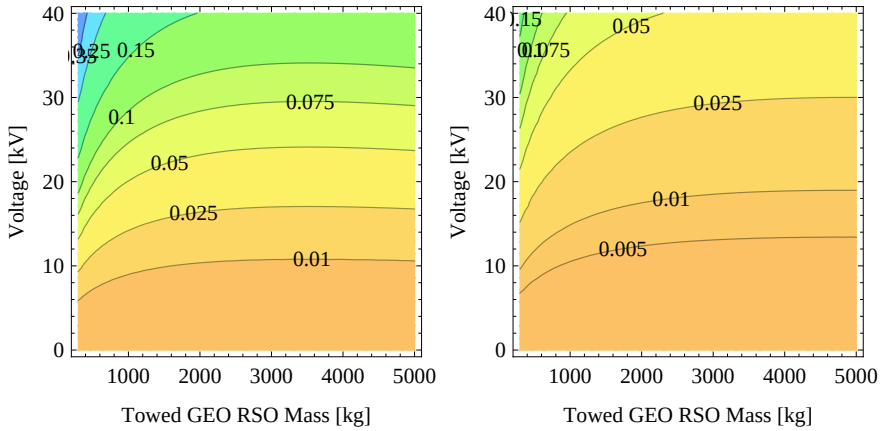

(c) Separation distance L=10 m, $i = 5°$ (d) Separation distance L=15 m, $i = 5°$

Figure 3.5: RAAN change per day (in degrees) for a range of RSO masses, voltages, and separation distances assuming $e \approx 0$. These results assume a mass-to-area relationship for deputy objects and a tow vehicle radius of 3 m.

the semi-major axis of the orbit is assumed to be a=42,241 km. The changes in RAAN for a range of RSO masses and craft voltages are shown in Figure 3.5. As expected, the performance is better for the lower inclination. The trend is again observed where larger deputy masses actually become easier to move beyond some critical mass value, due to the increased capacitance of the larger objects. The potential RAAN changes over a period of a few months are on the order of several degrees for the cases considered here. This is much more significant than the possible inclination changes. However, the deputy object inclination is assumed to be relatively small here. Larger inclinations would significantly hinder the potential of the electrostatic tug to perform RAAN

corrections.

3.3.5 Slot Change Performance

The problem of repositioning a deputy object from one slot in GEO to another is now considered. Here, a transfer from one longitude to another at GEO is of interest. The maneuver to perform such a transfer can be broken down into two phases, a tug and coast period. In the first, the tug is employed to change the semi-major axis of the object. With a different semi-major axis, the object will drift at a different anomaly rate which allows for a longitude change to occur while coasting. The tug is then reemployed to return the semi-major axis back to its original value. The maneuver is assumed to contain some fraction of tugging and coasting periods. It is possible to tug the entire time, first pulling the object away from a GEO orbit and then pulling it back. The longer the tugging is performed, the larger the semi-major axis change will be. This, in turn, results in a faster drift rate, which will ultimately change the longitude more quickly.

For the following analysis, it is assumed that the maneuver is divided symmetrically. That is, if a slot change of 30 degrees is desired, some combination of tugging and coasting may be employed to reach the 15 degree mark. The same procedure is then used in reverse to take the object the final 15 degrees. This assumption allows the maneuver time to be computed for half of the desired slot change, and then doubled to estimate the total required time.

For the slot change maneuver, the first phase consists of a tugging in the positive or negative along-track direction to change the semi-major axis of the object's orbit. The amount of longitude change that occurs during this period is denoted as $\delta\theta_1$. It is assumed that the time spent during the tugging phase is t_1. In Reference 98, the amount of drift that occurs during the tugging phase is determined as

$$\delta\theta_1 = -\frac{3}{2}\frac{a_\theta}{a}t_1^2. \tag{3.14}$$

Once a semi-major axis change has occurred, there will be a difference in mean motion that allows a further change in the longitude simply by coasting, denoted as $\delta\theta_2$. Assuming a coasting time of

t_2, the drift due to the coasting period is

$$\delta\theta_2 = \Delta n t_2, \tag{3.15}$$

where Δn is the change in mean motion of the object due to the semi-major axis change. Recall the expression for mean motion

$$n = \sqrt{\frac{\mu}{a^3}}. \tag{3.16}$$

Because small changes in a relative to the size of the orbit are considered here Δn is approximated by taking the first variation of n,

$$\Delta n \approx -\frac{3}{2}\frac{\delta a}{a} n_{\text{GEO}}, \tag{3.17}$$

where δa is the change in a that occurs during the tugging period and n_{GEO} is the mean motion of the GEO orbit. The semi-major axis change, δa, is due solely to the tugging period and is approximately[98]

$$\delta a = \frac{2a_\theta}{n_{\text{GEO}}} t_1. \tag{3.18}$$

Substituting Eq. (3.18) into (3.17) and combining with Eq. (3.15) yields the change in longitude during the coast period

$$\delta\theta_2 = -3\frac{a_\theta}{a} t_1 t_2. \tag{3.19}$$

The total maneuver time is expressed as

$$t_t = 2(t_1 + t_2). \tag{3.20}$$

The factor of two is due to the symmetry of the maneuver. If a 40 degree slot change is desired, for example, then $\delta\theta_1 + \delta\theta_2 = 20°$. The expressions for $\delta\theta_1$ and $\delta\theta_2$ may be rearranged to solve for t_1 and t_2. Using these values, the total time required for a slot change is

$$t_t = 2\left(\sqrt{\frac{-2a}{3a_\theta}}\delta\theta_1 + \sqrt{\frac{-a\delta\theta_1}{6a_\theta}}\frac{\delta\theta_2}{\delta\theta_1}\right). \tag{3.21}$$

The signs of a_θ and $\delta\theta_1$ must be opposite to obtain a real result. This is due to how a_θ affects the semi-major axis change. When $a_\theta > 0$, an increase in a occurs and the mean motion of the

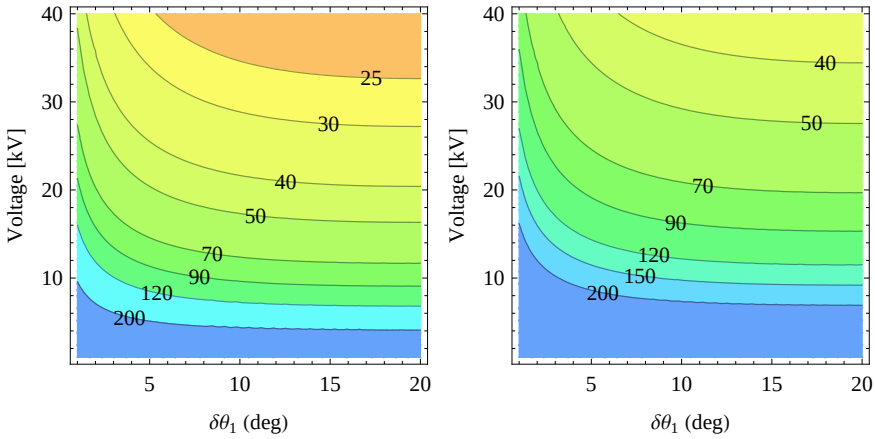

(a) Separation distance L=10 m (b) Separation distance L=15 m

Figure 3.6: Time required in days for a slot change of 40°. Deputy object is assumed to have a mass of 2000 kg.

object will be reduced. This will cause a drift in the negative θ direction. The opposite occurs when $a_\theta < 0$.

For a total desired longitude change of $\delta\theta$, any combination of $\delta\theta_1$ and $\delta\theta_2$ may be used so long as $\delta\theta_1 + \delta\theta_2 = \delta\theta/2$, $\text{sign}(\delta\theta_1) = \text{sign}(\delta\theta)$, and $|\delta\theta_1| > 0$. To illustrate times required to perform a slot change using the electrostatic tug, a repositioning of $\delta\theta = 40°$ is considered. Here, the deputy object is assumed to have a mass of 2000 kg and an orbit with $a = 42,241$ km. The time, in days, required to perform the slot change maneuver for a variety of conditions is shown in Figure 3.6. The angle change during the tug period is varied from 1 degree to 20 degrees. At the upper limit, no coasting period exists; the tug tows the object to decrease, then increase, the semi-major axis. This is the fastest manner in which to achieve the slot change because the semi-major axis change is greatest. The performance is improved for higher voltages and lower separation distances due to the increased electrostatic forces that result. Higher forces yield larger a_θ values. Inspection of Eq. (3.21) reveals that larger a_θ values will tend to decrease the total time required. For the scenario described here, no more than a few months are required to achieve the desired slot change.

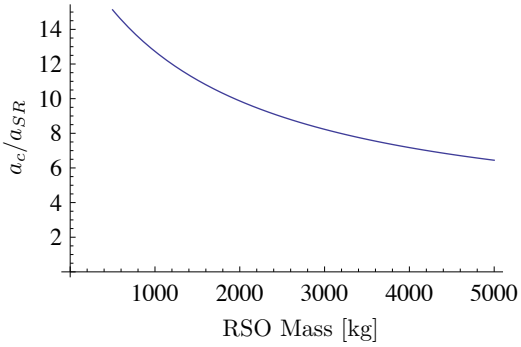

Figure 3.7: Ratio of a_c to a_{SR} for a variety of towed-object masses. These results assume $V_t = 25$ kV and $V_d = -25$ kV with a tug radius of 3 m.

3.3.6 Solar radiation pressure and third-body effects

The electrostatic tug is now considered for use in station-keeping maneuvers. For an otherwise functional satellite (the deputy) that has lost its ability to perform maneuvers, the electrostatic tug may be used to extend mission lifetime by repositioning the satellite as needed. As such, it is pertinent to examine the more significant perturbations acting on a satellite at GEO, and determine how large their influence is relative to the capabilities of the electrostatic tug. Here, the influences of solar radiation pressure and third-body effects are considered.

The acceleration due to solar radiation is computed and compared with that due to the electrostatic force. The model used for this acceleration is[112]

$$a_{SR} = -\frac{p_{SR} c_R A}{m_d}, \tag{3.22}$$

where p_{SR} is the solar pressure (4.51×10^{-6} N/m^2), A is the area of the satellite exposed to the sun, and c_R is the reflectivity of the satellite surface. Here, we are not concerned with precisely modeling the effects of solar radiation pressure, but rather with obtaining appropriate order-of-magnitude estimates. As such, the assumption of spherical deputy shapes is maintained, and the reflectivity is set at $c_R = 1$. To illustrate how large the solar radiation effects are, a scenario is considered where the tug is charged to 25 kV and the deputy to -25 kV. The tug is assumed to have a radius of 3 m, and the nominal separation distance is set to $L = 15$ m. The ratio of the acceleration due to the electrostatic force, a_c, to the acceleration due to solar radiation pressure,

a_{SR}, is computed for a variety of towed-object masses. The results are shown in Figure 3.7. Note that for all masses considered the electrostatic acceleration is several times that due to solar radiation pressure. Because the tug direction is arbitrary, any direction of solar radiation pressure may be corrected for. In terms of station keeping, any undesired motion due to solar radiation effects may be overcome by the electrostatic tug.

To consider the effects of third-body perturbations, approximate orbital element rates are computed which result from the influence of lunar gravity. These variational equations are obtained from Reference 26, and are derived assuming the third body is fixed in space. Because order-of-magnitude estimates for these effects are desired, this is a sufficient approximation. The variational equations of interest here are

$$\frac{\mathrm{d}r_p}{\mathrm{d}t} = -a\frac{\mathrm{d}e}{\mathrm{d}t} \tag{3.23a}$$

$$\frac{\mathrm{d}e}{\mathrm{d}t} = -\frac{15\mu_3 e\sqrt{1-e^2}}{4r_3^3 n}\left(2AB\cos(2\omega) - (A^2-B^2)\sin(2\omega)\right) \tag{3.23b}$$

$$\frac{\mathrm{d}i}{\mathrm{d}t} = \frac{3\mu_3 C}{4r_3^3 n\sqrt{1-e^2}}\left(A[2+3e^2+5e^2\cos(2\omega)] + 5Be^2\sin(2\omega)\right) \tag{3.23c}$$

$$\frac{\mathrm{d}\Omega}{\mathrm{d}t} = \frac{3\mu_3 C}{4r_3^3 n\sqrt{1-e^2}\sin(i)}\left(5Ae^2\sin(2\omega) + B[2+3e^2-5e^2\cos(2\omega)]\right), \tag{3.23d}$$

where r_3 is the distance from satellite to third body and μ_3 is the gravitational parameter for the third body. The parameters A, B, and C are functions of the relative orientation of the satellite and third body. Rather than examining a particular scenario, the orders of magnitude of the above variational equations are considered. The rates $\mathrm{d}i/\mathrm{d}t$ and $\mathrm{d}\Omega/\mathrm{d}t$ are on the order $\mu_3/(r_3^3 n)$. The eccentricity rate, $\mathrm{d}e/\mathrm{d}t$, is on the order of $\mu_3 e/(r_3^3 n)$, and the rate $\mathrm{d}r_p/\mathrm{d}t$ is of order $a\mu_3 e/(r_3^3 n)$. Assuming an average distance from a satellite in GEO to the moon of 384,400 km, this works out to rates on the order of $\mathrm{d}i/\mathrm{d}t \approx \mathrm{d}\Omega/\mathrm{d}t \approx 10^{-9}$ 1/s^2 . For the radius of perigee corrections, the eccentricity levels considered here ($\sim$0.001) result in a rate on the order of $\mathrm{d}r_p/\mathrm{d}t \approx 10^{-7}$ km/s. For eccentricity, the rate is on the order of $\mathrm{d}e/\mathrm{d}t \approx 10^{-12}$ 1/s^2.

To compare the lunar perturbations with the electrostatic tug capabilities, the changes over one orbital period computed previously are averaged over one day. For any of the orbital elements,

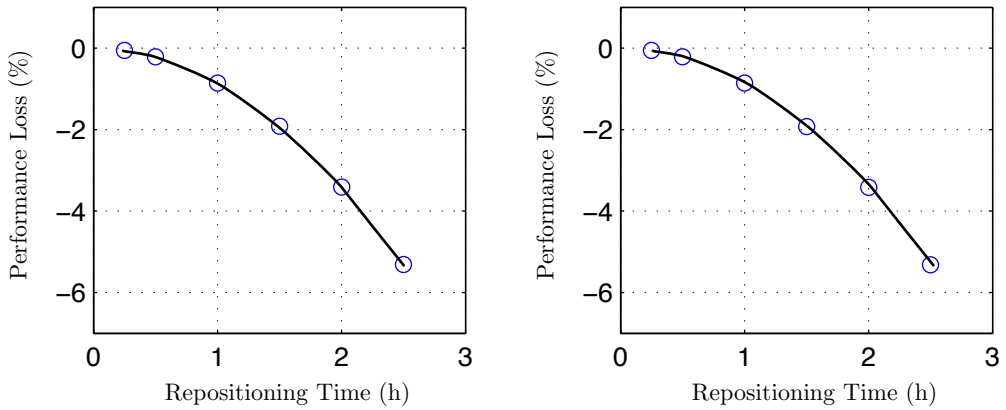

(a) Eccentricity (b) RAAN

Figure 3.8: Percent loss in performance over one orbital period for various repositioning times.

the rate is approximated as $d\text{œ}/dt = \Delta\text{œ}/P$, where P is the orbital period. For each of these orbital elements except inclination, the electrostatic tug is able to modify their values at a faster rate than the third body perturbations. This implies that use of the electrostatic tug will not be inhibited by the third body, except in the case of inclination. However, the performance results for inclination are at sufficiently low levels to suggest that the tug is not an ideal method for large-scale inclination corrections.

3.4 Tug Repositioning Considerations

In the evaluation of orbit element modification performance, tug repositioning maneuvers are assumed for changes in e, i, and Ω. During the repositioning phase of the orbit, the tug is discharged so that no electrostatic force is in place between tug and deputy object. The primary reason for doing this is to prevent accelerations from acting on the deputy object in unwanted directions as the tug maneuvers around it. These unintended accelerations would lead to changes in orbital elements that are not desired.

3.4.1 Performance Losses

In the following analysis, a deputy object with a semi-major axis of 42,241 km and an eccentricity of 0.001 is considered. The inclination is set at 5°, the right ascension of the ascending node at 20°, and the argument of perigee at 90°. For these conditions, the orbital period will be approximately 24 hours. The deputy object is assumed to have a mass of 2000 kg and a potential of -25 kV. The tug is assumed to be at a potential of 25 kV with a radius of 3 m. The nominal separation distance is set at 15 m. To determine the impact of tug repositioning on performance, numerical simulation of the inertial equations of motion is used. Here, only the motion of the deputy is propagated with

$$\ddot{\boldsymbol{r}}_d = -\frac{\mu}{r_d^3}\boldsymbol{r} + \boldsymbol{a}_c, \tag{3.24}$$

where $\boldsymbol{a}_c$ is computed using Eq. (3.2). The direction of $\boldsymbol{a}_c$ is set depending on which orbital element is being corrected. To simulate the tug repositioning, $\boldsymbol{a}_c$ is set to zero for various time spans during an orbit where the repositioning occurs. The tug reorientation is divided equally on either side of the switching condition. For example, if an eccentricity change maneuver is considered then half of the tug repositioning occurs on one side of $E = \pi/2$, and the remainder on the other side. Effectively, the switching condition is encountered when the tug is halfway through repositioning.

The finite-time tug realignment maneuvers are compared with an instant realignment, as assumed in the performance predictions in the preceding section. The percent loss in performance for various repositioning times is computed for eccentricity and RAAN corrections. The results are shown in Figure 3.8. Note that the repositioning times shown here are for a single repositioning maneuver, which occurs twice per orbit. So, for a 2.5 hour maneuver time there are a total of 5 hours during the orbit during which no electrostatic force acts on the deputy. This is slightly more than 20% of the orbit. Even for such a large fraction of the orbital period, the performance losses are relatively minimal at slightly more than 5%. The reason for this is that the switching conditions occur at times in the orbit when the rates of change for their respective orbital elements are nearly zero. The penalty for removing the electrostatic force at these locations is minimal

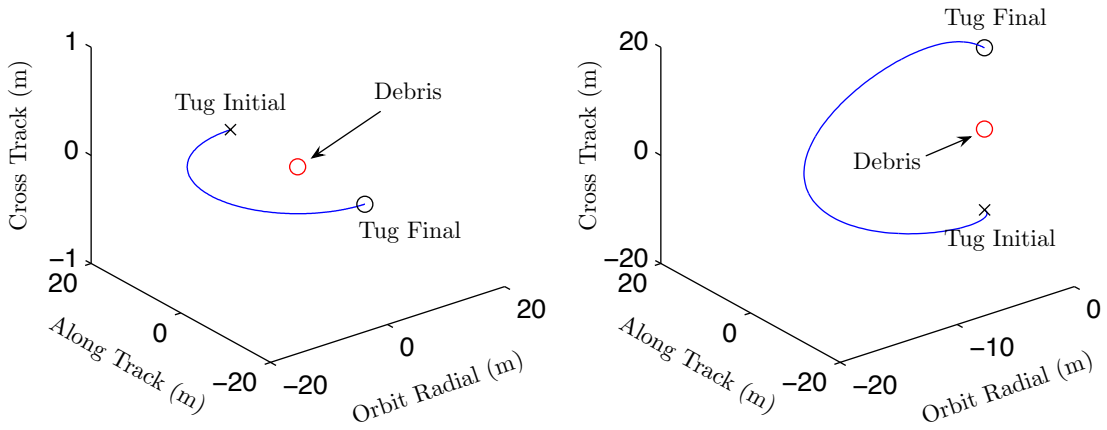

(a) e Changes

(b) Ω, i Changes

Figure 3.9: Relative motion trajectories during repositioning maneuvers

because there is already little change of the orbital element. As the repositioning time is increased, however, the penalties increase because regions of the orbit with higher rates of orbital element changes are encountered. The results of this analysis indicate that, practically, the repositioning will have minimal impact on the overall performance of the electrostatic tug.

3.4.2 Thrust Requirements

Now, attention is paid to the issue of thrust requirements for achieving a tug repositioning in the time scales considered here. The electrostatic tug concept is based around the use of low thrust engines on the tugging vehicle, on the order of mN.[44,98] It would be impractical if thrust levels on the order of Newtons or tens of Newtons were required during repositioning, because the propulsion system would not be designed for such conditions. From a fuel consumption standpoint, employing such high thrust levels twice per orbit over the dozens of orbits required for orbit element corrections would greatly reduce mission lifetime.

Determining thrust levels necessitates consideration of the relative motion between tug and deputy. A control system is needed to enforce the desired relative motion and compute the required thrust. For this purpose, the relative motion control system in Reference 44 is employed. The

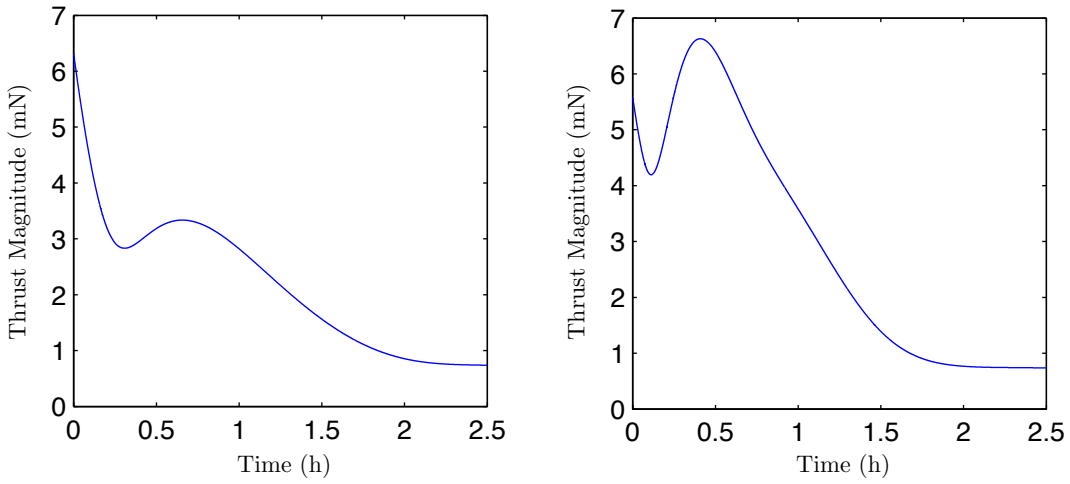

(a) e Changes

(b) Ω, i Changes

Figure 3.10: Thrust magnitudes required for repositioning maneuvers

control system is designed to affect a desired relative motion trajectory of the tug relative to the deputy for the electrostatic tug problem. For the simulations done here, thrust levels are computed assuming a repositioning time of 2.5 hours. Two scenarios are considered. The first is applicable to eccentricity changes, where the tug begins ahead of the deputy object in the along-track direction and must end up behind it. The second applies to inclination and RAAN changes, where the tug must pass from one side to the other of the deputy orbital plane. The goal here is to move the tug from an initial separation distance of 15 meters to a final separation distance of 15 meters in its new orientation, within a 2.5 hour timespan. During the simulation, the potential on the tug is set at 0 so that no electrostatic force is present. The motion of both tug and deputy is propagated using inertial 2-body equations of motion. The deputy follows natural orbital motion, in a circular orbit at 42,241 km. The tug motion is affected both by gravity and by inertial thrusters.

The relative motion trajectories for both repositioning maneuvers are shown in Figure 3.9. For the case of eccentricity changes, the tug is initialized 15 meters ahead of the deputy in the along-track direction. The control system uses the inertial thrusters to reposition the tug behind the deputy at 15 meters in a 2.5 hour timespan. While not considered here, the eccentricity correction maneuver does require the eventual return of the tug to its initial position ahead of

the deputy object. For inclination and RAAN changes, the tug is initialized 15 meters below the deputy object in the cross-track direction (below the deputy orbital plane). In a 2.5 hour span, the thrusters are used to reposition the tug 15 meters above the deputy orbital plane. In both cases, the separation distance is held at a constant 15 meters throughout the maneuver. This is a function of the control law developed in Reference 44, which uses spherical coordinates as the relative position measure. The repositioning maneuver is accomplished by controlling the spherical angles, all the while holding separation distance constant.

The thrust magnitudes required for both maneuvers are shown in Figure 3.10. For both cases considered here, no more than 6.5 mN is required to achieve a repositioning in 2.5 hours. These levels of thrust are comparable to those required to maintain a fixed separation distance with the electrostatic force in place.[44] During the actual orbit element correction phases, when a fixed relative position is held with the electrostatic force in place, the same thrust levels are needed. This has important implications on the thrust requirements. The same low-thrust engines used during the towing phases are sufficient to reposition the tug within a timeframe that does not significantly affect performance. Furthermore, no additional fuel is expended using these repositioning maneuvers than would otherwise be used by holding a tugging configuration the entire time. The orbit element modifications that require repositioning would not adversely affect mission lifetime as compared to the more simple case of semi-major axis corrections, where no repositioning is needed.

Chapter 4

Charge Transfer Analysis

4.1 Charging Model and Nominal Space Weather Conditions

In this study, a scenario is considered where a spacecraft (the tug) is equipped with an electron gun that is used for remote charging of a second satellite (the deputy). In general, the deputy may be a cooperative spacecraft or a non-functioning debris object. For the charge transfer analysis, however, we return to the baseline scenario of reorbiting a GEO debris object into a disposal orbit. Only a semi-major axis change is required and the tug and deputy maintain a constant leader-follower position throughout the duration of the maneuver.[44,95] First, the details of the charging model used to characterize the charge transfer process are presented, and then various aspects of charging behavior are investigated.

4.1.1 Spacecraft Charging Model

The electrostatic tugging force used for towing is dependent on the charging that occurs on both the tug and deputy. Several factors influence this charging process. Naturally occurring ion and electron plasma currents are collected by the spacecraft, and photoelectrons may be emitted depending on the spacecraft potential and presence of sunlight. Focused electron beam emission by the tug is used for charge control. When the electron beam is absorbed by the deputy, secondary electron emission occurs as the incoming beam electrons excite and release electrons from the deputy surface material. The potential levels achieved by the tug and deputy result from a balance of these various current sources, which are illustrated in Figure 4.1. To compute these potentials,

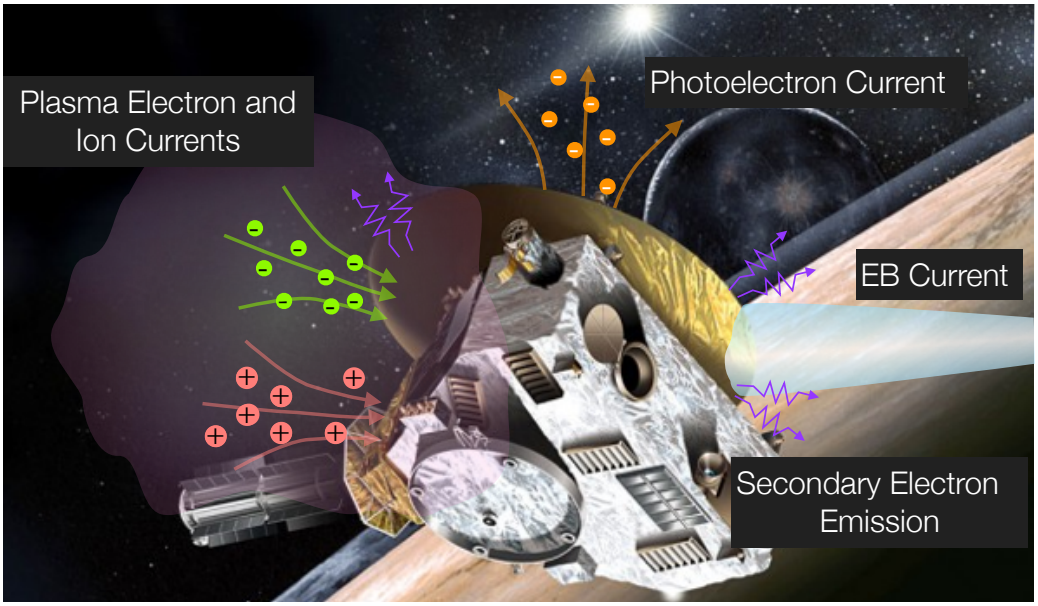

Figure 4.1: Illustration of various current sources that affect spacecraft charging.

the charging model developed in Reference 100 is applied.

A photoelectron current occurs whenever the spacecraft are in sunlight. This current is modeled by[67]

$$I_{ph}(\phi) = j_{ph,0} A_{\perp} e^{-\phi/T_{ph}} \qquad \phi > 0 \tag{4.1a}$$

$$= j_{ph,0} A_{\perp} \qquad \phi \leq 0 \tag{4.1b}$$

where ϕ is the spacecraft potential, $T_{ph} = 2$ eV is the temperature of the emitted photoelectrons, $j_{ph,0} = 20\ \mu\text{A/m}^2$ is the photoelectron flux,[100] and $A_{\perp}$ is the cross-sectional area exposed to sunlight. For the spherical geometries assumed here, $A_{\perp} = \pi r^2$. For potentials in excess of about +10 V, the photoelectron current is effectively zero because all of the emitted electrons are recaptured.

The plasma electron current is modeled by[92]

$$I_e(\phi) = -\frac{A q n_e w_e}{4} e^{\phi/T_e} \qquad \phi < 0 \tag{4.2a}$$

$$= -\frac{A q n_e w_e}{4} \left(1 + \frac{\phi}{T_e}\right) \qquad \phi \geq 0, \tag{4.2b}$$

where A is the effective surface area exposed to the plasma environment, T_e is the plasma electron temperature, n_e is the plasma electron density, q is the elementary charge, and $w_e = \sqrt{8T_e/\pi m_e}$

is the thermal velocity of the electrons. The electron mass is represented by m_e. Note that for large negative potentials, I_e is very small. This is due to the fact that electrons are repelled by the negatively charged spacecraft. Similarly, the plasma ion current is computed using[92]

$$I_i(\phi) = \frac{Aqn_i w_i}{4} e^{-\phi/T_i} \qquad \phi > 0 \tag{4.3a}$$

$$= \frac{Aqn_i w_i}{4}\left(1 - \frac{\phi}{T_i}\right) \qquad \phi \leq 0, \tag{4.3b}$$

where $w_i = \sqrt{8T_i/\pi m_i}$. Note that the variable quantities represent the same parameters as before, except the subscript i is used to denote they represent ions. In the space weather model for the GEO environment utilized here, the ion species consists solely of protons. For high positive potentials, the ion current is very small because the ions are repelled by the positively charged spacecraft.

Charge control is achieved using an electron emitted from the tug onto the deputy. A portion of the beam current will be absorbed by the debris, depending on tug pointing accuracy and the charge levels of both tug and debris. This current is modeled as

$$I_D(\phi_D) = -\alpha I_t \qquad q\phi_T - q\phi_D < E_{EB} \tag{4.4a}$$

$$= 0 \qquad q\phi_T - q\phi_D \geq E_{EB}, \tag{4.4b}$$

where I_t is the beam current emitted by the tug, E_{EB} is the electron beam energy, and the subscripts T and D represent the tug and deputy, respectively. The parameter α represents the efficiency of the charge transfer process; it is the fraction of the beam current emitted by the tug that reaches the deputy. In general, this is a function of beam pointing accuracy and the width of the beam at the deputy location. It can also be impacted by the tug and debris potentials, in addition to the beam energy. In the current paper a value of $\alpha = 1$ is used, which maintains the value established in Reference 100. This assumes a well focused and accurately pointed beam. Better quantification of the α parameter is beyond the scope of this paper, and is left for future work. Once $q\phi_T - q\phi_D = E_{EB}$, it is impossible for additional beam current to make it to the deputy. The emitted beam electrons do not have enough energy to cross the potential difference between tug and deputy.

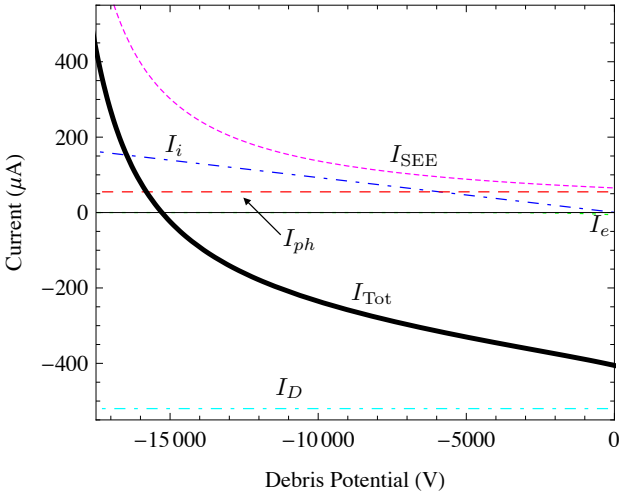

Figure 4.2: Currents acting on the deputy for a range of deputy potentials. Deputy achieves a potential that results in $I_{\rm Tot}$=0.

When the electron beam impacts the deputy object, the incoming electrons result in the emission of secondary electrons. Because of the large negative potential of the deputy object (kV level), these electrons will escape. This represents a significant current source that must be accounted for. Secondary electron emission is modeled by[33]

$$I_{\rm SEE}(\phi_D) = -4Y_M I_D(\phi_D)\kappa \qquad \phi_D < 0 \tag{4.5a}$$

$$= 0 \qquad \phi_D \geq 0, \tag{4.5b}$$

where

$$\kappa = \frac{E_{\rm eff}/E_{\rm max}}{(1 + E_{\rm eff}/E_{\rm max})^2}$$

and $E_{\rm eff} = E_{EB} - q\phi_T + q\phi_D$. Y_M is the maximum yield of secondary electron production, and E_{max} is the impact energy at which this maximum occurs. In this paper, $Y_M = 2$ and $E_{\rm max} = 300$ eV are used, maintaining the values established in Reference 100.

For the tug, the charging is dominated by the plasma electron current and electron beam emission. The tug settles to a potential that satisfies the current balance $I_e(\phi_T) + I_t = 0$. This is solved analytically as

$$\phi_T = \left(\frac{4I_t}{Aqn_e w_e} - 1\right) T_e, \tag{4.6}$$

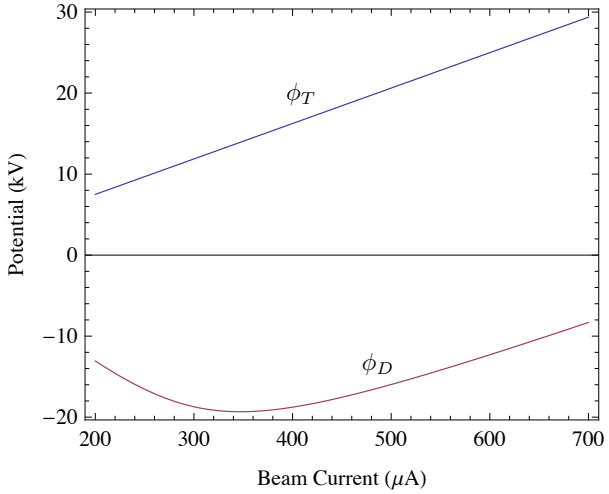

Figure 4.3: Tug and deputy potentials as a function of beam current.

which assumes a positive tug potential. This will be the case provided the beam current is sufficient. The current balance on the deputy object contains a few more contributions, and an analytical solution does not exist. The deputy will achieve a potential that satisfies

$$I_{\text{Tot}} = I_e(\phi_D) + I_i(\phi_D) + I_{\text{SEE}}(\phi_D) + I_{ph}(\phi_D) + I_D(\phi_D) = 0. \tag{4.7}$$

The presence of the photoelectron current implies the deputy is in the sunlight. When in the Earth's shadow, the current balance contains all of the same terms except for I_{ph}. A numerical root finder is used to solve for ϕ_D in Eq. (4.7).

An example charging scenario is presented in Figure 4.2. Shown are the various currents impacting deputy charging for space weather conditions of $n_e = 0.6$ cm^{-3}, $n_i = 9.5$ cm^{-3}, $T_i = 50$ eV, and $T_e = 1250$ eV, which are typical of GEO in quiet storm conditions.[32] The results assume a beam energy of E_{EB} =40 keV and a beam current of I_t=520 μA. The tug and deputy are treated as spheres, with radii of $r_T = 2$ m and $r_D = 0.935$ m. With these conditions, the tug achieves a potential of $\phi_T = 21.5$ kV and the deputy reaches a potential of $\phi_D = -15.3$ kV. As seen in Figure 4.2, the deputy potential results in a net zero current balance, i.e. $I_{\text{Tot}} = 0$. While the plasma electron current is included in the current balance, for the deputy it provides an insignificant contribution to charging at the high potential levels achieved. The tug and deputy potentials as a

function of beam current are shown in Figure 4.3. The tug potential increases linearly with beam current, while the deputy potential has its largest value around $I_t = 350$ μA.

There are two electron beam parameters that may be used to influence charging: the beam energy and potential. Generally, a higher beam energy will result in higher deputy charging. This is due to the reduced secondary electron emission that stems from the higher energy of the incoming beam electrons. As the energy of an absorbed electron increases, fewer secondary electrons are emitted. Because the secondary electrons essentially result in the loss of some fraction of the incoming beam current, reducing the number of secondary electrons emitted will improve deputy charging. Thus, the beam energy is treated as constant, while the beam current is considered to be a control variable. Depending on the space weather conditions, increasing or decreasing the beam current can improve or worsen deputy charging, as shown in Figure 4.3. However, the tug will always charge to higher potentials as the beam current is increased, up to the level of the beam energy ($q\phi_T \leq E_{EB}$). Choosing a beam current to maximize the resulting electrostatic force requires a careful balance between tug and deputy charging, as well as consideration of changes in space weather. Too much current will overcharge the tug relative to the deputy and result in a weaker force. Too little, and neither the tug nor deputy will charge sufficiently.

It is assumed that the potentials ϕ_T and ϕ_D that result from this charging model are absolute potentials,[105] and that the plasma electron and ion currents are functions of the background plasma densities. However, the plasma distribution in the presence of a highly charged object is perturbed. For example, in the vicinity of the positively charged tug, the electron density will be higher than background, and the ion density will be lower. Even though the deputy is located within this region, the background densities are used in the electron and ion current expressions. The validity of this assumption is not clear at this time, and future work is needed to investigate and possibly modify the charging model.

In the event that the tug cannot deliver electron beam current to the deputy, the charging model will yield a deputy potential that is a function of the plasma ion and electron currents and the photoelectron current. The charging is dominated in large part by the photoelectron current,

Table 4.1: Coefficients used to fit space weather data.

Parameter	a_5	a_4	a_3	a_2	a_1	a_0
n_e	9.447e-7	-5.601e-5	1.425e-3	0.0170	0.04804	0.9
n_i	4.144e-5	-2.270e-3	.03558	-.09276	-0.6345	5.0
T_e	1.112e-5	-6.948e-4	0.01599	-.1564	.4568	2.30

which is of higher magnitude than the plasma currents. Because of this, the charging model will result in a deputy potential of a few volts positive due to emission of photoelectrons. When the deputy reaches this slightly positive potential, photoelectrons are recaptured and the deputy reaches equilibrium potential.

The highly charged nearby tug, however, changes this dynamic somewhat. In isolation, the deputy begins recollecting photoelectrons at only a few volts positive. This is reflected in Eq. (4.1a) where the net photoelectron current decays to zero as the deputy is charged to higher potentials. Essentially, the reason why the deputy settles to a few volts positive is because this is the potential at which a large portion of the emitted photoelectrons are recaptured. With the tug nearby at a high positive potential, emitted photoelectrons will be collected by the tug because the electric field in the vicinity of the deputy will point away from it, even if the deputy is at a few volts positive. At low positive potentials, the photoelectrons will not be recaptured by the deputy. This loss of negative charge (outgoing electrons) will raise the deputy potential until the deputy begins recapturing enough photoelectrons to results in a net zero current. This phenomenon is not captured by the charging model here, and so the charging model cannot be applied to the case when charge transfer does not occur. When charge transfer occurs, driving the deputy to a negative potential, there is enough electron beam current to offset the loss of photoelectrons and this issue is not a problem. Modifying the charging model for applicability to the non-charge transfer scenario would be a good area for future work.

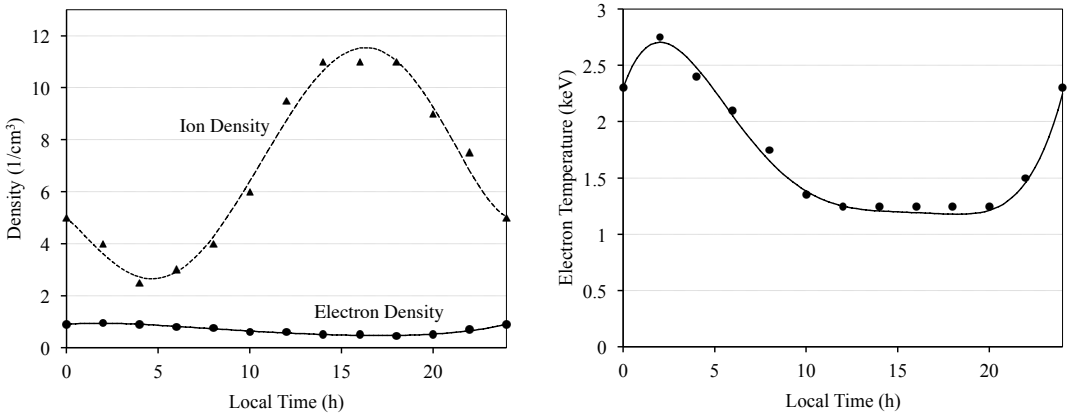

(a) Density (b) Temperature

Figure 4.4: GEO space weather parameters as a function of local time for $K_p = 1.5$. Markers represent data values taken from Reference 32 and lines show polynomial data fits.

4.1.2 Space Weather Environment at GEO

The charging results are dependent on the local space weather environment at GEO. The plasma density and temperature varies considerably, both with solar activity and local time. To provide a realistic model for the GEO environment, the ten year averaged measurements presented in Reference 32 are used. The data were collected over an eleven year period from 1990-2001 and cover roughly one complete solar cycle. In this study, we seek to characterize the impacts of changes in space weather that occur over a typical day during quiet geomagnetic storm activity. While extreme geomagnetic storms do create periods of highly perturbed space weather conditions, these do not make up a significant portion of the time required for an electrostatic tugging maneuver (see Figure 1.2). Thus, a model for the variations in space weather throughout a single GEO orbit is sought for a K_p index of 1.5. The K_p index is a measure of solar activity, and a value of 1.5 represents a condition of low solar activity.

In the GEO environment, there are two populations of ions: hot and cold. The hot ions generally have temperatures in the 10 keV range, with densities on the order of 1 cm^{-3}. The cold ions, which have their origins in the ionosphere, have temperatures between 3 and 100 eV and densities that range from less than 1 to over 10 cm^{-3}. These cold ions are most prevalent in the

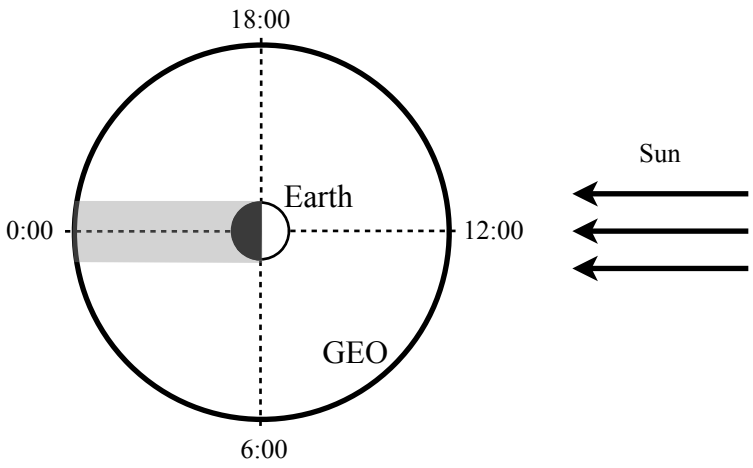

Figure 4.5: Illustration of local time at GEO, looking down at the north pole. Shaded region represents Earth shadow period.

periods of low storm activity considered here. The ratio of hot to cold ion current collected by the spacecraft is roughly proportional to $T_{i,C}/T_{i,H}$, where the subscripts C and H denote cold and hot ions, respectively. Considering the temperature ranges for the hot and cold ion populations, the current due to the hot ions is around 1-5% of that from the cold ions. Thus, in the charging computations for the quiet storm conditions only the cold ion population will be used to compute the plasma ion currents as it predominates over the contributions from hot ions.

The data taken from Reference 32 are presented in Figure 4.4. To provide continuous functions for the various parameters, polynomial fits are used, and are chosen to provide continuity across midnight ($f(0) = f(24)$). The function used to fit each set of data values is

$$f(x) = \sum_{i=0}^{5} a_i x^i,$$

where x represents local time in hours, as illustrated in Figure 4.5. The coefficients a_i for the electron density, electron temperature, and ion density are summarized in Table 4.1. Unfortunately, no data are available for the cold ion temperature variations as a function of local time, so a constant value of T_i =50 eV is used. The fit functions are plotted with their corresponding data sets in Figure 4.4.

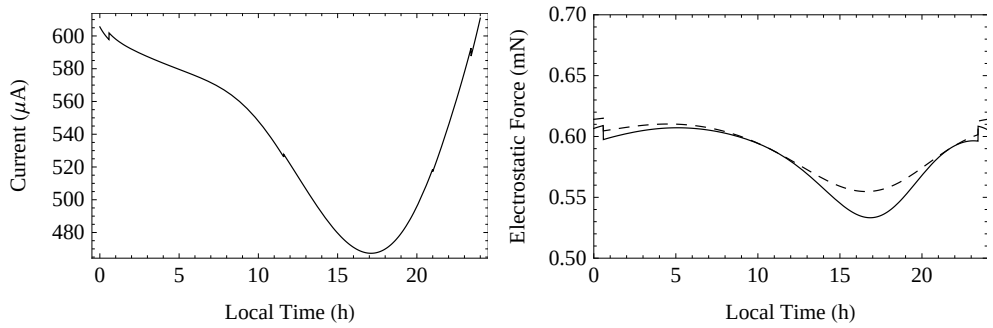

(a) Optimal Current (b) Resulting E-Force

Figure 4.6: a) Optimal electron beam current as a function of local time and b) electrostatic force resulting from optimal beam current (dashed) and constant current of 540 μA (solid). The results shown assume $E_{EB} = 40keV$, $r_T = 2$ m, and $r_D = 0.935$ m.

4.2 Space Weather Impacts on Tugging

4.2.1 Beam Current Modification

The electron beam is what drives the charging of both the tug and deputy. The beam current and energy are each factors that contribute the resulting potentials achieved by the tug and deputy. Here we will treat the beam energy as a constant, with a value of E_{EB} =40 keV. With a constant beam energy, beam current control is considered as the primary method for electrostatic force manipulation. Two different scenarios are considered: constant beam current and varied beam current. The constant beam current scenario is straightforward; a particular current value is chosen and maintained throughout the duration of the tugging. A variable current, on the other hand, requires an analysis of the space weather environment fluctuations over a typical day to help choose an appropriate current profile.

The magnitude of the electrostatic force between deputy and tug is directly responsible for the rate at which reorbiting occurs. A larger force will yield a faster reorbiting time, and so a method for maximizing this force using beam current control is desired. In this study, an open-loop current control strategy as a function of local time is used, which assumes known nominal GEO space weather variations. The following results assume a beam energy of 40 keV, a tug-deputy separation distance of 12.5 m, a tug radius of 2 meters, and a deputy radius of 0.935

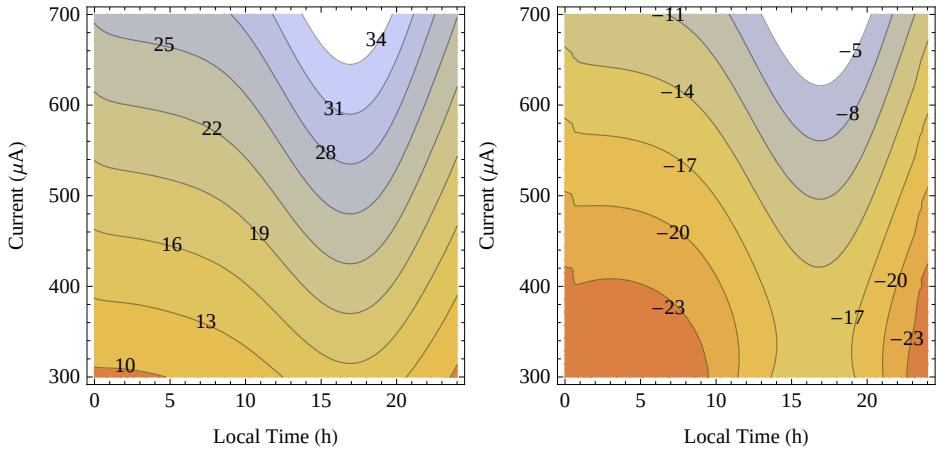

(a) ϕ_T (kV) (b) ϕ_D (kV)

Figure 4.7: Potentials achieved by tug and deputy as a function of local time for a range of currents. The results shown assume $E_{EB} = 40keV$, $r_T = 2$ m, and $r_D = 0.935$ m.

meters. The deputy radius is chosen to provide an equivalent surface area to the cylindrical deputy model used in the numerical simulation later in the paper. To determine the optimal current, the *FindMinimum* numerical minimization tool in Mathematica is used. Using the electrostatic tractor force expression in Eq. (2.4) as the function to be minimized, the optimal current which will yield the largest electrostatic force for a given local time is computed. Note that Eq. (2.4) will always be negative due to the opposite polarities of the charges q_T and q_D. The optimal current history is shown in Figure 4.6(a), and the resulting electrostatic force in Figure 4.6(b). The discontinuities on either side of midnight are due to the lack of photoelectron emission by the deputy while in the earth's shadow.

The maximum beam current occurs at midnight, while the minimum occurs around 17:00. To explain this trend requires an examination of the tug and deputy potentials as a function of beam current and local time. Figure 4.7 shows these potentials for a range of currents between 300 and 700 μA. If a fixed current is held throughout the day, the tug will experience its maximum potential around dusk. This is due to the trend in electron density. As the electron density decreases after noon, there is less electron current returning to the tug for a given potential. In order to balance electron beam emission with the plasma electron current, the tug must settle to a higher potential.

The deputy, on the other hand, experiences its minimum potential at the same time that the tug experiences its maximum. A casual study of the space weather trends would suggest that this is due to increasing ion density after noon. While this trend does contribute partially to the decrease in deputy potential, the primary factor in this reduction is the secondary electron emission generated by the incoming electron beam current. The amount of secondary electrons emitted due to an incoming electron is a function of the incoming electron's energy. The maximum secondary electron yield occurs when the energy of an incoming electron is equal to $E_{\max} = 300$ eV in the model implemented here. As the energy of an incoming electron increases, the corresponding secondary electron yield is reduced. The energy of the incoming electrons from the electron beam is equal to the beam energy minus the potential difference between tug and deputy, i.e. $E_{\text{eff}} = E_{EB} - q\phi_T + q\phi_D$. As the tug potential ϕ_T increases after noon due to lower electron density, the energy of the incoming beam electrons is reduced considerably. These lower energy electrons, in turn, result in a higher secondary electron current that reduces the deputy potential.

It is also at this dusk period where the difference in the magnitudes of tug and deputy potentials is at its greatest point. There is an ideal potential difference between tug and deputy that will yield the maximum electrostatic force. In Reference 100, expressions for these ideal potentials in a vacuum are derived as

$$\phi_T = \frac{E_{EB}}{2}\frac{\rho^2 - 2\rho r_D + r_T r_D}{(\rho - r_T)(\rho - r_D)} \tag{4.8a}$$

$$\phi_D = \frac{E_{EB}}{2}\frac{\rho^2 - 2\rho r_T + r_T r_D}{(\rho - r_T)(\rho - r_D)}. \tag{4.8b}$$

These relationships assume that the potential difference between tug and deputy is equal to the electron beam energy ($E_{EB} = q\phi_T - q\phi_D$). In reality, this will never be the case because the various currents that contribute to the charging process cause some losses in efficiency. Still, this ideal potential split provides a baseline for analyzing the reasons why the minimum forces occur when they do. Using Eq. (4.8) yields ideal potentials of ϕ_T =22.2 kV and ϕ_D =-17.8 kV. The magnitudes of the actual potentials achieved using the ideal current history are shown in Figure 4.8, along with the values computed from Eq. (4.8). The deputy potential is always smaller than its ideal value,

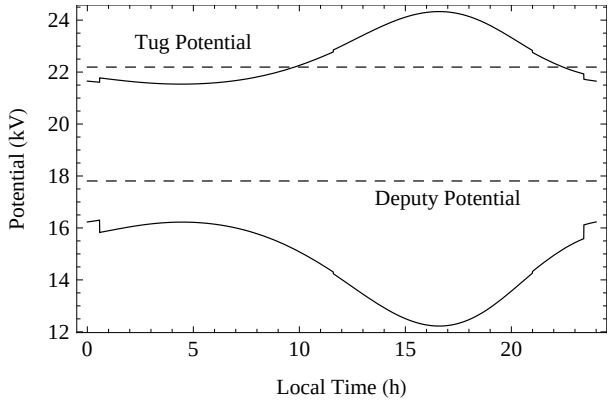

Figure 4.8: Potential magnitudes of tug and deputy that result from applying ideal current history. Dashed lines represent ideal potentials computed assuming $E_{EB} = q\phi_T - q\phi_D$.

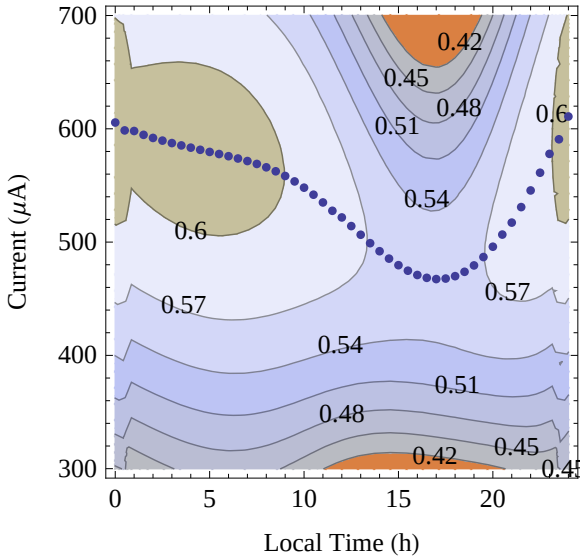

Figure 4.9: Electrostatic forces (in mN) computed for a variety of electron beam current values as a function of local time. Data points illustrate the ideal current history.

which reflects the losses due to the charging process. Note that the maximum electrostatic force occurs when the potential split best approximates the ideal value. Reducing the beam current during the post-noon timeframe is necessary for limiting the increase in the difference between tug and deputy potentials. Without reducing the current, the tug potential would climb higher and the deputy potential would descend lower, further deviating from the ideal split. This explains why the ideal current history follows the trend in Figure 4.6(a).

We now turn our attention to the case of maintaing a constant electron beam current throughout the duration of the orbit. Choosing an ideal current history is dependent on knowledge of the space weather environment, and such information may not be available in real time. A much simpler approach would be to simply hold a fixed beam current. Of course, there will be some reduction in the magnitude of the electrostatic forces, which may or may not be significant enough to severely impact performance of the tugging process. Instead of varying the current with local time, a fixed current of 540 μA is used. The resulting electrostatic forces are shown in Figure 4.6(b). Comparing with the results from the ideal current history, the largest reduction in electrostatic force occurs during the dusk period discussed previously. Again, maintaining a constant current results in an increase in tug potential and decrease in deputy potential during this period that leads to a weaker electrostatic force. Even at the worst point, the reduction in electrostatic force is no more than about 5%.

To illustrate why the losses are small, a plot of the electrostatic force as a function of local time and current is presented in Figure 4.9. Also plotted is the ideal current history. The regions around the ideal current values are relatively flat, featuring shallow force dropoffs. While the ideal current varies by 140 μA throughout the course of a day, losses of no more than 5% can be achieved by maintaining a constant current of anywhere between 400 and 550 μA. Again, this raises the question of whether or not the added complexity required to predict an ideal current as a function of space weather is worth it when very similar performance can be obtained by simply maintaining a fixed current with a large margin of error.

4.2.2 Numerical Simulation

A full numerical simulation incorporating the charging model and relative motion is performed. The $\boldsymbol{\sigma}$-set relative motion control law is used to stabilize the position of tug relative to deputy. As detailed previously, errors in estimated charges can lead to a collision between tug and deputy. The control gains need to be selected appropriately to prevent such an occurrence. To determine the lower limit for K_L, we consider the impacts of changing space weather condi-

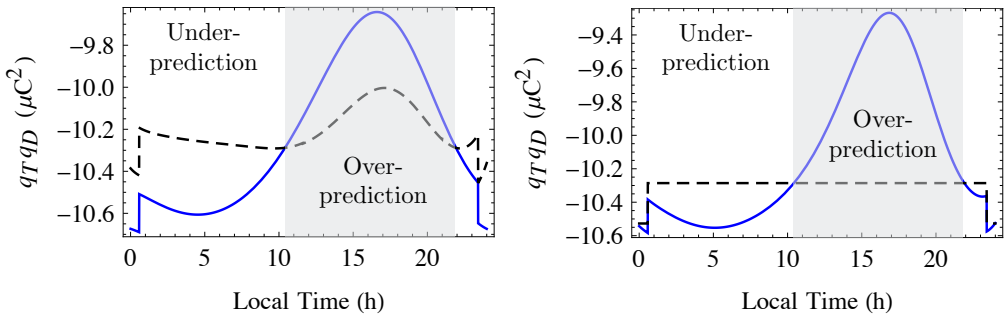

(a) Ideal I_t (b) $I_t = 540$ μA

Figure 4.10: Charge product $q_T q_D$ for a) ideal beam current history and b) constant beam current of 540 μA. Solid lines represent true charge product, while dashed lines represent estimated values.

tions on charge prediction. Because space weather conditions are dynamic and may be difficult to incorporate into a realtime estimate, constant average values are used for charge prediction. Considering the expected parameter ranges shown in Figure 4.4, values of $n_i = 7$ cm^{-3}, $T_i = 50$ eV, $n_e = 0.7$ cm^{-3}, and $T_e = 1.7$ keV are used in the charging model to estimate the charges on tug and deputy. The resulting true and estimated charge products as a function of local time are shown in Figure 4.10, assuming $r_T = 2$ m and $r_D = 0.935$ m. Results are computed using both the ideal beam current history and a constant beam current of 540 μA. There is a roughly even split in the amount of time that is spent in under-prediction versus time spent in over-prediction. During periods of over-prediction, some performance loss occurs because of the smaller electrostatic force that results from a larger separation distance. This is somewhat balanced by the increased performance obtained during under-prediction when the tug and deputy are closer than desired.

The difference between true and estimated charge products is used to bound K_L. For the ideal current history, the max under-prediction occurs just before 4:00 with a $\Delta Q_{\max} = 0.35$ μC^2. For constant current of 540 μA, the worst under-prediction occurs just after 5:00 with a $\Delta Q_{\max} = 0.21$ μC^2. The tug and deputy masses are required for evaluation of Eq. (2.46); values of $m_T = 500$ kg and $m_D = 1000$ kg are used here and in the following numerical simulation. Using the higher value of $\Delta Q_{\max} = 0.35$ μC^2, the lower limit of K_L is found to be $K_L = 3.26 \times 10^{-8}$ s^{-2}.

For the debris reorbiting scenario considered in this study, slight errors between the true and

Table 4.2: Initial orbital elements of tug and deputy.

	a (km)	e	i (°)	Ω (°)	ω (°)	ν (°)
Deputy	42164	0	0	0	0	0
Tug	42164.075	1e-6	-0.001	0	0	1e-5

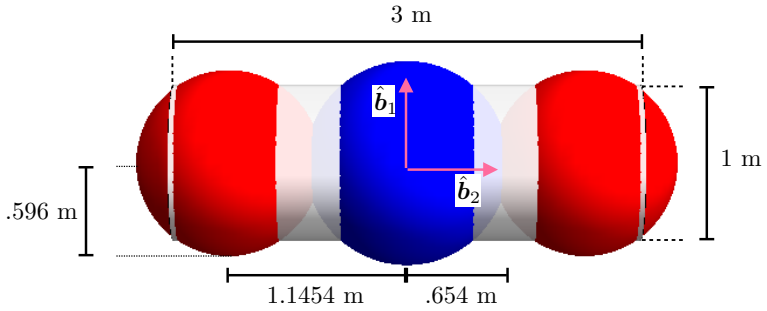

Figure 4.11: Multi-sphere model used to represent the 3x1 meter cylindrical deputy object.

desired separation distance are not a serious concern. The ultimate goal is raising a debris object into a graveyard orbit,[52] and taking slightly more or less time to get there is not a major obstacle to achieving this goal. If more precision is required during a deputy reorbiting maneuver, these slight errors could have a significant impact and would need to be considered.

The spacecraft charging model is implemented into a full numerical simulation and used to model relative motion while performing charge transfer and electrostatic tugging. A total simulation period of two days is used, and both the ideal current history and a constant beam current of 540 μA are applied. The initial orbital elements for both tug and deputy are summarized in Table 4.2. In the debris reorbiting scenario modeled here, the tug maintains a constant position 12.5 meters ahead of the deputy in the along track direction, which corresponds to reference sigma-set values of $L_r = 12.5,\ \sigma_{1r} = 1,\ \sigma_{2r} = 0$ (shadow set values of $L_{rs} = -12.5,\ \sigma_{1rs} = -1,\ \sigma_{2rs} = 0$). The control gains used are $[K] = 3.75 \times 10^{-7}[I_{3\times3}]$ s^{-2} and $[P] = 1.13 \times 10^{-3}[I_{3\times3}]$ s^{-1}. Note that the values K_i are an order of magnitude larger than the lower limit required to avoid collision, and the gains will result in a settling time of 2.4 hours.

4.2.2.1 Multi-Sphere Model of the Deputy

The tug is modeled using a sphere with a radius of 2 meters. Rather than treating the deputy object as spherical, a cylindrical model is used instead. This results in off-axis forces that are no longer necessarily aligned with the line of sight from tug to deputy. Furthermore, electrostatic torques affect the attitude motion of the deputy. As the deputy tumbles, even with a fixed separation distance between tug and deputy, the electrostatic force magnitude will no longer be constant. Incorporating a non-spherical model allows for inclusion of these effects, which in turn provides for a more realistic simulation of charged relative motion. In general, a debris object will be non-spherical and the electrostatic tugging process would experience these phenomena.

The multi-sphere method (MSM) is used to compute the electrostatic forces and torques between tug and deputy.[109] The deputy is modeled as a cylinder with a diameter of 1 meter and a height of 3 meters. To compute the charge on the deputy an approximation of three spheres is used, as depicted in Figure 4.11. In the deputy body frame $\mathcal{B} : \{\hat{\boldsymbol{b}}_1,\ \hat{\boldsymbol{b}}_2,\ \hat{\boldsymbol{b}}_3\}$ each sphere is located at a position of $\boldsymbol{r}_i$ and has an associated radius of R_i. The sphere locations and radii are presented in Table 4.3.

The procedure for computing the electrostatic forces and torques between tug and deputy follows. First, the potentials on tug and deputy are computed using the charge model detailed above. Each sphere on the deputy is assumed to have the same potential of ϕ_D. Denoting the charge on each individual sphere as q_i, the matrices $\boldsymbol{\Phi} = [\phi_D\ \phi_D\ \phi_D\ \phi_T]^T$ and $\boldsymbol{q} = [q_1\ q_2\ q_3\ q_T]^T$ are constructed. Using the position dependent capacitance model, the potentials and charges are related through

$$\boldsymbol{\Phi} = k_c[C_M]^{-1}\boldsymbol{q}. \tag{4.9}$$

The inverse of the position dependent capacitance matrix, $[C_M]^{-1}$, is then expanded as

$$[C_M]^{-1} = \begin{bmatrix} 1/R_1 & 1/r_{1,2} & 1/r_{1,3} & 1/r_{1,T} \\ 1/r_{2,1} & 1/R_2 & 1/r_{2,3} & 1/r_{2,T} \\ 1/r_{3,1} & 1/r_{3,2} & 1/R_3 & 1/r_{3,T} \\ 1/r_{T,1} & 1/r_{T,2} & 1/r_{T,3} & 1/r_{T}, \end{bmatrix}. \tag{4.10}$$

where $r_{i,j}$ is the distance between spheres i and j. The subscript T refers to the tug, so that $r_{1,T}$ is the separation distance between deputy MSM sphere 1 and the tug. To solve for the charges, $\boldsymbol{q}$, Eq. (4.9) is inverted. The total electrostatic force acting on the deputy is obtained by summing up the forces on the individual MSM spheres, i.e.

$$\boldsymbol{F}_{e,D} = -k_c q_T \sum_{i=1}^{3} \frac{q_i}{r_{i,T}^3} \boldsymbol{r}_{i,T}, \tag{4.11}$$

where $\boldsymbol{r}_{i,T}$ is the vector from MSM sphere i to the tug. This force acts equal and opposite on the tug, so that $\boldsymbol{F}_{e,T} = -\boldsymbol{F}_{e,D}$. The total torque acting on the deputy resulting from the electrostatic interaction with the tug is computed as

$$\boldsymbol{T}_e = -k_c q_T \sum_{i=1}^{3} \frac{q_i}{r_{i,T}^3} \boldsymbol{r}_i \times \boldsymbol{r}_{i,T}. \tag{4.12}$$

The spherical geometry of the tug prevents any electrostatic torques from acting on it.

4.2.2.2 Tug and Deputy Dynamics

To propagate the orbits of both tug and deputy, inertial two-body dynamics are used. In the case of the tug, the motion is governed by gravity, electrostatic forces, and thrusting. The tug trajectory is determined through integration of

$$\ddot{\boldsymbol{p}}_T = -\frac{\mu}{p_T^3} \boldsymbol{p}_T + \frac{\boldsymbol{F}_{e,T}}{m_T} + \frac{\boldsymbol{T}_T}{m_T}, \tag{4.13}$$

where $\boldsymbol{p}_T$ is the position of the tug in the earth centered inertial (ECI) frame. Similarly, the deputy orbit is propagated using

$$\ddot{\boldsymbol{p}}_D = -\frac{\mu}{p_D^3} \boldsymbol{p}_D + \frac{\boldsymbol{F}_{e,D}}{m_D}. \tag{4.14}$$

Table 4.3: Radii and body-frame sphere locations used to represent cylinder in MSM model.

Sphere	Body Frame Location $\boldsymbol{r}_i$ (m)	Sphere Radius R_i (m)
1	-1.454$\hat{\boldsymbol{b}}_2$	.5959
2	$\boldsymbol{0}$	.6543
3	1.454$\hat{\boldsymbol{b}}_2$	.5959

Local time is computed by assuming the sun direction is $\hat{\boldsymbol{r}}_\odot = [1\ 0\ 0]^T$ in the ECI frame. The tug thrust $\boldsymbol{T}_T$ is computed with Eqs. (2.4.1) and (2.39), and it is assumed the deputy and tug orbital positions are known. The electrostatic force compensation in the controller is obtained using the averaged space weather values $n_i = 7$ cm^{-3}, $T_i = 50$ eV, $n_e = 0.7$ cm^{-3}, and $T_e = 1.7$ keV, and assumes the deputy is spherical with a radius of $r_D = 0.935$ m. The true electrostatic force used to propagate the orbits uses the MSM cylindrical model and the time-varying space weather conditions in Figure 4.4.

The electrostatic forces and torques are a function of the deputy attitude, and so deputy attitude motion must be accounted for. Modified Rodrigues parameters ($\boldsymbol{\eta}$) are used to describe the deputy attitude, with the corresponding attitude dynamics[97]

$$\dot{\boldsymbol{\eta}} = \frac{1}{4}\left[(1-\eta^2)[I_{3\times3}] + 2[\tilde{\boldsymbol{\eta}}] + 2\boldsymbol{\eta}\boldsymbol{\eta}^T\right]\boldsymbol{\omega} \tag{4.15a}$$

$$[J]\dot{\boldsymbol{\omega}} = -\boldsymbol{\omega}\times[J]\boldsymbol{\omega} + \boldsymbol{T}_e, \tag{4.15b}$$

where

$$[J] = \begin{bmatrix} 893.75 & 0 & 0 \\ 0 & 125.0 & 0 \\ 0 & 0 & 731.25 \end{bmatrix} \text{ kg m}^2$$

is the deputy inertia tensor. The initial conditions used to propagate the deputy attitude are $\boldsymbol{\eta}_0 = \boldsymbol{0}$, $\boldsymbol{\omega}_0 = [1\ 2\ -0.6]^T$ (deg/s).

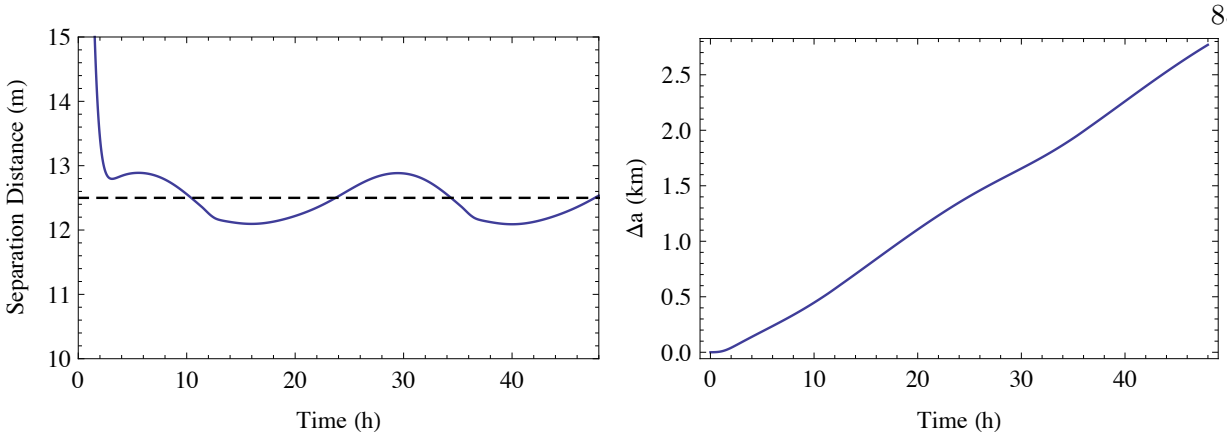

(a) Separation Distance (b) SMA Change

Figure 4.12: a) Separation distance between tug and deputy and b) increase in deputy semi-major axis with application of ideal beam current history.

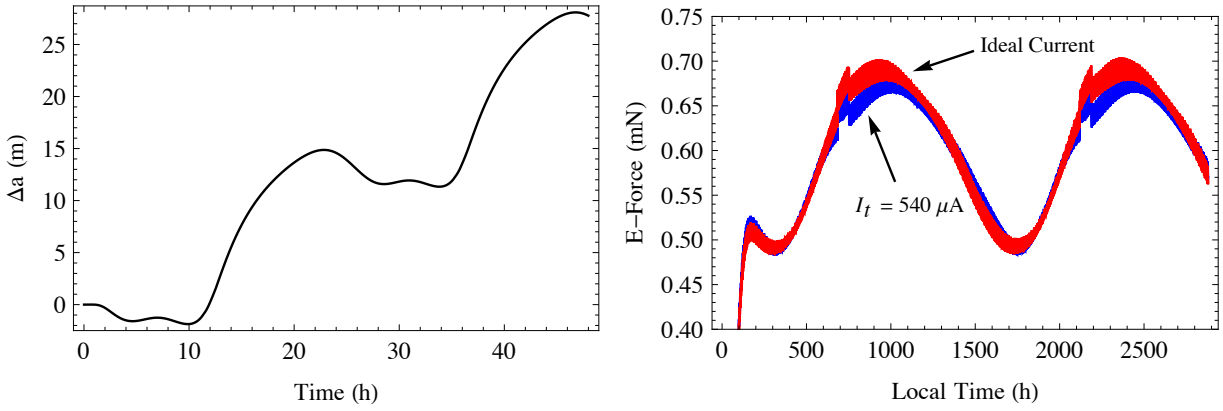

(a) SMA Differences (b) Electrostatic Forces

Figure 4.13: a) Difference in deputy semi-major axis evolution and b) electrostatic force magnitudes resulting from application of ideal beam current history and a constant beam current of 540 μA.

4.2.2.3 Simulation Results

First, the effects of the ideal beam current history on relative motion and reorbiting are considered. After approximately 2.5 hours, the tug and deputy achieve the desired leader-follower alignment. The separation distance between tug and deputy throughout the duration of the simulation is presented in Figure 4.12(a). Though the desired separation distance is 12.5 meters, the actual separation oscillates about this value with a range of 0.8 meters. This results from the errors between the estimated and true electrostatic forces, and is expected. For the debris reorbiting

scenario, these slight oscillations are of minor concern. The ultimate goal is merely increasing the semi-major axis of the deputy object to a high enough level to prevent reentry into GEO. Slight deviations from the desired performance do not hinder this goal.

The increase in deputy semi-major axis during the maneuver is shown in Figure 4.12(b). After two days, the deputy semi-major axis is about 2.6 kilometers larger than at the beginning of the maneuver. This agrees with earlier work predicting reorbiting performance using the electrostatic tug for debris mitigation applications, where semi-major axis corrections of 1-3 km per day are expected.[43,98] There are slight variations in the rate of change of the semi-major axis, and these correspond with the periods of charge over- and under-prediction. Charge over-prediction occurs during the time of day when the electrostatic forces are at their smallest, and separation distances are at their largest. As a result, there is a weaker tug force pulling on the deputy, resulting in a slower increase in semi-major axis. The opposite occurs during the periods of under-prediction.

Next, attention is paid to application of a constant beam current of 540 μA throughout the maneuver. The separation distance history is very similar to what is depicted in Figure 4.12(a), and is not shown here for the sake of brevity. The same oscillations occur, with periods of smaller and larger separation distances than desired. To assess the performance differences between the constant beam current and ideal beam current histories, the resulting semi-major axis changes are compared. The difference between the deputy semi-major axis during the ideal and constant current cases is shown in Figure 4.13(a). Positive values indicate that the ideal beam current history has achieved a larger semi-major axis increase than the constant beam current. A positive slope indicates the using the ideal current history is increasing the semi-major more quickly, while a negative slope implies that the constant beam current is increasing the semi-major axis more quickly. After 48 hours, charge control using the ideal beam history results in an additional 25 meter increase in the semi-major axis as compared to maintaining a constant beam current of 540 μA. This means that using the constant beam current would result in a performance loss on the order of 1%. This again raises the question of whether or not the performance benefits resulting from the optimized electrostatic force are worth the added complexity as compared to simply maintaining a constant

beam current that works well for the expected range of nominal space weather conditions.

The ideal beam current history should result in larger electrostatic forces throughout the maneuver, which implies that the rate of semi-major axis change will always be larger than for the fixed current case. However, as seen in Figure 4.13(a), this is not the case. There are periods where the fixed beam current actually outperforms the ideal beam current case. Figure 4.13(b) shows the electrostatic forces resulting from both current histories. At certain times, the constant 540 μA current produces a larger electrostatic force than the ideal beam current. A few factors contribute to this result. First, the ideal beam current is computed assuming a spherical deputy geometry. The true physical model implemented in the numerical simulation is cylindrical, and this changes the current balance affecting the deputy potential. Specifically, the photoelectron current will not be equivalent between cylinder and sphere, and for the cylinder is dependent on the orientation of the deputy relative to the sun. Secondly, the differences in force estimation between the two cases result in slightly different separation distance histories. There are times when the constant current results in a closer separation distance than the ideal beam current. Because the voltages achieved in both cases are similar, the smaller separation distances yield larger forces for the constant current. These periods are brief, and generally the ideal beam current history does result in better performance. The widths of the electrostatic force curves in Figure 4.13(b) are due to the deputy tumbling. Small oscillations occur in the electrostatic force magnitude due to this attitude motion.

4.3 Impact of Geomagnetic Storm Events on Tractor Performance

Thus far, the electrostatic tractor performance has been analyzed for quiet ($k_p = 1.5$) storm conditions. Now, the effects of geomagnetic storm events are considered. When a geomagnetic storm occurs, the population of lower energy ions (50 eV) in the period following local midnight is lost, with a higher energy population of slightly lower density (1 cm^{-3}) remaining.[31,32] Solar storm events also provide a higher energy population of electrons, with energies as high as a few tens of keV. This phenomenon was experienced by the ATS-5 satellite and recorded in GEO space weather measurements taken by the magnetospheric plasma analyzer (MPA) instruments flown by

Table 4.4: Plasma parameters used for geomagnetic storm analysis

Storm Level	n_e (cm^{-3})	T_e (keV)	n_i (cm^{-3})	T_i (keV)
Moderate ($k_p = 6$)	1	4.7	1	15
Severe ($k_p = 8 - 9$)	1	20	1	20
Quiet ($k_p = 1.5$)	0.925	2.64	3.05	0.05

Los Alamos National Laboratory.[8] When a spacecraft enters into eclipse during a storm event it may naturally charge to potential levels in excess of -10 kV, depending on the severity of the geomagnetic storm. During storm events experienced by ATS-5, typical potentials achieved in shadow were 3-4 kV (negative polarity), with lows of 70-100 V and highs in above 10 kV.[31] Note that a spacecraft experiences eclipse for under an hour each day in the 3-4 weeks before and after an equinox. Over an electrostatic tractor reorbiting scenario with a lifetime of several months, this represents a very small portion of the total operating time. When a spacecraft is in sunlight, the photoelectron current precludes these very high natural charging levels. ATS-5 observed a maximum potential of -300 V in the sunlight, and reached potentials of between -50 and -300 V several times. All of these charging events occurred during periods of very high solar activity, and occurred between local midnight and dawn. The SCATHA satellite was also used to study natural charging in sunlight, and recorded potentials as high as -740 V.[78] Charging events in excess of -100 V only occurred for k_p indices of 2 or greater.

The NOAA space weather scale classifies the severity and frequency of geomagnetic storms, with a scale ranging from G-1 (minor, $k_p = 5$) to G-5 (extreme, $k_p = 9$).[87] In an 11 year solar cycle, minor storm activity is expected for roughly 900 days, with extreme storm events occurring much less frequently, only about 4 times. For the analysis of storm activity, two storm conditions are considered: a moderate geomagnetic storm, G-2 on the NOAA scale, with $k_p = 6$ and a worst-case severe storm event. Only the effects on the charge transfer process are considered. Severe solar activity can be harmful to spacecraft subsystems, causing electrical failures and differential charge driven arcing events, but consideration of these phenomena is beyond the scope of the current work. For the moderate storm condition ($k_p = 6$), data from Reference 32 are used to determine plasma

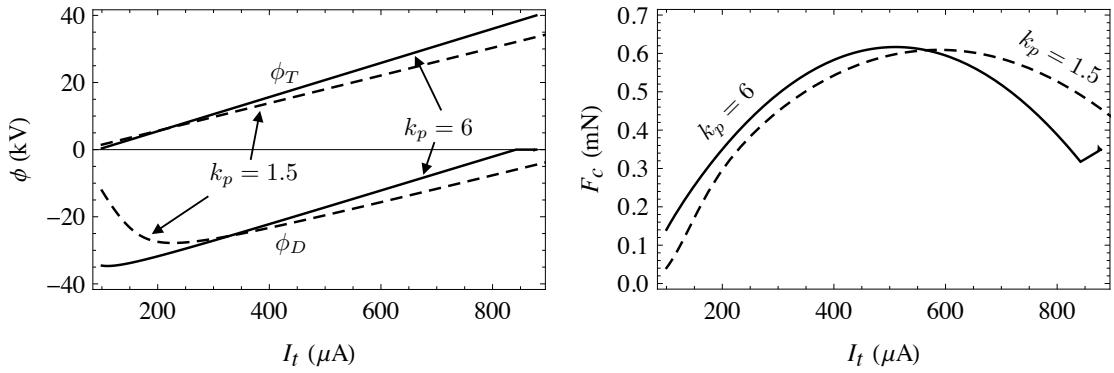

(a) Potentials (b) E-Force

Figure 4.14: a) Potentials and b) electrostatic force as a function of electron beam current for moderate solar storm event (solid) and quiet solar conditions (dashed). Results assume $r_T = 2$ m, $r_D = 0.935$ m, and $E_{EB} = 40$ keV.

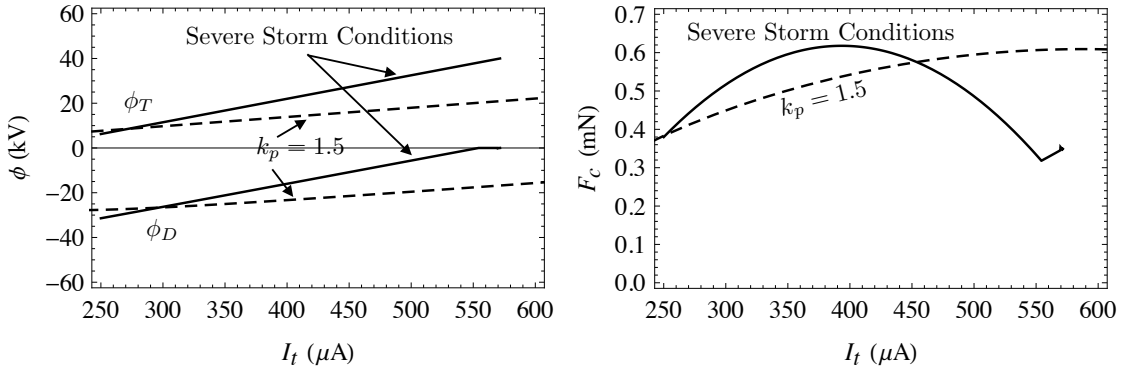

(a) Potentials (b) E-Force

Figure 4.15: a) Potentials and b) electrostatic force as a function of electron beam current for severe solar storm event (solid) and quiet solar conditions (dashed). Results assume $r_T = 2$ m, $r_D = 0.935$ m, and $E_{EB} = 40$ keV.

temperatures and densities. The data are taken at a local time of 3:00, which corresponds to the post-midnight period where high natural charging is observed. For the severe storm condition, the plasma parameters corresponding to a severe storm in Reference 73 are used. The ion and electron densities for both storm conditions are presented in Table 4.4, along with the quiet ($k_p = 1.5$) conditions computed for 3:00.

To determine the effects of these storm conditions, the tug and deputy potentials are computed as a function of electron beam current, for $E_{EB} = 40$ keV, $r_T = 2$ m, and $r_D = 0.935$ m.

The electrostatic force is also computed, assuming a separation distance of 12.5 m. The potentials and forces are also computed for the quiet solar conditions ($k_p = 1.5$) to serve as a baseline for comparison. For the moderate solar storm event ($k_p = 6$), the results are illustrated in Figure 4.14. Also shown are potentials computed using the quiet conditions. The storm conditions result in the tug charging to higher potentials for a given electron beam current. For the deputy, the maximum potential occurs at a lower beam current level, and the potential decreases at a faster rate as the beam current is increased. The tug reaches its maximum potential ($q\phi_T = E_{EB}$) at a lower current level than for quiet space weather conditions. Considering the electrostatic forces that result, a slightly higher maximum force occurs for the storm condition and it occurs at a lower beam current level. The potentials and forces are also computed for the severe storm conditions, and are shown in Figure 4.15. The same effects are observed that are seen for moderate storm conditions, but to a higher degree. The tug potential increases more rapidly as beam current is increased, and the deputy potential decreases in a similar fashion. For the severe storm condition, the tug reaches its maximum potential for a beam current of about 575 μA, while in the moderate storm condition the tug potential is at its maximum for a beam current of almost 900 μA. As the storm severity increases, less current is required to maximally charge the tug. Looking at the electrostatic forces for the severe storm condition, the maximum is once again slightly above that of the quiet condition, but occurs at much less current.

Clearly, geomagnetic storm events do not prevent charge transfer for the electrostatic tractor. In fact, the storm conditions facilitate the charging. A slightly higher electrostatic force is possible, and less current is required to achieve it. Current modification is required to compensate for the onset of these storm events, however. When considering the nominal GEO space weather conditions for quiet periods of activity, holding a fixed current does not result in significant performance losses (see Figure 4.6(b)). For the tug and deputy dimensions considered here, a constant beam current of 540 μA is used. If a severe solar storm event occurs and the beam current is not modified to compensate, Figure 4.15 shows that a performance loss of 40% results. Thus, to account for solar storm events the beam current should be controllable, which is likely to be the case anyway. The

analysis of solar storm events on tractor performance reveals that the worst-case scenario from a performance perspective is actually the nominal, quiet space weather conditions. For this reason, the $k_p = 1.5$ plasma parameter values are used in all further studies.

4.4 Relative Sizing Considerations

The maximum allowable electron beam current is driven by the energy of the beam. If enough current is emitted, the tug will achieve a potential equal to the beam energy. Beyond this limit, any emitted beam electrons will be captured by the tug because they do not have enough energy to escape the tug potential well. This has important implications regarding the relative sizing between tug and deputy that will still permit charge transfer. If the tug vehicle is much smaller than the deputy, the tug will reach its potential limit before it has emitted enough current to charge the deputy. This will significantly hinder performance if the sizing difference is large enough. Thus, it is of interest to identify how large a tug vehicle must be to tow a deputy object of a given size.

4.4.1 From a Deputy Potential Perspective

To identify the conditions under which charge transfer is no longer possible, a threshold condition must be defined. Here, ϕ_c is used to represent a cutoff deputy potential. Any scenario that yields a deputy potential below ϕ_c is no longer considered as a case of successful charge transfer. Note that a failure to achieve charge transfer will result in drastically reduced performance. Without a sufficient absorbed beam electron current, the deputy will result in a high positive potential due to the loss of photoelectrons. Because the charging model is not applicable to this scenario, however, performance results for this condition are ignored. For the following analysis the quiet ($k_p = 1.5$) space weather conditions at 17:30 are used, with values of $n_e = 0.47$ cm^{-3}, $T_e = 1180$ eV, $n_i = 11$ cm^{-3}, $T_i = 50$ eV.

First, a relationship between emitted beam current and beam energy required to achieve charge transfer is considered for a range of tug and deputy sizes. That is, given a particular ratio of tug and deputy sizes and an emitted beam current, what beam energy E_c would be required to yield

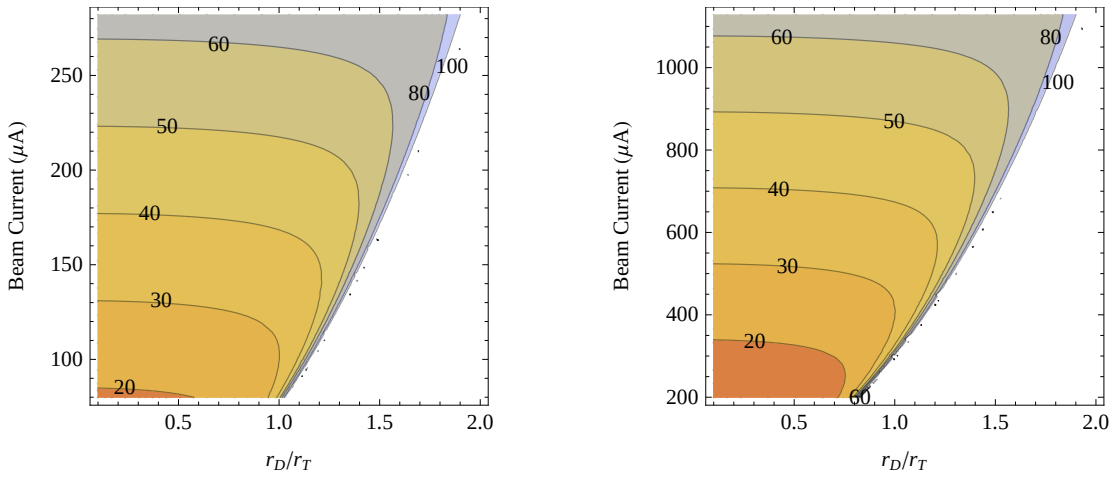

(a) $r_T = 1$ m (b) $r_T = 2$ m

Figure 4.16: Beam energy (E_c, in keV) required to reach charging threshold of $\phi_c = -1$ kV for a variety of emitted beam currents and size ratios. The plots are

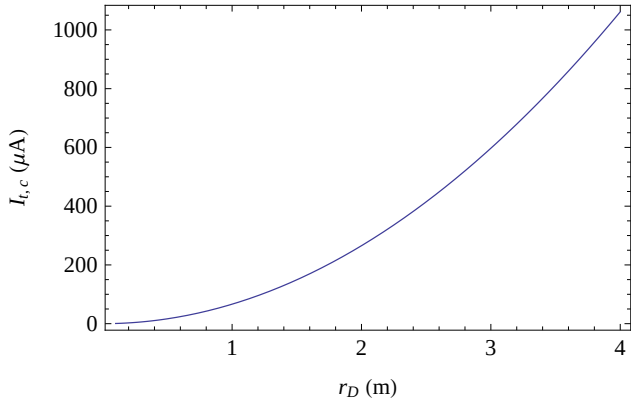

Figure 4.17: Minimum current required for charge transfer in the limit of $E_{EB} \to \infty$, assuming a threshold of $\phi_c = -1000$ V.

ϕ_c? If the actual beam energy is below E_c, then charge transfer is not possible. If the beam energy is above E_c, then charge transfer is possible and deputy potentials above ϕ_c are achievable. Using a numerical root finder, the critical values of E_c are computed for tug sizes of 1 and 2 meters as a function of emitted current and the ratio of deputy and tug radii, r_D/r_T. The charging threshold is defined as ϕ_c = -1 kV. The results are shown in Figure 4.16, and several interesting conclusions

can be drawn. First, for any given beam energy E_c, there is an upper limit on the deputy size for which charge transfer is possible. For example, considering the $E_c = 40$ keV contour has its outermost edge at roughly r_D/r_T=1.2 (see Figure 4.16), any deputy size beyond 1.2 times that of the tug would preclude charge transfer. From a vehicle design perspective, this implies that for better performance a larger tug vehicle should be used. If the tug vehicle is as large or larger than the biggest expected deputy object, then charge transfer will be possible. However, a smaller tug vehicle is limited in the variety of potential deputy candidates that may be towed. There is a tradeoff that must be considered, however, because a larger tug vehicle requires more current to reach the same potential levels. More current requires more power. Thus, while a larger vehicle can potentially tow a wider range of deputy objects, it will require more power to do so.

Another interesting result shown in Figure 4.16 is the existence of a hard cutoff in the charging threshold, where higher beam energies no longer allow for the charging of larger deputy objects. It would seem that this might be a function of the size ratio r_D/r_T. However, this cutoff is merely a reflection of the fact that there is some minimum current required to balance the photoelectron and plasma ion currents and reach ϕ_c. An analytic expression for the cutoff is found by considering the limit of very large beam energies ($E_{EB} \to \infty$). While perhaps not practically realistic, computing this limit allows one to identify the minimum theoretical current that is required to accomplish charge transfer for a deputy object of a given size. In the limit of a very large beam energy, the secondary electron emission current is effectively zero, due to the fact that

$$\lim_{E_{EB}\to\infty} \kappa = 0.$$

Thus, the current balance on the deputy may be rewritten as

$$I_e(\phi_c) + I_i(\phi_c) + I_{ph}(\phi_c) + I_D(\phi_c) = 0, \tag{4.16}$$

which can be solved for I_t. Denoting $\mathcal{F}_e = qn_e w_e/4$ and $\mathcal{F}_i = qn_i w_i/4$ as the plasma electron and ion fluxes, the minimum beam current required to achieve ϕ_c is computed as

$$I_{t,c} = \left(4\mathcal{F}_i\left(1 - \frac{\phi_c}{T_i}\right) - 4\mathcal{F}_e e^{\phi_c/T_e} + j_{ph,0}\right)\pi r_D^2. \tag{4.17}$$

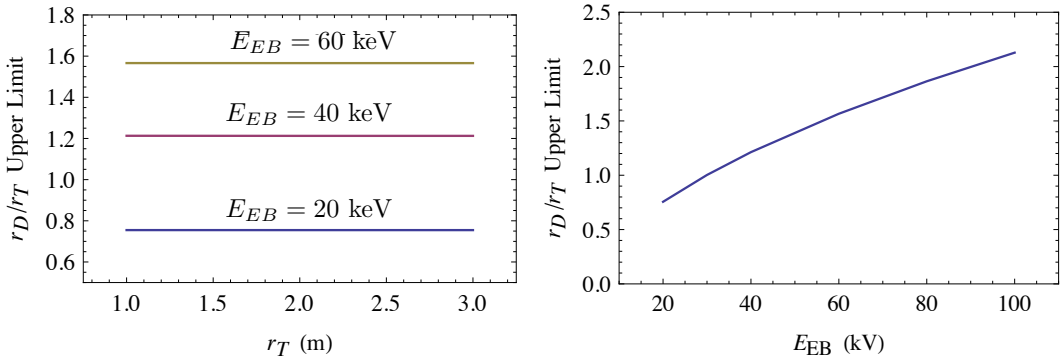

(a) Function of tug size

(b) Function of beam energy

Figure 4.18: a) Size ratio limits for a variety of tug sizes and b) size ratio limits as a function of beam energy for which charge transfer ($\phi_c - 1$ kV) is possible.

A tug vehicle that cannot emit at least this amount of current, no matter how high the beam energy, will not be able to achieve charge transfer. A plot of $I_{t,c}$ for $\phi_c = -1000$ V is shown in Figure 4.17. For finite beam energies, secondary electron emission contributes additional losses to the charge transfer process. More current than predicted in Eq. (4.17) is required to achieve charge transfer, and the beam energy must be high enough so that the total secondary electron yield is less than one. Depending on the parameters of particular case, the actual current required to achieve charging could be much higher than predicted by $I_{t,c}$.

Returning to Figure 4.16, the upper limit on the scaling parameter (r_D/r_T) for a given beam energy is consistent between the two plots. For example, for the 40 keV contour the maximum size ratio for which charge transfer can still be accomplished is roughly 1.2. The primary difference between the two cases where $r_T = 1$ m and $r_T = 2$ m is the amount of current required to reach this peak. The increased current for the larger object sizes is required to offset the higher plasma and photoelectron currents that result from increased surface areas. While it is difficult to determine an expression for the maximum size ratio that still permits charge transfer, the peaks can be computed numerically. To investigate the sensitivity of the upper limits to the tug size, the maximum allowable size ratios are computed for a range of tug radii. The results for beam energies of 20, 40 and 60 keV are shown in Figure 4.18(a). It is clear that the upper limits on the relative sizes are not sensitive

to the tug size, but rather to the beam energy. A higher beam energy allows for charge transfer onto a larger object. The upper limits on the size ratio for a range of beam energies is shown in Figure 4.18(b). At the lower end of the spectrum, a tug vehicle equipped with a 20 keV electron beam would only be capable of achieving charge transfer onto an object roughly three-quarters of its size or smaller. To achieve charge transfer onto a similarly sized object ($r_T = r_D$), the tug vehicle would need an electron beam in excess of 30 keV. As the beam energy increases, larger and larger objects can be charged. This is reflective of the fact that higher beam energies allow the tug vehicle to emit more current before it achieves charge saturation ($q\phi_T = E_{EB}$). Larger deputy objects require more current for charging, as reflected in Figure 4.17. Increasing the beam energy allows the tug to provide these higher currents for larger deputy objects.

From the perspective of achieving charge transfer, the results thus far suggest that a larger tug is better. A larger tug achieves charge transfer for a wider range of deputy object sizes while requiring less beam energy than a smaller tug. With a 40 keV electron beam, a tug vehicle with a 3 meter radius can perform charge transfer onto a deputy object with a radius in excess of 3.5 meters. A one-meter tug similarly equipped could only perform charge transfer on an object with a 1.2 meter radius. It is important to note that the results shown here are computed for the specific space weather conditions encountered at 17:30 for quiet solar conditions ($k_p = 1.5$). This particular time of day is chosen because it represents the lower end of charge transfer performance, where the electron density is lowest and the ion density is highest. While different space weather conditions would certainly lead to different results, in general the performance would be better than obtained for these particular space weather parameter values.

4.4.2 From a Force Perspective

The charge transfer analysis for varying sizes has thus far only been concerned with achieving a potential on the deputy object. However, this is really only part of the bigger picture when it comes to assessing electrostatic tractor performance. The tractor performance is dependent on the electrostatic force that exists between tug and deputy. To illustrate the impact of relative sizing on

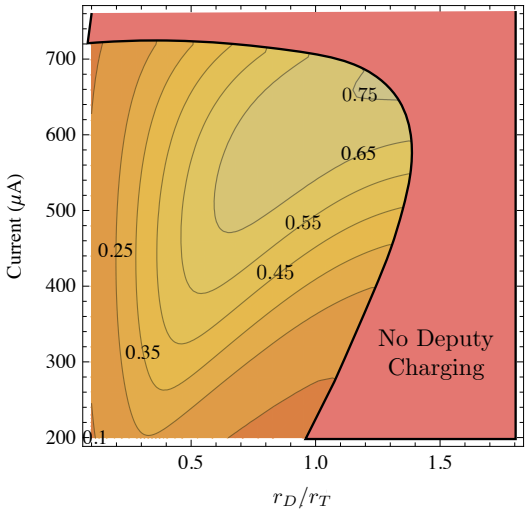

Figure 4.19: Electrostatic force magnitude (in mN) for a range of beam currents and deputy sizes, assuming a tug radius of 2 m

the resulting electrostatic force, a 2 meter tug radius is considered with a beam energy of $E_{EB} = 40$ keV. The electrostatic force magnitudes (in mN) are computed for a range of deputy sizes and beam currents. The results are shown in Figure 4.19. The upper limit on the current range is chosen as the condition that provides a tug potential equal to the beam energy ($q\phi_T = E_{EB}$). Additional current emission is not possible, because the beam electrons would be recaptured by the tug.

There are two distinct regions on the plot: conditions where charge transfer occurs and a force is computed, and conditions that prevent charge transfer. Where charge transfer fails, the charging model is insufficient to provide a potential on the deputy and a force cannot be computed. Considering the boundary of the region of charge transfer, the largest sized object that can be towed is about 1.35 times the size of the tug. The largest objects enable the largest electrostatic forces. This is due to higher capacitance for larger objects, where more charge exists on the deputy for a given potential.

4.4.3 From an Orbit Raising Perspective

Computing the electrostatic force magnitudes only tells half of the story. Larger objects tend to produce larger forces for a given potential, because the total charge on the objects increases

linearly with radius. But larger objects also tend to be heavier, meaning they may be accelerated more slowly. Ultimately, the most important performance criteria that may be considered for the electrostatic tractor is the rate at which the deputy orbit may be changed. Returning to the debris reorbiting scenario, where the objective is increasing the deputy radius by approximately 300 km, the semi-major axis increase over one day is used to quantify the tugging performance. Again, there is a need to define a lower threshold on performance to characterize acceptable performance levels. A one kilometer per day increase in the deputy semi-major axis is used as this lower bound. Assuming a circular deputy orbit, the semi-major axis increase in the deputy orbit over one day is[98]

$$\Delta a \approx \frac{4\pi}{n^2}\frac{F_c}{m_D}, \tag{4.18}$$

where n is the mean motion of the deputy orbit and m_D the deputy mass. A GEO orbit radius of 42,164 km is assumed for this analysis. The deputy mass is required to compute the semi-major axis change. Considering publicly available data on GEO satellites, Reference 96 provides a relationship between spacecraft mass and an approximate sphere radius. The simple linear expression

$$r_D(m_D) = 1.152 \text{ m} + 0.00066350\frac{\text{m}}{\text{kg}}m_D \tag{4.19}$$

provides a deputy radius for use in the charging model. While certainly not perfect, this linear relationship does capture the general trend of increased mass for larger objects and is based on actual data for GEO objects.

Considering a tug size of $r_T = 3$ meters and an electron beam energy of 40 keV, the semi-major axis increase over one day for a range of deputy sizes is shown in Figure 4.20. Again, there are two distinct regions of the plot, which correspond to successful charge transfer and no charge transfer. Using charge transfer the 3 meter tug can tow objects in excess of 4000 kg faster than the $\Delta a = 1$ km/day threshold. In fact, the maximum rate of increase in the semi-major axis for the 4000 kg objects is about 1.6 km/day. Objects of slightly less than 3000 kg can be towed at Δa =2 km/day; reaching a 3 km/day performance level is possible for objects as large as 1700 kg.

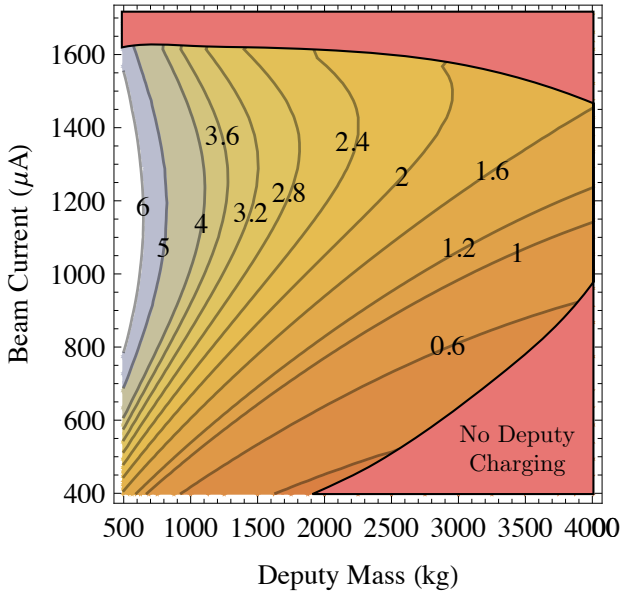

Figure 4.20: Deputy semi-major axis increase per day (in km) for a range of deputy sizes and electron beam currents. The tug size is $r_T = 3$ meters.

4.4.4 Power Considerations

All of the results regarding limitations on tug and deputy sizing highlight the challenges of tugging a deputy object larger than the tug. There are no issues achieving charge transfer when the deputy is much smaller than the tug ($r_D/r_T \ll 1$). On the contrary, charge transfer and tugging performance in general suffer when the deputy is significantly larger than the tug. This implies that the tug vehicle should be made as large as possible in order to maximize the range of objects that can be towed. Of course, there are tradeoffs to using a larger tug that must be considered. A larger tug vehicle, owing to its larger surface area, will require significantly more current to achieve a desired potential, and this current increases with the square of the tug radius. This means that doubling the tug radius will require four times as much power to achieve supercharging for a given potential. The expression

$$P_{\max} = I_{t,\max} E_{EB} \tag{4.20}$$

provides the power required for supercharging a tug vehicle ($q\phi_T = E_{EB}$). The variable $I_{t,\max}$ is the maximum current that may be emitted for the given beam energy and is computed as

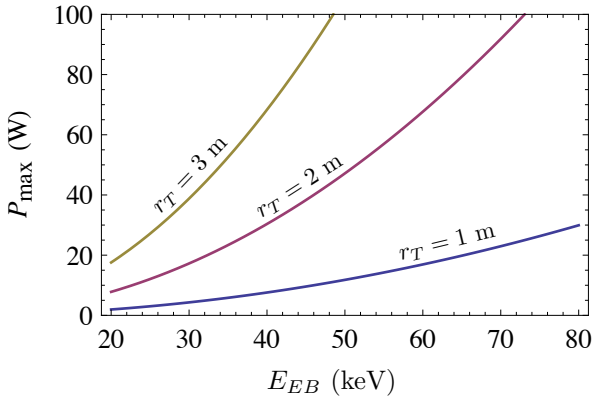

Figure 4.21: Power required to supercharge tug vehicle as a function of beam energy.

$I_{t,\max} = -I_e(E_{EB})$. Note that this serves as an upper bound on the required power, because the is the maximum amount of current that the tug can emit. Charge transfer generally requires a lower amount of current. The power required to supercharge tug sizes of 1, 2, and 3 meters is presented in Figure 4.21. Even for the largest 3 meter radius tug considered here, power levels of no more than 100 Watts are required for electron beams of around 50 keV or less.

4.5 Simultaneous Electron/Ion Beam Emission

Deputy charging is limited by the amount of current that can be delivered to it by the tug. As the tug emits more electron beam current, it will charge itself to higher potentials. This results in the beam electrons having lower energy when they reach the deputy, generally causing a higher secondary electron yield. Thus, the deputy charging can actually decrease even for higher beam currents, as illustrated in Figure 4.3. Furthermore, the plasma electron conditions can cause the tug to charge up to relatively high values and limit the deputy potential. This can cause significant deviations from the ideal potential split, leading to reduced performance. These performance losses are encountered in the analysis of space weather variations on tugging performance, and shown in Figure 4.8. The dip in electron density after local noon results in a higher tug potential for a given beam current, which in turn results in a lower deputy potential.

It would be very beneficial if the tug could change the amount of current delivered to the

deputy without affecting its own potential. If a tug vehicle could maintain, for example, a 20 keV potential while emitting a broad range of electron beam currents, deputy charging could be improved and the tug vehicle would be able to perform charge transfer onto a wider variety of deputy sizes. With only electron beam emission, of course, this is impossible. However, consider a scenario where the tug is equipped not only with an electron gun, but also an ion beam. Assuming the ion beam is directed away from the deputy object in a manner that does not result in an additional current source on the deputy, the deputy charging dynamics would be the same as in Eq. (4.7). Assuming there is sufficiently more electron beam current than ion beam current so that the tug charges to a high positive potential, the tug current balance takes on the slightly modified form

$$I_t - I_b + I_e(\phi_T) = 0, \tag{4.21}$$

where I_b is the ion beam current. The tug potential, then, is a function of the net emitted current $\Delta I_B = I_t - I_b$:

$$\phi_T = \left(\frac{4\Delta I_B}{Aqn_e w_e} - 1 \right) T_e \tag{4.22}$$

The tug vehicle, being charged positive, will not recapture the beam ions in any significant capacity.

With the ion beam, a tug vehicle can theoretically emit any amount of electron beam current while maintaing a specific potential. For example, if the tug is desired to maintain a potential of 20 keV with a ΔI_B of 500 μA, any amount of electron beam current above 500 μA may be delivered to the deputy. If 1000 μA of electron beam current is emitted, then 500 μA of ion beam current must also be emitted to maintain the necessary ΔI_B.

The ion beam emission allows for performance improvement in a variety of ways. Revisiting the issue of tug/deputy size limitations, a tug would be able to achieve charge transfer onto objects larger than itself. With only an electron beam, the amount of beam current that the tug can emit is limited by the tug size. As the tug emits more current, it charges to a higher potential. The beam electrons that reach the deputy have a lower effective energy when they arrive, resulting in further performance losses due to higher secondary electron emission. With an ion beam included,

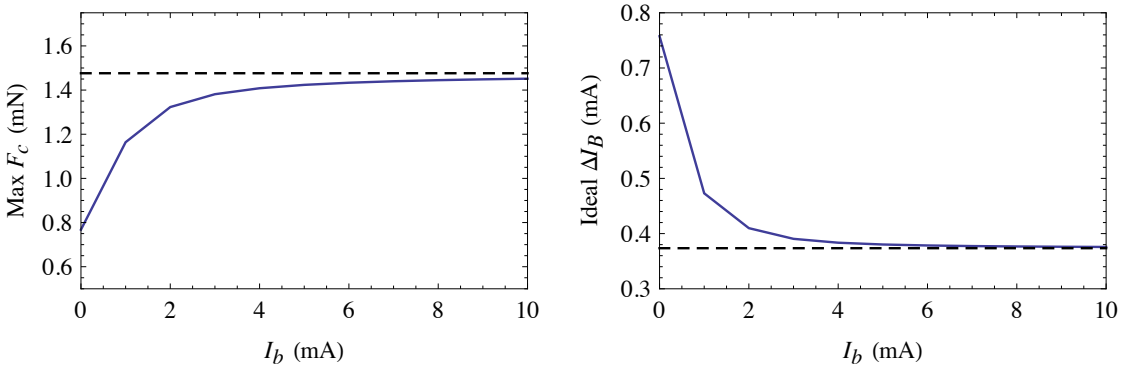

(a) Maximum E-Force

(b) Ideal ΔI_B

Figure 4.22: a) Maximum possible electrostatic force and b) ΔI_B required to obtain the maximum force for simultaneous electron and ion beam emission. Dashed lines are the limiting values for the case of very large current emission. The results are computed with $r_T = r_D = 2$ m and $E_{EB} = 40$ keV.

however, the tug can now deliver the necessary amount of electron beam current for deputy charging. Emitting higher levels of electron beam current does not necessarily result in higher tug potentials, because ion beam current can be increased to maintain a constant tug potential. More current can be delivered to the deputy at higher energies, inhibiting losses due to secondary electron emission. Considering the space weather driven performance losses illustrated in Figure 4.8, the increase in tug potential in the afternoon period can be eliminated by compensation with the ion beam. Keeping the tug potential from increasing also prevents the deputy potential from decreasing. The end result is that both potentials remain close to the ideal split, where best performance occurs.

Naturally, introducing another control variable once again raises the question of what current emission strategy will yield the best performance for the electrostatic tractor. To provide insight into the effects of increasing electron and ion beam currents on the resulting electrostatic force, a numerical optimization is once again used. Considering a range of emitted ion beam currents, the maximum possible electrostatic force and its associated electron beam current are computed. The nominal GEO space weather conditions at 17:30 are, again, used. Both tug and debris are assumed to have radii of two meters, and the electron beam energy is assumed to be 40 keV. The ion beam current is swept across a range of values, and the maximum possible electrostatic force is computed,

along with the ΔI_B need to achieve the max force. The results are shown in Figure 4.22. As the ion and, correspondingly, electron beam currents are increased, the maximum electrostatic force increases. However, there is a limit on the increase, regardless of how much current is emitted. This reflects the fact that for a given beam energy, the maximum potential difference between tug and deputy is finite. Furthermore, as the current is increased the ideal ΔI_B also converges towards a distinct value. Here, the inclusion of an ion beam allows for a significant boost in the electrostatic force magnitude. With only electron beam emission ($I_b = 0$), the maximum electrostatic force that can be generated is just under 0.8 mN. As the ion and, correspondingly, electron beam currents are increased, the maximum electrostatic force increases towards a limit of slightly less than 1.5 mN. This is an an increase of 87%, which would nearly cut the reorbiting time required in half.

These results imply that for the case of simultaneous electron and ion beam emission, delivering ever higher amounts of current to the deputy will yield the best tractor performance. Clearly, though, there is a limit to how large of an electrostatic force may be generated, even for very high current levels. The only non-beam deputy current source that increases directly as a function of the electron beam current is the secondary electron current. As the beam current is increased to very high values, the ion and photoelectron currents become insignificant relative to the secondary electron and beam absorption currents. Thus, the deputy will reach a potential that satisfies

$$I_D - 4Y_M I_D \kappa = 0. \tag{4.23}$$

The deputy potential that satisfies this current balance is

$$\phi_D = \phi_T - E_{EB} + E_{\max}(2Y_M - 1) + 2E_{\max}\sqrt{Y_M(Y_M - 1)}. \tag{4.24}$$

The maximum secondary electron yield Y_M must be greater than one for a real solution to exist. If the max yield were below 1, the secondary electrons would be unable to balance with the incoming beam current and the deputy would settle to a potential difference such that $q\phi_T - q\phi_D = E_{EB}$. With simultaneous electron and ion beam emission, the largest theoretical difference that is possible between tug and deputy is $E_{EB} - E_{\max}(2Y_M - 1) + 2E_{\max}\sqrt{Y_M(Y_M - 1)}$. The losses in efficiency due to secondary electron emission are apparent.

To compute the maximum possible force with electron/ion beam emission, the cost function

$$J = (r_D\phi_D - \rho\phi_T)(\rho\phi_D - r_T\phi_T) \tag{4.25}$$

is used. This comes directly from the electrostatic force expression, and the electrostatic force is at its largest magnitude when J is maximized. After substituting in Eq. (4.24) for ϕ_D, and setting $\partial J/\partial\phi_T = 0$, the tug potential that will yield that maximum force is found to be

$$\phi_T^* = \frac{E_{EB} - E_{\max}\left(2Y_M - 1 + 2\sqrt{Y_M(Y_M-1)}\right)}{2}\frac{\rho^2 - 2\rho r_D + r_D r_T}{(\rho - r_D)(\rho - r_T)}. \tag{4.26}$$

Similarly, the deputy potential at the maximum force condition is

$$\phi_D^* = -\frac{E_{EB} - E_{\max}\left(2Y_M - 1 + 2\sqrt{Y_M(Y_M-1)}\right)}{2}\frac{\rho^2 - 2\rho r_T + r_D r_T}{(\rho - r_D)(\rho - r_T)}. \tag{4.27}$$

It is worth noting the similarities between these ideal potentials and those in Eq. (4.8), computed for vacuum conditions. Both results are very similar, save for the losses in efficiency due to secondary electron emission. The ΔI_B required to provide the necessary ϕ_T^* is

$$\Delta I_B^* = A\mathcal{F}_e\left(1 + \frac{\phi_T^*}{T_e}\right). \tag{4.28}$$

This limit is plotted in Figure 4.22 for the scenario considered therein, and reflects the asymptote that the numerically computed result is approaching. The theoretical maximum force that can be generated with both ion and electron beam emission is

$$F_c = -\frac{r_D r_T}{4k_c(\rho - r_D)(\rho - r_T)}\left(E_{EB} + E_{\max}(1 - 2Y_M) - 2E_{\max}\sqrt{Y_M(Y_M-1)}\right)^2. \tag{4.29}$$

This limit is also plotted in Figure 4.22, and the numerically computed maximum forces approach it as the currents are increased.

Of course, emitting arbitrarily large currents is not physically possible for a number of reasons. In addition to very high power requirements, the maximum current is limited by the space charge effect. If the charge density in a beam is high enough, the mutual repulsion between similarly charged particles reduces the beam velocity and limits the current flow.[67] These results should

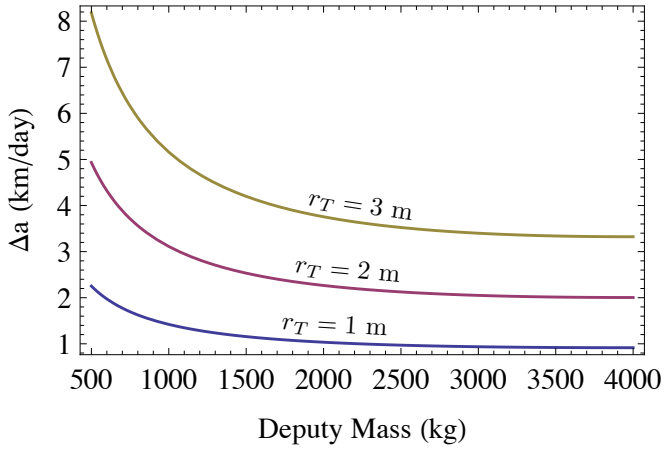

Figure 4.23: Theoretical maximum semi-major axis increase per day for a range of tug and deputy masses with simultaneous electron and ion beam emission. Results assume $E_{EB} = 40$ keV.

not be interpreted as implying that arbitrarily large currents can be emitted for the electrostatic tractor application. Rather, they serve to provide an upper limit on the performance improvement that may be gained by including ion beam emission in addition to electron beam emission. Further, Figure 4.22 shows that, for the vehicle sizes considered here, the achievable electrostatic forces with milliamp level currents approach the theoretical maximum to within 10%. Electron beam currents in excess of 10 milliamps have been demonstrated in flight, and the SCATHA mission is one such example.[64]

The semi-major axis increases per day for a one, two, and three meter radius tug as a function of deputy mass are computed using the ideal electrostatic force expression in Eq. (4.29), assuming an electron beam energy of 40 keV and quiet space weather conditions at 17:30. The results are shown in Figure 4.23. As expected, the three meter radius tug provides the best performance, towing objects of 4000 kg with a semi-major axis increase of more than 3 km/day. For the one meter tug, even simultaneous electron and ion beam emission is not enough to tow larger deputy objects at a rate of $\Delta a = 1$ km/day.

Considering the dual beam scenario, we address the question of the maximum towable deputy mass. To compute the maximum towable mass, the linear mass-radius relationship in Eq. (4.19) is once again employed. Using the best-case electrostatic force predicted by Eq. (4.29) in conjunction

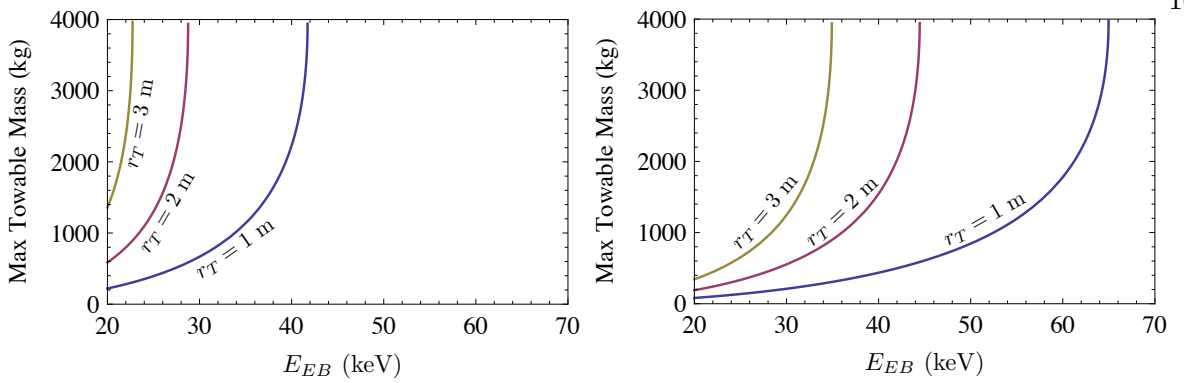

(a) Δa =1 km/day (b) Δa =2.5 km/day

Figure 4.24: Maximum towable mass using simultaneous electron and ion beam emission to meet performance criteria of a) $\Delta a = 1$ km/day and b) Δa =2.5 km/day.

with the approximate semi-major axis increase per day from Eq. (4.18) allows for a numerical solution of the deputy mass that will yield a desired Δa given a particular tug radius, separation distance, and electron beam energy. Two performance thresholds are used: Δa =1 km and Δa =2.5 km. The Δa =1 km performance level is somewhat lower than typically assumed, and for the debris reorbiting scenario would require a maneuver duration of roughly 10 months. The higher performance level of Δa =2.5 km is more typical of what has been assumed in prior electrostatic tractor research.[98]

The maximum towable masses as a function of electron beam energy are shown in Figure 4.24 for tug sizes of r_T =1, 2, and 3 meters. The improved performance for larger tug vehicles is apparent. Significantly less beam energy is needed to achieve the same level of performance for the three meter tug radius than for the one meter tug radius. By incorporating ion beam emission, a tug with a one meter radius can tow objects as large as 4000 kg at a rate of Δa =2.5 km/day with an electron beam energy of 65 keV. To achieve a Δa of 2.5 km/day, the three meter radius tug needs only 35 keV.

Ion beam emission, owing to the higher mass of ions relative to electrons, can impart a significant thrust force onto the tug vehicle. In fact, low-thrust propulsion systems have been designed around continuous ion emission.[10,39,114] Further, the ion-beam shepherd concept considers

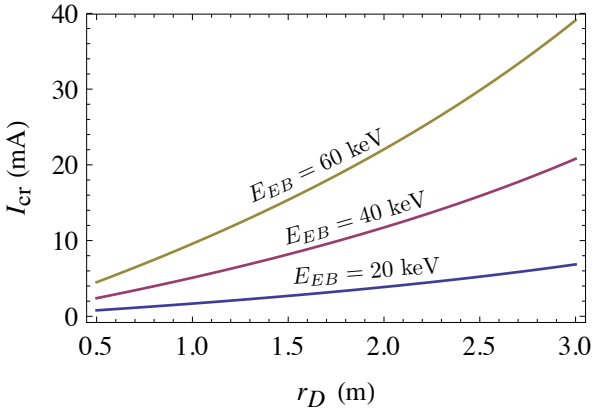

Figure 4.25: Ion beam current for which F_{th} is equal to the maximum possible electrostatic force for simultaneous electron and ion beam emission.

the use of a collimated ion beam to impart a small force onto a debris object due to the impact of the incoming ions on the debris object, which is used for deorbiting purposes.[12] For the case of simultaneous ion and electron beam emission, performance improves as more beam current is emitted. Because the ion thrust force increases as more current is emitted, there will be a point beyond which the thrust force is higher than the electrostatic force. Because the tug vehicle is charged to a high positive potential ions that are emitted will be repelled, so there is no need for a high energy ion beam. It is assumed that the ions are emitted in a direction that will not lead to their capture by the negatively charged deputy.

The thrust force on the tug due to the ion beam emission is

$$F_{th} = \frac{I_b}{q} m_b v_\infty(\phi_T) \tag{4.30}$$

where m_b is the mass of the ions and

$$v_\infty(\phi_T) = \sqrt{\frac{2q\phi_T}{m_b}} \tag{4.31}$$

is the velocity of the ions at infinity, after they have been accelerated out of the tug potential well. This formulation assumes that the ions are emitted with low energy, and that all of their v_∞ is due to acceleration by the tug's electric field. The ion species is assumed to be Argon (Ar^+), with an associated mass of $m_b = 6.63 \times 10^{-26}$ kg. The thrust force matches the performance limit for dual

beam emission when

$$\frac{I_b}{q} m_b v_\infty(\phi_T^*) = -\frac{r_D r_T}{4k_c(\rho - r_D)(\rho - r_T)} \left(E_{EB} + E_{\max}(1 - 2Y_M) - 2E_{\max}\sqrt{Y_M(Y_M - 1)} \right)^2. \quad (4.32)$$

Solving this equation for I_b yields the critical beam current, I_{cr}, for which more force is generated by the ion beam emission than is possible for the electrostatic attraction. Considering the case of a two meter tug radius, this critical current level is computed for electron beam energies of 20, 40, and 60 keV and presented in Figure 4.25. Higher beam energies allow for higher potentials on tug and deputy, resulting in a larger electrostatic force. Thus, it takes more ion beam current to generate equivalent levels of thrust. As r_D is increased, more charge accumulates on the deputy for the same potential level. This also results in a larger electrostatic force and a higher I_{cr} level. Depending on E_{EB} and the deputy size, only a few milliamps of current are required for the ion beam thrust to equal the maximum electrostatic force. As seen in Figure 4.22, it may take several milliamps of current before the electrostatic force magnitude begins to closely approach the theoretical maximum. This implies that actually achieving the potential increases that are possible with dual beam emission may result in a scenario where the ion beam thrust is on the same order of the electrostatic force. Considering again the scenario depicted in Figure 4.22, with a two meter tug and deputy radius, the electrostatic forces begin to closely approach the theoretical maximum around an ion beam current of 5-6 milliamps. Considering Figure 4.25, the amount of ion beam current required to reach the level of these electrostatic forces is 12 millamps. For this particular scenario, where roughly 5-6 milliamps of ion beam current are required to achieve maximum performance, the thrust due to the resulting ion beam emission is roughly half of the electrostatic force magnitude.

Operating the ion beam requires a consumable source of fuel for ion generation. The reorbiting times of several months means that the ion beam will have to be emitted continuously for a long duration. Thus, it is of interest to investigate roughly how much fuel is required for ion beam operation. The mass flow rate of fuel due to the ion beam is computed as

$$\dot{m}_F = \frac{I_b}{q} m_i. \quad (4.33)$$

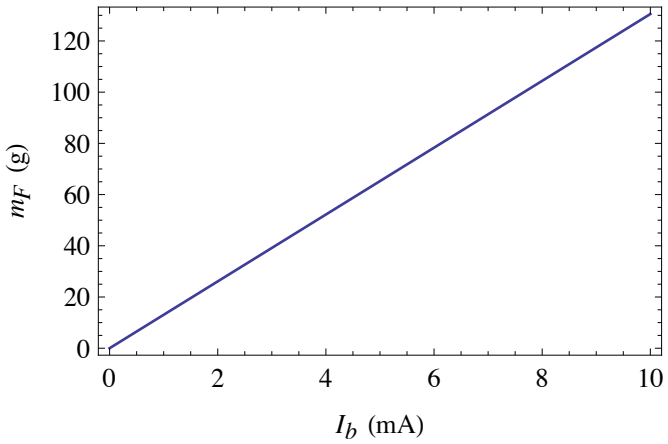

Figure 4.26: Fuel required for continuous ion beam emission over the course of one year.

Considering a continuous operating time of one year, the total fuel consumption for a range of ion beam currents is shown in Figure 4.26. For current levels of several milliamps, the total fuel consumption is about 130 g. Considering the sizes of the tug and deputy objects, this is a negligible increase in total system mass and not a significant hindrance for adding ion beam emission.

The decision to equip a tug vehicle with both an ion and electron beam depends on several factors. Really maximizing the benefits that are possible with simultaneous emission requires a large increase in the emitted beam current levels. This has a direct impact on the resulting power requirements. For a two meter tug with only an electron beam, the maximum power required for beam operation is in the supercharging scenario, and is about 30 W. Maximizing performance benefits with an ion beam requires at least several milliamps of current. Estimating power requirements as $P = I_t E_{EB}$, emitting 6 milliamps of electron beam current with an energy of 40 keV requires 240 W. This is an increase of 700%, and does not even include additional power consumption due to the ion beam emission. Still, power generation in excess of 10 kW has been achieved in operating GEO satellites,[42] so this issue of increased power consumption is not likely to pose any significant technical hurdles.

Another practical concern is the additional complexity of adding a second current source (the ion beam). While it can greatly improve the performance for smaller tug vehicles, this must

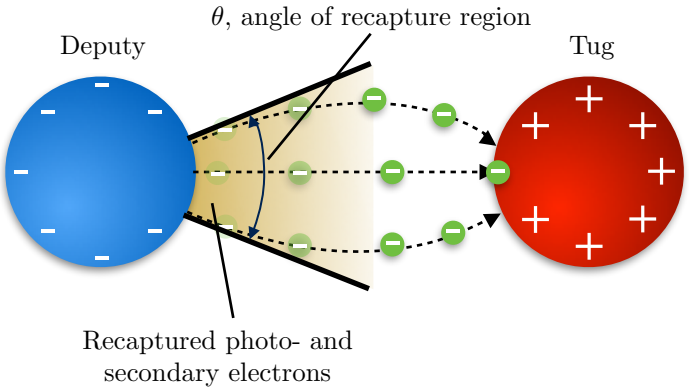

Figure 4.27: Electron back-flux from the deputy to the tug.

be weighed against the decision to simply build a larger tug vehicle with only an electron beam. Increasing the size of the tug does not necessarily necessitate increased vehicle mass and higher launch costs. There are no requirements on tug density, so it could be built like a hollow shell, keeping the mass increases manageable for larger tug vehicles.

Lastly, the ion beam emission introduces a significant thrust force. While this does not preclude any functionality of the electrostatic tractor it is something that the relative motion control system will have to compensate for, increasing the required thrust for station keeping. If the ions are emitted directly away from the deputy object, a ion-beam thrust on the same order as the electrostatic will double the station-keeping thrust requirements. This will, in turn, double fuel requirements. It may be possible, however, to mitigate these effects somewhat by emitting the ions such that they provide some portion of the required station-keeping thrust. Doing so, however, would require emission in the direction of the deputy object. This could lead to recollection of the ions by the deputy, which would reduce deputy charging and hurt tractor performance. A full analysis of this phenomenon is beyond the scope of this study.

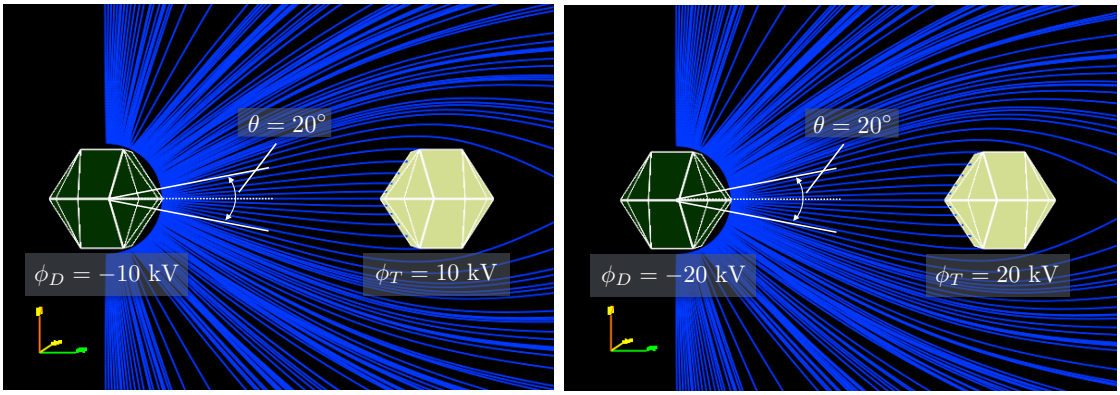

(a) $\phi_T = -\phi_D = 10$ kV (b) $\phi_T = -\phi_D = 20$ kV

Figure 4.28: Electron back-flux trajectories computed by NASCAP-2K for a) $\phi_T = -\phi_D = 10$ kV and b)$\phi_T = -\phi_D = 20$ kV. Results assume spheres of two-meter radius separated by a distance of 12 meters.

4.6 Tug Electron Back-Flux

Two deputy current sources are due to emission of electrons from the deputy surface: photo-electron and secondary electron emission. Because the deputy is charged negatively, these electrons are lost. The nearby tug, however, recaptures a portion of these emitted electrons, as depicted in Figure 4.27, owing to high positive potential. This serves as an additional current source on the deputy object which will impact its charging. Thus, it is important to study this effect, and obtain a rough estimate for how significantly these current sources affect tug charging. The scope of this analysis is not meant to be comprehensive, but rather to provide some insight into how much this back-flux might affect electrostatic tractor performance. A two meter radius is assumed for both tug and deputy and the quiet space weather conditions at 17:30 are maintained.

To identify the angle of the recapture region, θ, the NASCAP-2K spacecraft charging analysis software is used.[72] Developed by NASA and the Air Force Research Lab, NASCAP-2K is capable of simulating charging behavior of 3-D spacecraft models, computing potentials in space, and tracking particle trajectories. To identify the region of recapture, potentials are prescribed onto two spherical objects (each with two-meter radius) separated by a distance of 12 meters. NASCAP-2K is then used to compute the potentials in space around the objects. Following this computation, electrons

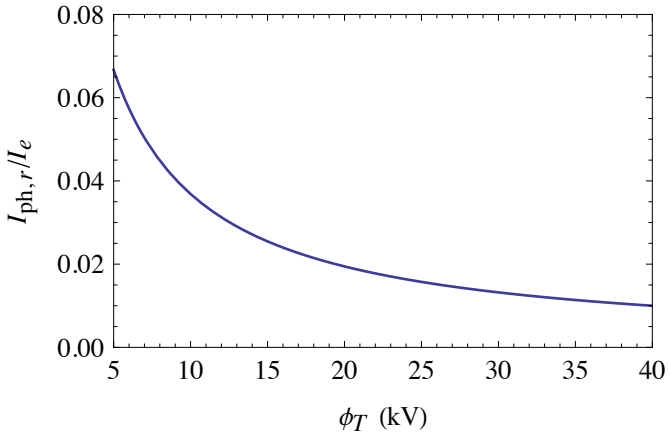

Figure 4.29: Ratio of recaptured photoelectron current and tug plasma electron current for two meter tug and deputy radii.

are distributed around the deputy object with a temperature of 2 eV. These electrons may represent either secondary or photoelectrons, as both are emitted at low energy. The electron trajectories are then computed to determine if they are recaptured by the tug vehicle. Two particular cases are considered: $\phi_T = -\phi_D = 20$ kV and $\phi_T = -\phi_D = 10$ kV.

The resulting electron trajectories are shown in Figure 4.28. The region of recapture for the 10 and 20 kV equal potential cases is nearly identical, with $\theta = 20°$. Any electrons emitted within this region will be recollected by the tug, constituting an additional current source that will affect tug charging. If the electron beam is directed along the line of sight from tug to deputy and is sufficiently narrow when it reaches the deputy, a very large portion of the resulting secondary electrons may be recaptured by the tug. Depending on the potential levels of tug and deputy, the secondary electron current can be a significant fraction of the beam current. In order to avoid the recapture of these electrons, a very narrow electron beam may not be the best choice. Alternately, the electron beam could be focused onto an area outside the region of recapture.

The back-flux of photoelectrons is an additional current source onto the tug. Assuming a worst-case scenario where the sun shines directly onto the region of recapture, the maximum cross

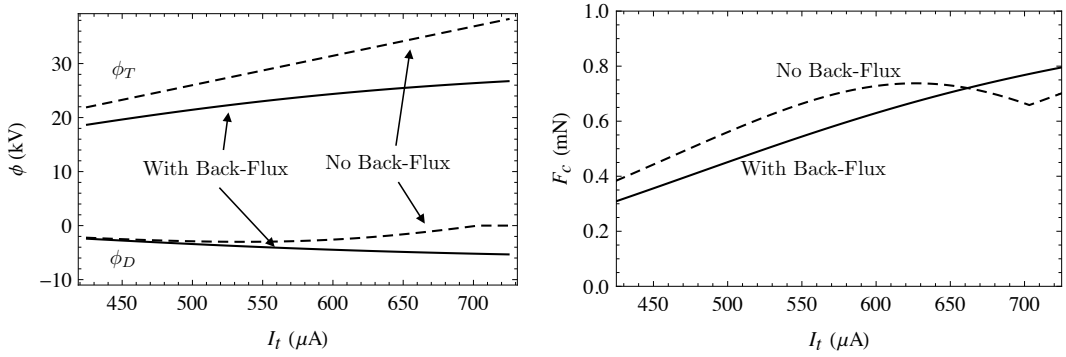

(a) Potentials (b) Electrostatic Force

Figure 4.30: a) Tug and deputy potentials with and without electron back-flux onto the tug and b) resulting electrostatic forces.

sectional area for which emitted photoelectrons are recaptured is

$$A_{\perp} = \pi r_D^2 \sin^2\left(\frac{\theta}{2}\right). \tag{4.34}$$

This is a higher area than could physically be exposed to sunlight because the tug would shadow at least some portion of the deputy. Assuming the tug is at potential levels of at least a few kiloVolts, the magnitude of this recaptured photoelectron current is insensitive to further increases in electron beam current. The recaptured photoelectron current is expressed as

$$I_{ph,r} = -\pi j_{ph} r_D^2 \sin^2\left(\frac{\theta}{2}\right). \tag{4.35}$$

To provide insight into how significant this current is on the tug, it is compared with the collected plasma electron current (I_e). Using the value of $\theta = 20°$ determined from the NASCAP-2K simulations, the ratio of recaptured photoelectron current to plasma electron current is shown in Figure 4.29. For the tug potentials considered for the electrostatic tractor application, the recaptured photoelectron current is a very small fraction (5% or less) of the incoming plasma electron current. Thus, this effect will not significantly impact the charging of the tug. The tug vehicle can simply emit slightly more current to offset these recaptured photoelectrons.

Assessing the impacts of recaptured secondary electrons is somewhat more complicated, because the recaptured SEE current depends on how well focused the beam is and how much beam

current is absorbed by the deputy. Assuming a worst case scenario where all secondary electrons are recaptured by the tug, the potentials ϕ_T and ϕ_D are found by solving

$$I_t + I_e(\phi_T) - I_{\text{SEE}}(\phi_T, \phi_D) + I_{ph,r} = 0 \tag{4.36a}$$

$$I_D(\phi_T, \phi_D) + I_e(\phi_D) + I_i(\phi_D) + I_{\text{SEE}}(\phi_T, \phi_D) + I_{ph} = 0. \tag{4.36b}$$

In the absence of back-flux, the tug potential is not a function of the deputy potential and can be solved directly. With back-flux, however, the tug potential is a function of the deputy potential due to the recaptured secondary electrons and these two current balance equations must be solved simultaneously for ϕ_T and ϕ_D. Considering the same 2 meter radius tug and deputy objects, at a separation distance of 12 meters, the potentials as a function of electron beam current are computed and shown in Figure 4.30. Also shown for comparison are the charging results if back-flux is neglected (or nonexistent). With back-flux, the tug and deputy potentials both increase as the electron beam is increased. Without back-flux, the tug potential increases linearly; the deputy potential increases up to a certain point and then begins to decrease. The presence of back-flux results in potential changes of several kiloVolts. The tug potential is lower than without back-flux, while the deputy potential is higher. The resulting electrostatic forces are also shown in Figure 4.30. For lower current values, the electrostatic force is reduced by the back-flux. However, there is a certain current level beyond which the electrostatic force is higher with back-flux than without it.

The potential for increased performance with electron back-flux is due to the same effect that improved performance with ion beam emission. The recaptured electrons reduce the tug potential for a given electron beam current. This allows for more current to be sent to the deputy at a higher energy level. The beam electrons lose less energy because the potential difference between tug and deputy is reduced by the back-flux. Because they arrive with more energy, the beam electrons induce fewer secondary electrons. This allows for the deputy to reach a higher potential, which can improve tractor performance at the cost of higher electron beam current. This phenomenon is driven primarily by the recaptured secondary electrons, because this current source is significantly larger than the small portion of photoelectrons that are recaptured. Of course, this analysis assumes

a worst case scenario where all secondary electrons emitted by the deputy are recaptured by the tug, which depends on how well-focused the beam is and where it is absorbed on the deputy. As a smaller portion of electrons are recaptured, the charging results approach those with no back-flux.

The brief analysis of electron back-flux on electrostatic tractor performance has identified several interesting phenomena. While there can be a substantial back-flux current onto the tug, it does not negatively impact performance. In fact, it can actually improve the magnitude of the electrostatic force between tug and deputy if more current is applied. Studying these effects further, extending the analysis to non spherical geometries, and characterizing these improvements in more detail would be good areas for further research. At this point, there is no evidence that the issue of back-flux from deputy to tug will inhibit the electrostatic tractor in any meaningful way.

Chapter 5

Conclusions

5.1 Summary of the Dissertation

Several fundamental questions regarding the electrostatic tractor GEO debris remediation strategy are addressed. Using a novel relative motion description, the equations of motion for the charged relative orbital motion are described. The relative motion coordinates are chosen because they allow for isolation of the separation distance between tug and deputy directly as a coordinate, and they allow for the avoidance of kinematic singularities that affected spherical coordinates used for a similar purpose in prior work. Using Lyapunov stability analysis, an asymptotically stabilizing control law is developed to stabilize the relative motion of tug and deputy during a reorbiting maneuver. The real challenge for implementing the controller is compensating for the electrostatic force resulting from tug and deputy charging. In practice, measuring the charging on tug and deputy is difficult, and an accurate measurement of the electrostatic force may be impossible. This is important because under-predicting the magnitude of the attractive electrostatic force can lead to a collision. Given some estimate of the severity of charge under-prediction that may occur, however, a bound on required control gains may be used to prevent such a collision. Even though the controller will not settle to the exact desired separation distance in the presence of uncertain charging, for the debris mitigation scenario this is not a major issue because the needed semi-major axis increases do not require precise relative positioning.

Using Gauss' variational equations, analytic predictions of reorbiting performance for different types of orbital corrections are considered. These more general orbital maneuvers apply to

scenarios beyond simple debris remediation. While some of these orbital corrections require a tug repositioning twice per orbit, these relocations only reduce tractor performance by a few percent. The electrostatic tractor is most suitable for planar orbit maneuvers like eccentricity and radius of perigee changes. Plane changes (inclination, RAAN) are simply too expensive in terms of required ΔV for the small tractor forces to succeed in any reasonable time frame.

An analysis of the typical space weather changes that occur over the course of a day in the GEO environment reveals that precise electron beam control is not required to achieve good reorbiting performance. While steps can be taken to modify the electron beam current to maximize the tractor forces, a much simpler approach of maintaining a fixed beam current yields nearly identical performance for much less effort. Geomagnetic storm activity does not inhibit charge transfer, and can actually provide improved tractor performance. The relative sizes of tug and deputy do present challenges to the charge transfer process. Indeed, it is very difficult for a tug to achieve charge transfer onto a deputy object roughly its own size. Charge transfer performance can be improved by incorporating an ion beam onto a tug vehicle equipped with an electron beam. Simultaneous electron and ion beam emission allows the tug to deliver more electron current to the deputy while keeping its own potential from increasing. This allows the deputy to reach a higher potential and the tractor force may be significantly improved, especially for smaller tug vehicles. Of course, this comes at the cost of higher power requirements and the added complexity of dual beam emission. Lastly, a portion of the emitted electrons from the deputy may be recaptured by the tug. This does affect the tug charging, and changes the optimal electron beam current for best performance. This back flux does not reduce the functionality of the electrostatic tractor, however, and allows for slightly higher electrostatic forces.

This study has provided additional evidence to confirm the feasibility of the electrostatic tractor for GEO debris remediation. Two approaches may be considered for the design of the tug vehicle, depending on the size requirements dictated by the launch vehicle. If a smaller tug vehicle (1 m radius) must be used, it would be best to equip it with both an ion and electron beam to allow for the towing of a wider range of deputy sizes. Alternately, if size constraints are not a serious

issue, good performance can be achieved with a 3 meter radius tug, and only an electron beam is required. The larger tug allows for the reorbiting of larger debris objects, so more potential threats could be removed.

5.2 Suggestions for Future Work

This work has identified several areas that would benefit from future research. The need to compensate for the uncertain electrostatic force is a challenging part of relative motion control. Future work might consider adaptive control strategies that are able to compensate for errors in estimated charging. Another good area for future work would be the consideration of the relative motion estimation. Using visual sensing methods, real time estimates of the relative motion could be obtained and integrated into the relative motion control algorithm. This estimation might also be done in such a way as to estimate the potentials (or charges) on the tug and deputy using the relative motion history.

The assumption that background plasma densities are what drive spacecraft potential would also be a good area for further research. There is no question that the presence of a highly charged object in the plasma environment leads to a rearrangement of the particles in space, and this effect occurs at lengths greater than the separation distances considered between tug and deputy. Future work might characterize how this affects the resulting plasma currents and, ultimately, the charging on the two objects. This would enable the charging model to be applied to the case where the electron beam is directed away from the deputy, and the tug charges highly positive.

The work so far has treated the deputy objects as perfect conductors. Real spacecraft contain dielectric and conductive materials, and these surfaces charge non-uniformly. Future research could consider how charge transfer would occur with such a structure, and how this would affect tractor performance. Numerical tools like NASCAP-2K might be useful for this purpose.

Bibliography

[1] Nasa safety standard: Guidelines and assessment procedures for limiting orbital debris. Technical Report NSS 1740.14, National Aeronautics and Space Administration, 1995.

[2] IADC space debris mitigation guidelines. Technical Report IADC-02-01, Inter-Agency Space Debris Coordination Committee, 2007.

[3] Shinsuke Abe, Tadashi Mukai, Naru Hirata, Olivier S. Barnouin-Jha, Andrew F. Cheng, Hirohide Demura, Robert W Gaskell, Tatsuaki Hashimoto, Kensuke Hiraoka, Takayuki Honda, et al. Mass and local topography measurements of itokawa by hayabusa. Science, 312(5778):1344–1347, 2006.

[4] F. Alby, E. Lansard, and T. Michal. Collision of cerise with space debris. In Second European Conference on Space Debris, volume 393, page 589, 1997.

[5] Paul V. Anderson and Hanspeter Schaub. Local orbital debris flux study in the geostationary ring. Advances in Space Research, 51(12):2195–2206, 2013.

[6] Paul V. Anderson and Hanspeter Schaub. Local debris congestion in the geosynchronous environment with population augmentation. Acta Astronautica, 94(2):619–628, Feb. 2014.

[7] Phillip C. Anderson. Characteristics of spacecraft charging in low earth orbit. Journal of Geophysical Research: Space Physics, 117(A7):n/a–n/a, 2012.

[8] S.J. Bame, D.J. McComas, M.F. Thomsen, B.L. Barraclough, R.C. Elphic, J.P. Glore, J.T. Gosling, J.C. Chavez, E.P. Evans, and F.J. Wymer. Magnetospheric plasma analyzer for spacecraft with constrained resources. Review of scientific instruments, 64(4):1026–1033, 1993.

[9] J. Bartels, N. H. Heck, and H. F. Johnston. The three-hour-range index measuring geomagnetic activity. Terrestrial Magnetism and Atmospheric Electricity, 44(4):411–454, 1939.

[10] John R. Beattie. Electrostatic ion thruster with improved thrust modulation, June 13 1989. US Patent 4,838,021.

[11] J.A. Bittencourt. Fundamentals of Plasma Physics. Springer-Verlag New York, Inc, 2004.

[12] Claudio Bombardelli and Jesus Pelaez. Ion beam shepherd for contactless space debris removal. AIAA Journal of Guidance, Control, and Dynamics, 34(3):916–920, May–June 2011.

[13] Claudio Bombardelli, Hodei Urrutxua, Mario Merino, Eduardo Ahedo, Jesus Pelaez, and Joris Olympio. Dynamics of ion-beam propelled space debris. In International Symposium on Space Flight Dynamics, Sao Jose dos Campos, Brasil, Feb. 28 – March 4, 2011 2011.

[14] Albert B. Bosse, W. James Barnds, Michael A. Brown, N. Glenn Creamer, Andy Feerst, C. Glen Henshaw, Alan S. Hope, Bernard E. Kelm, Patricia A. Klein, Frank Pipitone, Bertrand E. Plourde, and Brian P. Whalen. Sumo: spacecraft for the universal modification of orbits. In International Society for Optical Engineering, volume 5419, pages 36–46. SPIE, 2004.

[15] L. Breger and J. How. Gve-based dynamics and control for formation flying spacecraft. In 2nd International Symposium on Formation Flying Missions and Technologies, Washington, DC, September 14-16 2004.

[16] E.G.C. Burt. On space manoeuvres with continuous thrust. Planetary and Space Science, 15(1):103–122, January 1967.

[17] M.R. Carruth Jr, Todd Schneider, Matt McCollum, Miria Finckenor, Rob Suggs, Dale Ferguson, Ira Katz, Ron Mikatarian, John Alred, and Courtney Pankop. Iss and space environment interactions without operating plasma contactor. AIAA paper, 401(5), 2001.

[18] Marco M. Castronuovo. Active space debris removal- a preliminary mission analysis and design. Acta Astronautica, 69(9-10):848–859, 2011.

[19] CelesTrak. Iridium 33/cosmos 2251 collision. Technical report, http://celestrak.com/events/collision, May 2011.

[20] Mengu Cho, Raju Ramasamy, Toshiaki Matsumoto, Kazuhiro Toyoda, Yukishige Nozaki, and Masato Takahashi. Laboratory tests on 110-volt solar arrays in simulated geosynchronous orbit environment. Journal of spacecraft and rockets, 40(2):211–220, 2003.

[21] Mengu Cho, T. Sumida, H. Masui, K. Toyoda, Jeong-Ho Kim, S. Hatta, F.K. Wong, and Bao Hoang. Spacecraft charging analysis of large geo satellites using muscat. Plasma Science, IEEE Transactions on, 40(4):1248–1256, 2012.

[22] Ho-Sung Choi, Jaejin Lee, Kyung-Suk Cho, Young-Sil Kwak, Il-Hyun Cho, Young-Deuk Park, Yeon-Han Kim, Daniel N. Baker, Geoffrey D. Reeves, and Dong-Kyu Lee. Analysis of geo spacecraft anomalies: Space weather relationships. Space Weather, 9(6):n/a–n/a, 2011.

[23] John A. Christian and Scott Cryan. A survey of lidar technology and its use in spacecraft relative navigation. In 2013 AIAA Guidance, Navigation, and Control Conference. American Institute of Aeronautics and Astronautics, 2013.

[24] W. H. Clohessy and R. S. Wiltshire. Terminal guidance system for satellite rendezvous. Journal of the Aerospace Sciences, 27(9):653–658, 1960.

[25] Daniel Condurache and Vladimir Martinusi. Quaternionic exact solution to the relative orbital motion problem. Journal of Guidance, Control, and Dynamics, 33(4):1035–1047, July-August 2010.

[26] G.E. Cook. Luni-solar perturbations of the orbit of an earth satellite. Geophysical Journal of the Royal Astronomical Society, 6:271, 1962.

[27] P. Couzin, F. Teti, and R. Rembala. Active removal of large debris: Rendezvous and robotic capture issues. In 2nd European Workshop on Active Debris Removal, Paris, France, 2013. Paper No. 7.5.

[28] P. Couzin, F. Teti, and R. Rembala. Active removal of large debris: System approach of deorbiting concepts and technological issues. In 6th European Conference on Space Debris, Darmstadt, Germany, April 22–25 2013. Paper No. 6a.P-17.

[29] John H. Cover, Wolfgang Knauer, and Hans A. Maurer. Lightweight reflecting structures utilizing electrostatic inflation. US Patent 3,546,706, October 1966.

[30] Frederik J. de Bruijn, E. Gill, and J. How. Comparative analysis of cartesian and curvilinear clohessy-wiltshire equations. In 22nd International Symposium on Space Flight Dynamics, São José dos Campos, Brazil, February 28-March 04 2011.

[31] Sherman E. DeForest. Spacecraft charging at synchronous orbit. Journal of Geophysical Research, 77(4):651–659, 1972.

[32] M. H. Denton, M. F. Thomsen, H. Korth, S. Lynch, J. C. Zhang, and M. W. Liemohn. Bulk plasma properties at geosynchronous orbit. Journal of Geophysical Research, 110(A7), 2005.

[33] B. T. Draine and E. E. Salpeter. On the physics of dust grains in hot gas. Astrophysical Journal, 231(1):77–94, 1979.

[34] W. H. Farthing, J. P. Brown, and W.C. Bryant. Differential spacecraft charging on the geostationary operational environmental satellites. Technical Report NASA Technical Report TM-83908, National Aeronautics and Space Administration, 1982.

[35] R. L. Forward, R. P. Hoyt, and C. Uphoff. The terminator tether: a near-term commercial application of the nasa/msfc proseds experiment. In Proceedings of Tether Technology Interchange Meeting, September 9-10 1997.

[36] Robert B. Friend. Orbital express program summary and mission overview. In Proceedings of SPIE, Vol 6958. International Society for Optics and Photonics, 2008.

[37] F. F. Gabdullin, A.G. Korsun, and E. M. Tverdokhlebova. The plasma plume emitted onboard the international space station under the effect of the geomagnetic field. IEEE Transactions on Plasma Science, 36(5):2207, 2008.

[38] Henry Berry Garrett. The charging of spacecraft surfaces. Reviews of Geophysics, 19(4):577–616, 1981.

[39] Dan M. Goebel and Ira Katz. Fundamentals of electric propulsion: ion and Hall thrusters, volume 1. John Wiley & Sons, 2008.

[40] John Louis Goodman. History of space shuttle rendezvous and proximity operations. Journal of Spacecraft and Rockets, 43(5):944–959, 2006.

[41] Phillip Hill and Carl Peterson. Mechanics and Thermodynamics of Propulsion: 2nd Edition. Addison-Wesley Publishing Company, Inc., 1992.

[42] C.F. Hoeber, E. A. Robertson, I. Katz, V.A. Davis, and D.B. Snyder. Solar array augmented electrostatic discharge in geo. In 17th AIAA International Communications Satellite Systems Conference and Exhibit, Yokohama, Japan, Feb 23-27 1998. Paper AIAA 98–1401.

[43] Erik Hogan and Hanspeter Schaub. Space debris reorbiting using electrostatic actuation. In AAS Guidance and Control Conference, Breckenridge, CO, Feb. 3–8 2012. Paper AAS 12–016.

[44] Erik Hogan and Hanspeter Schaub. Relative motion control for two-spacecraft electrostatic orbit corrections. AIAA Journal of Guidance, Control, and Dynamics, 36(1):240–249, Jan. – Feb. 2013.

[45] Lee Holguin, Shashi Prabhakaran Viswanathan, and Amit Sanyal. Guidance and control for spacecraft autonomous rendezvous and proximity maneuvers using a geometric mechanics framework. In AIAA Guidance, Navigation, and Control Conference, 2012.

[46] Richard T. Howard, Andrew F. Heaton, Robin M. Pinson, and Connie K. Carrington. Orbital express advanced video guidance sensor. In 2008 IEEE Aerospace Conference. IEEE, 2008.

[47] I. I. Hussein and H. Schaub. Invariant shape solutions of the spinning three craft coulomb tether problem. Journal of Celestial Mechanics and Dynamical Astronomy, 96(2):137–157, 2006.

[48] L. Iess, C. Bruno, C. Ulivieri, U. Ponzi, M. Parisse, G. Laneve, G. Vannaroni, M. Dobrowolny, F. De Venuto, B. Bertotti, and L. Anselmo. Satellite de-orbiting by means of electrodynamic tethers part i: General concepts and requirements. Acta Astronautica, 50(7):399–406, 2002.

[49] L. Iess, C. Bruno, C. Ulivieri, and G. Vannaroni. Satellite de-orbiting by means of electrodynamic tethers part ii: System configuration and performance. Acta Astronautica, 50(7):407–416, 2002.

[50] Piotr Jasiobedzki, Stephen Se, Tong Pan, Manickam Umasuthan, and Michael Greenspan. Autonomous satellite rendezvous and docking using lidar and model based vision. In SPIE 5798, Spaceborne Sensors II, pages 54–65. International Society for Optics and Photonics, 2005.

[51] R. Jehn, V. Agapov, and C. Hernandez. The situation in the geostationary ring. Advances in Space Research, 35, 2005.

[52] Rudiger Jehn and Cristina Hernandez. International practices to protect the geostationary ring. Space Debris, 1:221–233, 2001.

[53] Fanghua Jiang, Junfeng Li, and Hexi Baoyin. Approximate analysis for relative motion of satellite formation flying in elliptical orbits. Celestial Mechanics and Dynamical Astronomy, 98:31–66, 2007.

[54] Nicholas L. Johnson. A new look at the {GEO} and near-geo regimes: Operations, disposals, and debris. Acta Astronautica, 80(0):82 – 88, 2012.

[55] Nicholas L. Johnson, Eugene Stansbery, David O. Whitlock, Kira J. Abercromby, and Debra Shoots. History of on-orbit satellite fragmentations- 14th edition. Technical Report NASA Technical Report TM-2008-214779, National Aeronautics and Space Administration, 2008.

[56] Yu S. Karavaev, R. M Kopyatkevich, M. N. Mishina, G. S. Mishin, P. G. Papushev, and P. N. Shaburov. The dynamic properties of rotation and optical characteristics of space debris at geostationary orbit. In Advances in the Astronautical Sciences, volume 119, pages 1457–1466, 2004. Paper No. AAS-04-192.

[57] I. Katz, B.M. Gardner, M.J. Mandell, G.A. Jongeward, M. Patterson, and R.M. Myers. Model of plasma contactor performance. Journal of spacecraft and rockets, 34(6):824–828, 1997.

[58] Ira Katz, V.A. Davis, and David B. Snyder. Mechanism for spacecraft charging initiated destruction of solar arrays in geo. In 36th AIAA Aerospace Sciences Meeting and Exhibit. AIAA, January 12-15 1998. DOI 10.2514/6.1998-1002.

[59] Michael C. Kelley. The Earth's Ionosphere: Plasma Physics & Electrodynamics, volume 96. Academic press, 2009.

[60] Lyon B. King, Gordon G. Parker, Satwik Deshmukh, and Jer-Hong Chong. Study of inter-spacecraft coulomb forces and implications for formation flying. AIAA Journal of Propulsion and Power, 19(3):497–505, 2003.

[61] Lyon B. King, Gordon G. Parker, Satwik Deshmukh, and Jer-Hong Chong. Spacecraft formation-flying using inter-vehicle coulomb forces. Technical report, NASA/NIAC, http://www.niac.usra.edu, January 2002.

[62] S. Kitamura. Large space debris reorbiter using ion beam irradiation. In 61st International Astronautical Congress, Prague, Czech Republic, Sept. 27 – Oct. 1 2010.

[63] Johan Köhler, Johan Bejhed, Henrik Kratz, Fredrik Bruhn, Ulf Lindberg, Klas Hjort, and Lars Stenmark. A hybrid cold gas microthruster system for spacecraft. Sensors and Actuators A: Physical, 97:587–598, 2002.

[64] Shu T. Lai. An overview of electron and ion beam effects in charging and discharging of spacecraft. IEEE Transactions on Nuclear Science, 36(6):2027–2032, 1989.

[65] Shu T. Lai. An improved langmuir probe formula for modeling satellite interactions with near-geostationary environment. Journal of Geophysical Research: Space Physics, 99(A1):459–467, 1994.

[66] Shu T. Lai. On supercharging: Electrostatic aspects. Journal of Geophysical Research: Space Physics (1978–2012), 107(A4):SMP–2, 2002.

[67] Shu T. Lai. Fundamentals of Spacecraft Charging. Princeton University Press, 2012.

[68] S.T. Lai. A critical overview on spacecraft charging mitigation methods. Plasma Science, IEEE Transactions on, 31(6):1118–1124, Dec 2003.

[69] Swiss Reinsurance Company Ltd. Space debris: On collision course for insurers? Technical report, http://media.swissre.com/documents/Publ11_Space+debris.pdf, March 2011.

[70] Edward T. Lu and Stanley G. Love. Gravitational tractor for towing asteroids. Nature, 438:177–178, November 2005.

[71] G.G. Managadze, V.M. Balebanov, A.A. Burchudladze, T.I. Gagua, N.A. Leonov, S.B. Lyakhov, A.A. Martinson, A.D. Mayorov, W.K. Riedler, M.F. Friedrich, et al. Potential observations of an electron-emitting rocket payload and other related plasma measurements. Planetary and space science, 36(4):399–410, 1988.

[72] Myron J. Mandell, Victoria A. Davis, David L. Cooke, Adrian T. Wheelock, and C.J. Roth. Nascap-2k spacecraft charging code overview. Plasma Science, IEEE Transactions on, 34(5):2084–2093, 2006.

[73] Myron J. Mandell, Ira Katz, Gary W. Schnuelle, Paul G. Steen, and James C. Roche. The decrease in effective photocurrents due to saddle points in electrostatic potentials near differentially charged spacecraft. IEEE Transactions on Nuclear Science, 25(6):1313–1317, 1978.

[74] S.M. Merkowitz, P.G. Maghami, A. Sharma, W.D. Willis, and C.M. Zakrzwski. A μnewton thrust-stand for lisa. Classical and Quantum Gravity, 19(7):1745, 2002.

[75] David K. Monroe. Space debris removal using a high-power ground-based laser. In Laser Power Beaming, volume 2121. SPIE, 1994.

[76] Tadashi Mukai, Shinsuke Abe, N. Hirata, R. Nakamura, O.S. Barnouin-Jha, A.F. Cheng, T. Mizuno, K. Hiraoka, T. Honda, H. Demura, et al. An overview of the lidar observations of asteroid 25143 itokawa. Advances in Space Research, 40(2):187–192, 2007.

[77] R. Mukherjee and D. Chen. Asymptotic stability theorem for autonomous systems. Journal of Guidance, Control, and Dynamics, 16:961–963, 1993.

[78] E. G. Mullen, M. S. Gussenhoven, and D. A. Hardy. Scatha survey of high-voltage spacecraft charging in sunlight. Journal of the Geophysical Sciences, 91:1074–1090, 1986.

[79] E.G. Mullen, A.R. Frederickson, G.P. Murphy, K.P. Ray, E.G. Holeman, D.E. Delorey, R. Robson, and M. Farar. An autonomous charge control system at geosynchronous altitude: flight results for spacecraft design consideration. Nuclear Science, IEEE Transactions on, 44(6):2188–2194, 1997.

[80] Naomi Murdoch, Dario Izzo, Claudio Bombardelli, Ian Carnelli, Alain Hilgers, and David Rodgers. Electrostatic tractor for near earth object deflection. In 59th International Astronautical Congress, Glasgow, Scotland, volume 29, 2008.

[81] Tomoko Nakagawa, Takuma Ishii, Koichiro Tsuruda, Hajime Hayakawa, and Toshifumi Mukai. Net current density of photoelectrons emitted from the surface of the geotail spacecraft. EARTH PLANETS AND SPACE, 52(4):283–292, 2000.

[82] Arun Natarajan and Hanspeter Schaub. Linear dynamics and stability analysis of a coulomb tether formation. Journal of Guidance, Control, and Dynamics, 29(4):831–839, July–Aug. 2006.

[83] Arun Natarajan and Hanspeter Schaub. Orbit-nadir aligned coulomb tether reconfiguration analysis. Journal of the Astronautical Sciences, 56(4):573–592, Oct. – Dec. 2008.

[84] Arun Natarajan and Hanspeter Schaub. Hybrid control of orbit normal and along-track two-craft coulomb tethers. Aerospace Science and Technology, 13(4–5):183–191, June–July 2009.

[85] Torsten Neubert and Peter M. Banks. Recent results from studies of electron beam phenomena in space plasmas. Planetary and Space Science, 40(2/3):153–183, 1992.

[86] Norman S. Nise. Control Systems Engineering. Wiley, 5th edition, 2008.

[87] National Oceanic and Atmospheric Administration. Noaa space weather scales. Technical report, http://www.swpc.noaa.gov/NOAAscales, March 2005.

[88] R.C. Olsen. Experiments in charge control at geosynchronous orbit-ats-5 and ats-6. Journal of Spacecraft and Rockets, 22(3):254–264, 1985.

[89] R.C. Olsen. Record charging events from applied technology satellite 6. Journal of Spacecraft and Rockets, 24(4):362–366, 1987.

[90] Antoine Petit, Eric Marchand, and Keyvan Kanani. Vision-based space autonomous rendezvous: A case study. In Intelligent Robots and Systems (IROS), 2011 IEEE/RSJ International Conference on, pages 619–624. IEEE, 2011.

[91] L. Pettazzi, D. Izzo, and S. Theil. Swarm navigation and reconfiguration using electrostatic forces. In 7th International Conference on Dynamics and Control of Systems and Structures in Space, The Old Royal Naval College, Greenwich, London, England, 16-20 July 2006.

[92] S. Pfau and M. Tichy. Low Temperature Plasma Physics: Fundamental Aspects and Applications. Wiley, Berlin, 2001.

[93] Carolyn K. Purvis, Henry B. Garrett, A.C. Whittlesey, and N. John Stevens. Design guidelines for assessing and controlling spacecraft charging effects, volume 2361. National Aeronautics and Space Administration, Scientific and Technical Information Branch, 1984.

[94] C.M. Saaj, Vaios Lappas, Hanspeter Schaub, and Dario Izzo. Hybrid propulsion system for formation flying using electrostatic forces. Aerospace Science and Technology, 14(5):348 – 355, 2010.

[95] Hanspeter Schaub and Lee E. Z. Jasper. Circular orbit radius control using electrostatic actuation for 2-craft configurations. In AAS/AIAA Astrodynamics Specialist Conference, Girdwood, Alaska, July 31 – August 4 2011. Paper AAS 11–498.

[96] Hanspeter Schaub and Lee E. Z. Jasper. Orbit boosting maneuvers for two-craft coulomb formations. AIAA Journal of Guidance, Control, and Dynamics, 36(1):74–82, Jan. – Feb. 2013.

[97] Hanspeter Schaub and John L. Junkins. Analytical Mechanics of Space Systems. AIAA Education Series, Reston, VA, 2nd edition, October 2009.

[98] Hanspeter Schaub and Daniel F. Moorer. Geosynchronous large debris reorbiter: Challenges and prospects. The Journal of the Astronautical Sciences, 59(1&2):165–180, 2012.

[99] Hanspeter Schaub, Gordon G. Parker, and Lyon B. King. Challenges and prospects of coulomb spacecraft formation control. Journal of the Astronautical Sciences, 52(1-2):169–193, 2004.

[100] Hanspeter Schaub and Zoltán Sternovský. Active space debris charging for contactless electrostatic disposal maneuvers. In 6th European Conference on Space Debris, Darmstadt, Germany, April 22–25 2013. ESOC. Paper No. 6b.O-5.

[101] Hanspeter Schaub and Daan Stevenson. Prospects of relative attitude control using coulomb actuation. In Jer-Nan Juang Astrodynamics Symposium, College Station, TX, June 25–26 2012. Paper AAS 12–607.

[102] Hanspeter Schaub, Srinivas R. Vadali, and Kyle T. Alfriend. Spacecraft formation flying control using mean orbit elements. Journal of the Astronautical Sciences, 48(1):69–87, 2000.

[103] Carl R. Seubert, Stephan Panosian, and Hanspeter Schaub. Dynamic feasibility study of a tethered coulomb structure. In AAS/AIAA Astrodynamics Specialist Conference, Toronto, Canada, Aug. 2–5 2010.

[104] Carl R. Seubert and Hanspeter Schaub. Tethered coulomb structures: Prospects and challenges. Journal of the Astronautical Sciences, 57(1-2):347–368, Jan.–June 2009.

[105] A. A. Sickafoose, J.E. Colwell, M. Horányi, and S Robertson. Experimental levitation of dust grains in a plasma sheath. Journal of Geophysical Research, 107(A11):SMP 37–1 – SMP 37–11, 2002.

[106] David E. Smith, Maria T. Zuber, Gregory A. Neumann, and Frank G. Lemoine. Topography of the moon from the clementine lidar. Journal of Geophysical Research: Planets (1991–2012), 102(E1):1591–1611, 1997.

[107] Eric S. Smith, Raymond J. Sedwick, John F. Merk, and Justin McClellan. Assessing the potential of a laser-ablation-propelled tug to remove large space debris. Journal of Spacecraft and Rockets, 50(6):1268–1276, 2013.

[108] Jack A. Soules. Precise calculation of the electrostatic force between charged spheres including induction effects. American Journal of Physics, 58(DOI: 10.1119/1.16251):1195, 1990.

[109] Daan Stevenson and Hanspeter Schaub. Multi-sphere method for modeling electrostatic forces and torques. Advances in Space Research, 51(1):10–20, Jan. 2013.

[110] Daan Stevenson and Hanspeter Schaub. Rotational testbed for coulomb induced spacecraft attitude control. In 5th International Conference on Spacecraft Formation Flying Missions and Technologies, Munich, Germany, May 29–31 2013.

[111] Laura A. Stiles, Carl R. Seubert, and Hanspeter Schaub. Effective coulomb force modeling in a space environment. In AAS Spaceflight Mechanics Meeting, Charleston, South Carolina, Jan. 29 – Feb. 2 2012. Paper AAS 12.

[112] D. A. Vallado. Fundamentals of Astrodynamics and Applications. Microcosm Press, Hawthorne, CA, 2007.

[113] Shuquan Wang and Hanspeter Schaub. Nonlinear charge control for a collinear fixed shape three-craft equilibrium. AIAA Journal of Guidance, Control, and Dynamics, 34(2):359–366, Mar.–Apr. 2011.

[114] Paul J. Wilbur, Vincent K. Rawlin, and J.R. Beattie. Ion thruster development trends and status in the united states. Journal of Propulsion and Power, 14(5):708–715, 1998.

[115] Song Zhang, Mingshan Hou, Dong Wang, and Tao Zhou. Optimal low-thrust trajectory design and robust tracking control for spacecraft rendezvous. In Control Conference (CCC), 2013 32nd Chinese, pages 4885–4888. IEEE, 2013.

Appendix A

Relative Motion Control with the Unit Vector Description

The most apparent obstacle present when using the unit-vector description for control is the fact that there are only three control inputs for a four dimensional system. However, the unit-vector components are not independent. Thus, it is possible to formulate the control problem in such a way as to obtain desired tracking behavior using the three control inputs.

A.1 Hill-Frame Like Control

For the first control law approach, consider the vector $\boldsymbol{R}$ defined as

$$\boldsymbol{R} = L\hat{\boldsymbol{e}}, \tag{A.1}$$

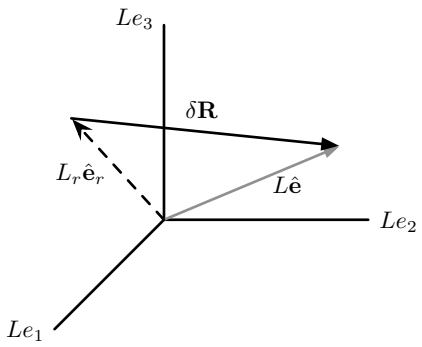

Figure A.1: The tracking error measure $\delta\boldsymbol{R}$ is the vector from the reference location to the current deputy position

with the associated derivatives

$$\dot{\boldsymbol{R}} = \dot{L}\hat{\boldsymbol{e}} + L\dot{\hat{\boldsymbol{e}}} \tag{A.2a}$$

$$\ddot{\boldsymbol{R}} = \ddot{L}\hat{\boldsymbol{e}} + 2\dot{L}\dot{\hat{\boldsymbol{e}}} + L\ddot{\hat{\boldsymbol{e}}} \tag{A.2b}$$

Note that the components of $\boldsymbol{R}$ are equivalent to the Cartesian Hill-frame components x, y, and z. Any set of L and $\hat{\boldsymbol{e}}$ will describe exactly one $\boldsymbol{R}$ vector. Thus, if the system tracks a desired L and $\hat{\boldsymbol{e}}$, then it will also track the equivalent $\boldsymbol{R}$. We may enforce tracking of L and $\hat{\boldsymbol{e}}$, then, by tracking the $\boldsymbol{R}_r$ vector, defined as

$$\boldsymbol{R}_r = L_r\hat{\boldsymbol{e}}_r, \tag{A.3}$$

where L_r and $\hat{\boldsymbol{e}}_r$ describe a desired reference trajectory. For the control law development, consider the candidate Lyapunov function[102]

$$V_1(\delta\boldsymbol{R}, \delta\dot{\boldsymbol{R}}) = \frac{1}{2}\delta\boldsymbol{R}^T[K]\delta\boldsymbol{R} + \frac{1}{2}\delta\dot{\boldsymbol{R}}^T\delta\dot{\boldsymbol{R}}, \tag{A.4}$$

where $\delta\boldsymbol{R} = \boldsymbol{R} - \boldsymbol{R}_r$ and $[K]$ is a positive definite gain matrix. Geometrically, the tracking error $\delta\boldsymbol{R}$ is the vector from the reference position to the actual position of the deputy, as illustrated in Figure A.1. It makes sense, then, that driving this vector to $\mathbf{0}$ would lead to tracking of the reference trajectory. The derivative of the candidate Lyapunov function with respect to time is

$$\dot{V}_1(\delta\boldsymbol{R}, \delta\dot{\boldsymbol{R}}) = \delta\dot{\boldsymbol{R}}^T\left([K]\delta\boldsymbol{R} + \ddot{\boldsymbol{R}} - \ddot{\boldsymbol{R}}_r\right). \tag{A.5}$$

For the deputy motion, the acceleration of $\boldsymbol{R}$ is

$$\ddot{\boldsymbol{R}} = [f_R] + \boldsymbol{u} = \begin{bmatrix} 2n(\dot{L}e_2 + L\dot{e}_2) + 3n^2Le_1 \\ -2n(\dot{L}e_1 + L\dot{e}_1) \\ -n^2Le_3 \end{bmatrix} + \begin{bmatrix} u_x \\ u_y \\ u_z \end{bmatrix}. \tag{A.6}$$

Substituting this back into the Lyapunov rate function yields

$$\dot{V}_1(\delta\boldsymbol{R}, \delta\dot{\boldsymbol{R}}) = \delta\dot{\boldsymbol{R}}^T\left([K]\delta\boldsymbol{R} + [f_R] + \boldsymbol{u} - \ddot{\boldsymbol{R}}_r\right). \tag{A.7}$$

To ensure Lyapunov stability, the control law is chosen as

$$\boldsymbol{u} = -[K]\delta\boldsymbol{R} - [P]\delta\dot{\boldsymbol{R}} + \ddot{\boldsymbol{R}}_r - [f_R], \tag{A.8}$$

where [P] is a positive definite gain matrix. This control law results in the negative semi-definite Lyapunov rate

$$\dot{V}_1(\delta \boldsymbol{R}, \delta \dot{\boldsymbol{R}}) = -\delta \dot{\boldsymbol{R}}^T [P] \delta \dot{\boldsymbol{R}} \tag{A.9}$$

and closed loop tracking dynamics

$$\delta \ddot{\boldsymbol{R}} + [P]\delta \dot{\boldsymbol{R}} + [K]\delta \boldsymbol{R} = \boldsymbol{0}. \tag{A.10}$$

To examine asymptotic stability, higher-order derivatives are taken and evaluated on the set $\delta \dot{\boldsymbol{R}} = \boldsymbol{0}$.[77] The first non-zero derivative is found to be

$$\dddot{V}_1(\delta \boldsymbol{R}, \delta \dot{\boldsymbol{R}} = \boldsymbol{0}) = -2\delta \boldsymbol{R}^T [K]^T [P][K] \delta \boldsymbol{R} \tag{A.11}$$

which is negative definite in terms of $\delta \boldsymbol{R}$. Thus, the control law tracks the reference trajectory asymptotically. Furthermore, the asymptotic stability is global, due to the radially unbounded nature of the candidate Lyapunov function in Eq. (A.4).

The control law in Eq. (A.8) does not linearize the dynamics of L and $\hat{\boldsymbol{e}}$. Rather, it provides linear closed-loop tracking error dynamics. Using the unit-vector description, the preceding control law development provides a means to track an arbitrary, potentially time-varying reference trajectory. Its major drawback, however, is that it does not isolate the actuation of the separation distance from the relative orientation. For collision avoidance applications, it would be useful to be able to stabilize the relative separation distance more rapidly than relative orientation. This would allow for reorientation maneuvers which occur at a safely maintained separation distance. Indeed, one may argue that little is gained using this control law versus a similar development using Cartesian Hill frame coordinates. After all, this control law is essentially actuating on these Hill-frame coordinates directly, albeit with a different description. While perhaps not ideal, these developments illustrate that it is possible to track an arbitrary reference trajectory using the unit-vector description.

A.2 Isolating L and $\hat{e}$: γ Control Law

For the next control development, the problem of isolating the separation distance actuation capabilities from the relative orientation is considered. That is, a control law is sought which would allow for tracking of some reference L_r more quickly than a reference orientation $\hat{\boldsymbol{e}}_r$. Such a control would stabilize the relative separation distance early on in the maneuver before a large reorientation has occurred, thus minimizing the chance of collision. Rather than attempting to control all states of the system, only the separation distance and two elements of the unit-vector are considered. As an example, consider an orientation error measure defined by e_1 and e_2. If the control is tracking a reference e_{1r} and e_{2r}, then

$$e_1^2 + e_2^2 + e_3^2 = 1 = e_{1r}^2 + e_{2r}^2 + e_{3r}^2. \tag{A.12}$$

Because $e_1 = e_{1r}$ and $e_2 = e_{2r}$ once the system has converged to the reference, it is guaranteed that

$$e_3 \to \pm e_{3r}. \tag{A.13}$$

Thus, the system may converge to a state that is at the proper separation distance, but not at the proper orientation. A similar argument may be repeated for any of the other pairs of unit-vector components. Determination of the conditions required for convergence to the proper value is left for future work.

To arrive at a control law which isolates the separation distance from the relative orientation, consider the error measure $\delta\boldsymbol{\gamma}$, defined as

$$\delta\boldsymbol{\gamma} = \boldsymbol{\gamma} - \boldsymbol{\gamma}_r = \begin{bmatrix} L \\ e_i \\ e_j \end{bmatrix} - \begin{bmatrix} L_r \\ e_{ir} \\ e_{jr} \end{bmatrix}, \tag{A.14}$$

where e_i and e_j denote any two components of $\hat{\boldsymbol{e}}$. This error measure is used to define the candidate Lyapunov function

$$V_2(\delta\boldsymbol{\gamma}, \delta\dot{\boldsymbol{\gamma}}) = \frac{1}{2}\delta\boldsymbol{\gamma}^T[K]\boldsymbol{\gamma} + \frac{1}{2}\delta\dot{\boldsymbol{\gamma}}^T\delta\dot{\boldsymbol{\gamma}}, \tag{A.15}$$

where $[K]$ is a positive definite gain matrix. The derivative of this Lyapunov function is

$$\dot{V}_2(\delta\boldsymbol{\gamma}, \delta\dot{\boldsymbol{\gamma}}) = \delta\dot{\boldsymbol{\gamma}}^T \left([K]\delta\boldsymbol{\gamma} + \ddot{\boldsymbol{\gamma}} - \ddot{\boldsymbol{\gamma}}_r\right). \tag{A.16}$$

The differential equation for $\boldsymbol{\gamma}$ is

$$\ddot{\boldsymbol{\gamma}} = [f_\gamma] + [G_\gamma]\boldsymbol{u}, \tag{A.17}$$

where the elements of $[f_\gamma]$ and $[G_\gamma]$ are populated from Eq. 2.23 depending on which components of $\hat{\boldsymbol{e}}$ are used. Substituting these dynamics back into the Lyapunov rate expression yields

$$\dot{V}_2(\delta\boldsymbol{\gamma}, \delta\dot{\boldsymbol{\gamma}}) = \delta\dot{\boldsymbol{\gamma}}^T \left([K]\delta\boldsymbol{\gamma} + [f_\gamma] + [G_\gamma]\boldsymbol{u} - \ddot{\boldsymbol{\gamma}}\right). \tag{A.18}$$

To ensure stability, the control requirement used for the system is

$$[G_\gamma]\boldsymbol{u} = -[f_\gamma] - [K]\delta\boldsymbol{\gamma} - [P]\delta\dot{\boldsymbol{\gamma}} + \ddot{\boldsymbol{\gamma}}_r, \tag{A.19}$$

where $[P]$ is a positive definite gain matrix. This results in the negative semidefinite Lyapunov rate

$$\dot{V}_2(\delta\boldsymbol{\gamma}, \delta\dot{\boldsymbol{\gamma}}) = -\delta\dot{\boldsymbol{\gamma}}^T[P]\delta\dot{\boldsymbol{\gamma}}. \tag{A.20}$$

As before, asymptotic stability is determined through consideration of higher order derivatives of V_2.[77] Evaluated on the set $\delta\dot{\boldsymbol{\gamma}} = \mathbf{0}$, the first non-zero derivative is

$$\ddot{V}_2(\delta\boldsymbol{\gamma}, \delta\boldsymbol{\gamma} \doteq \mathbf{0}) = -2\delta\boldsymbol{\gamma}^T[K]^T[P][K]\delta\boldsymbol{\gamma}, \tag{A.21}$$

which is negative definite in terms of $\delta\boldsymbol{\gamma}$. Thus, if Eq. (A.19) is satisfied the system is asymptotically stable. The region of stability is global, due to the radially unbounded nature of V_2.

In order to find the control acceleration, $[G_\gamma]$ must be inverted and multiplied by the right hand side of Eq. (A.19). This presents a problem, however, as $[G_\gamma]$ is not always invertible. The nature of this singularity becomes evident when considering the determinant of $[G_\gamma]$. It is solely a function of L and e_k,

$$|[G_\gamma]| = \frac{e_k}{L^2}, \tag{A.22}$$

where e_k is the component of $\hat{\boldsymbol{e}}$ **not** used in $\boldsymbol{\gamma}$. If relative motion is desired in the chief orbit plane, for example, e_1 and e_2 cannot be used in $\boldsymbol{\gamma}$ or $[G_\gamma]$ will be singular all along the reference trajectory, where $e_3 = 0$.

The singularity issue is a very significant drawback to using this second control law to track a reference trajectory. If e_1 and e_2 are used in $\boldsymbol{\gamma}$, any trajectory that crosses from one side of the chief orbital plane to the other will encounter a singularity at the moment of crossing. If e_2 and e_3 are used in $\boldsymbol{\gamma}$, a trajectory that moves from above to below the chief (or vice-versa) will pass through the singularity. Lastly, if e_1 and e_3 are used in $\boldsymbol{\gamma}$, any trajectory that passes from in front to behind the chief (or vice-versa) will encounter the singularity issues. These conditions are extremely limiting on the number of reference trajectories that may be followed, and the performance of the system is very dependent on the starting location of the deputy. If the deputy is able to reach and converge onto the reference trajectory before a singularity is encountered then no problems will occur. However, for arbitrary reference motion and initial deputy conditions this is unlikely to be the case.

Let us turn our attention to a specific example of converging onto a naturally occurring relative motion. It is well known that for close separation distances, a naturally occurring relative motion is a 2x1 ellipse in the chief orbit plane. We will assume, at least for this example, that the ellipse is centered on the chief. It would not be possible to use e_1 and e_2 in $\boldsymbol{\gamma}$ for this case due to the fact that $e_3 = 0$ all along the reference trajectory. Thus, it would be required to use e_3 and either e_1 or e_2 in $\boldsymbol{\gamma}$. However, both e_1 and e_2 will pass through 0 twice during each revolution of the ellipse. This example illustrates how significant the singularity issues are, even in enforcing simple, naturally occurring motion.

The second major issue is the indeterminacy of e_k. There is no guarantee that the relative orientation will converge to the reference. It is likely that if the deputy starts closer to e_{kr} than $-e_{kr}$ that it will converge to the proper orientation, but there is no guarantee. Furthermore, note that to converge from a position near e_{kr} onto $-e_{kr}$, the system would have to pass through the singularity. For example, assume that e_3 is not used in $\boldsymbol{\gamma}$. If e_{3r} is a positive value, and $e_3(t_0)$ is

also positive, the only way the system could converge to $-e_{3r}$ is if e_3 passed through the singularity at 0.

A.3 Numerical Simulation of the γ Control Law

The γ control law is implemented into an inertial simulation, where the trajectory of each craft is determined from integration of

$$\ddot{\boldsymbol{r}}_i = -\frac{\mu}{r^3}\boldsymbol{r}_i + \boldsymbol{u}, \tag{A.23}$$

where $\boldsymbol{u}$ is determined from the control laws developed above. The relative motion is then computed using the inertial trajectories of each craft. The initial conditions for each simulation are determined by defining a set of orbital elements for the chief, and orbit element differences for the deputy. Because the unit-vector equations of motion are obtained from the linearized CW equations, the orbital element differences will be kept at small levels such that the linear approximation is valid. The initial conditions of tug and deputy are shown in Table 2.1. For this validation, no charging is modeled and there is no electrostatic force.

To demonstrate the performance of the unit-vector γ control law, a time-varying reference trajectory is prescribed in the Hill frame and the control law is applied to track the reference. The target reference motion, which is not a naturally occurring motion, is

$$x_r(t) = 0.05\cos(nt) \text{ (km)} \tag{A.24a}$$

$$y_r(t) = 0.05\sin(nt) \text{ (km)} \tag{A.24b}$$

$$z_r(t) = 0.02\sin(2nt + \pi/2) + 0.03 \text{ (km)}. \tag{A.24c}$$

The z coordinate is maintained positive to avoid singularity issues that would occur for the case when e_3 would pass from negative (-z) to positive ($+z$). The reference trajectory is transformed into unit-vector components for implementation into the control law, with gains of $[K] = n^2\text{diag}([10; 1; 1])$ and $[P] = n * \text{diag}([10; 1; 1])$. Gain selection is important for this scenario. Improper gain selection will cause the system to encounter the singular transition from $+z$ to $-z$.

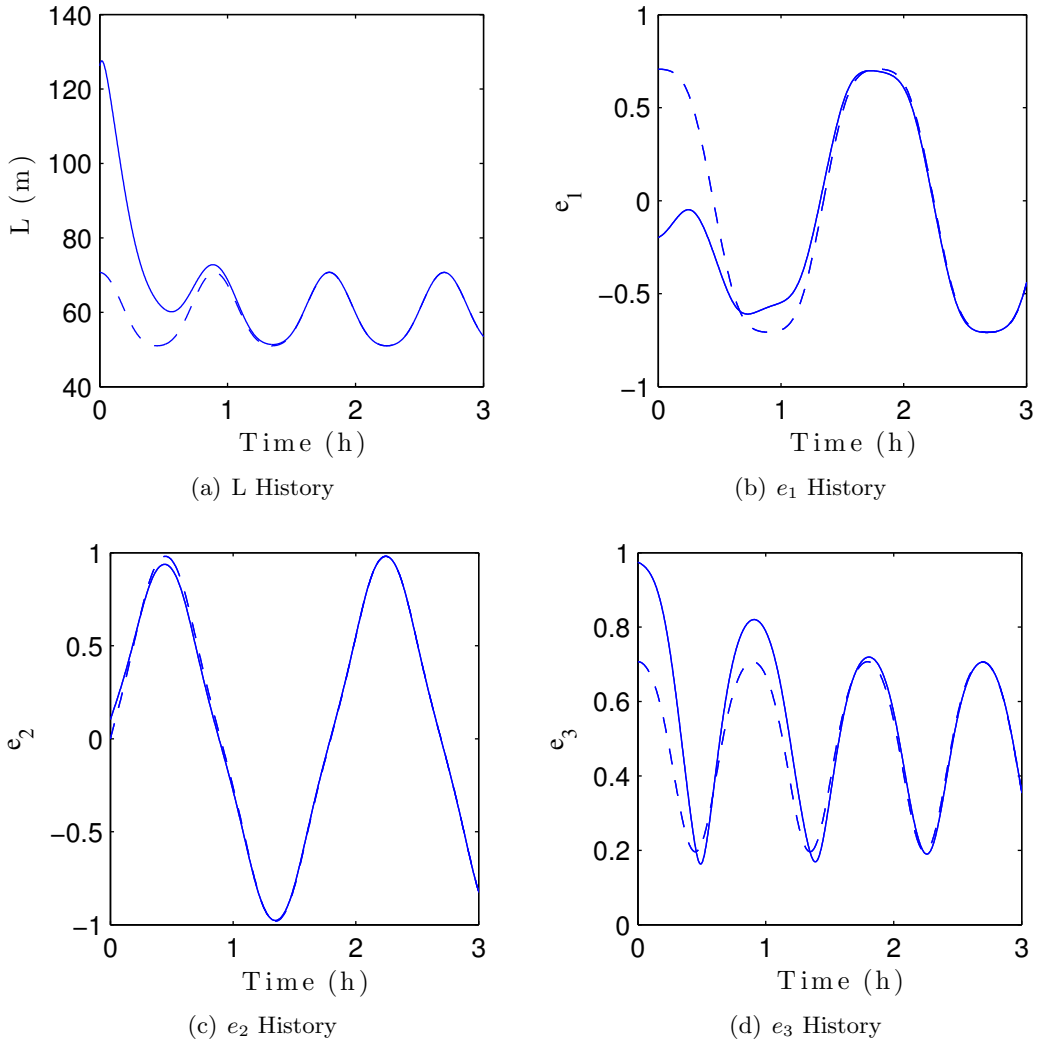

(a) L History (b) e_1 History

(c) e_2 History (d) e_3 History

Figure A.2: Time histories of L and $\hat{\boldsymbol{e}}$ during tracking maneuver. The reference trajectory is shown as a dashed line.

Here, appropriate gains are chosen to avoid encountering the singularity and illustrate proper functionality of the control law.

The $\boldsymbol{\gamma}$ control law is applied using L, e_1, and e_2 for the error measure. By weighting the separation distance error 10 times higher than the relative orientation error, the singularity is avoided. The time histories of L and $\hat{\boldsymbol{e}}$ during the maneuver are shown in Figure A.2, and the state errors are presented in Figure A.3. Due to the higher gains on the L error, the rate of converge to the reference separation distance is faster than the rate of convergence to the reference orientation.

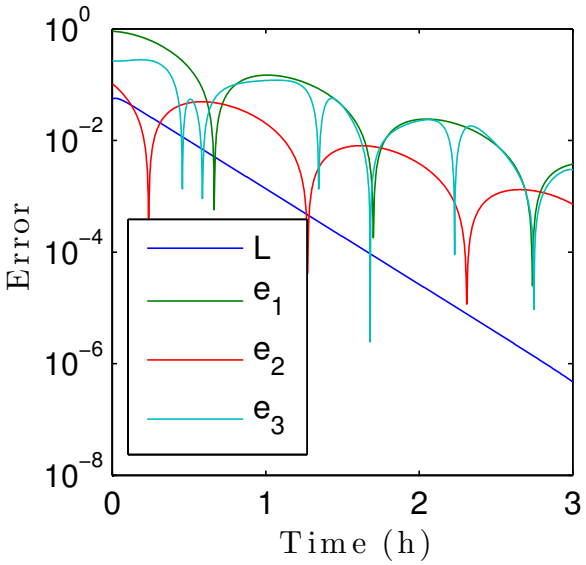

Figure A.3: State errors for γ control law throughout tracking maneuver.

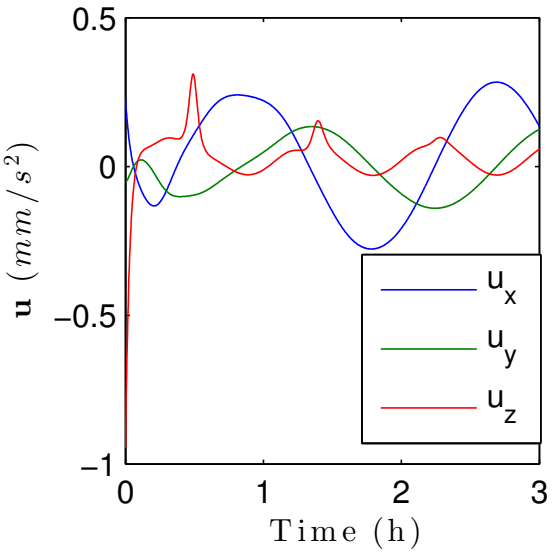

Figure A.4: Control inputs for γ set control law.

The control inputs generated by the γ control law are shown in Figure A.4. The transient response necessary for the deputy to reach the reference trajectory is evident, followed by the non-zero control required to maintain the non-naturally occurring reference motion. The magnitude of control acceleration needed is on the order of mm/s^2.